Focused Ion Beam Micromachining of *Si* and *GaAs* Using *Ga* and *Au* Liquid Metal Ion Sources

Geoffrey A. Crow
B.A., University of Chicago, 1983

A dissertation submitted to the faculty
of the Oregon Graduate Institute
of Science and Technology
in partial fulfillment of the
requirements for the degree
Doctor of Philosophy
in
Applied Physics

October, 1990

The dissertation *Focused Ion Beam Micromachining of* Si *and* GaAs *Using* Ga *and* Au *Liquid Metal Ion Sources* by Geoffrey A. Crow has been examined and approved by the following Examination Committee:

Jon Orloff, Thesis Advisor
Professor

Paul Davis
Professor

Anthony Bell
Associate Professor

Mark Utlaut
Assistant Professor, University of Portland

To no one in particular.

Figures

Figures

Figures

Tables

Abstract

Focused Ion Beam Micromachining of Si *and* GaAs
Using Ga *and* Au *Liquid Metal Ion Sources*

Geoffrey A. Crow, Ph.D.
Oregon Graduate Institute, 1990

Supervising Professor: Jon Orloff

Application of focused ion beam(FIB) technology is increasing rapidly. A particularly important application is focused ion beam micromachining(FIBM). This technique is used in areas such as mask repair, IC modification, and opto–electronic device fabrication, where knowledge of the sputtering yield is critically important. Because of the importance of sputtering yields, the following series of experiments was undertaken.

The sputtering yield of single crystal (100) oriented *Si* and *GaAs* were measured as functions of ion energy and angle of incidence for Ga^+ ion bombardment. These materials were chosen because of their importance in FIBM, particularly integrated circuit repair and opto-electronic device fabrication. In addition, the effects of ion dose, beam scan velocity and

ion channeling were investigated. For comparison, the sputtering yield for $Au^{+,++}$ bombardment of *GaAs* was also measured, and single crystal (111) oriented *Si* was bombarded by Ga^{+} to test the effects of crystal orientation.

The results of the above experiments were analyzed in terms of Sigmund's linear cascade theory of sputtering. A brief overview of the theory is presented to show how the angular and energy dependence of the sputtering yield enter into the theory. The dependence of the sputtering yield on incident angle and ion energy is then compared to theoretical predictions.

The above yield measurements were made by machining a rectangular crater of a consistent size and shape, chosen to minimize the effects of redeposition and facilitate the measurement of the sputter crater volume. Real applications of FIBM involve the machining of more complicated structures, where the net sputtering yield can be significantly different. To check the applicability to FIBM of the above measurements, they were compared to measurements made for more complex structures typical of FIBM.

In the course of machining these structures, an equation was derived which relates the shape of the surface to be machined, to the scan velocity of the beam and the sputtering yield of the target. The time dependence of the beam position required to create the desired surface was obtained by solving a nonlinear partial differential equation. Several different surface contours were machined using this technique. The sputtering yield was measured for one particularly simple example, and was then compared to the yield measurements described above. Two other examples illustrate the application of the equation to the production of more complicated surfaces.

Introduction

The past fifteen years have seen the field of finely focused ion beams (FIB) grow from it's infancy to become an important technology with a wide variety of applications. The first finely focused beams were produced using a gas field ionization (GFI) source, and were used primarily for scanning ion microscopy (SIM)[1,2]. A side effect of the ion bombardment was the sputtering of the target material, which suggested that finely focused beams could be used to fabricate submicron structures or perform surface microanalysis at submicron spatial resolution. Unfortunately, the early GFI sources were of limited brightness, so the total probe current in these early systems was too small for such applications to be practical.

The development of the liquid metal ion source (LMIS) provided a dramatic increase in ion source brightness[3-7]. Submicron ion beams could be produced with current densities of several amps/cm^2, and applications such as focused ion beam micro-machining (FIBM) and SIMS finally became practical.

I. Applications of FIB.

The following is a brief summary of some of the applications of focused ion beam technology. The factor common to most of them is the need to know, as accurately as possible, the sputtering yield for a given ion-target combination.

A. Scanning Ion Microscopy.

As with the GFI source, the first application of LMIS FIB technology was microscopy, where the brighter sources led to improved imaging from the much improved signal to noise ratio[8,9]. Ion microscopy is of interest because it is much more surface sensitive than conventional scanning electron microscopy. The penetration depth of the ions is much smaller than for electrons, and the secondary particles detected in forming the image originate much closer to the sample surface. SIM

images are very sensitive to the surface topography of a sample, and because of the possibility of ion channeling, can provide information about the crystalline structure of a sample.

Scanning ion microscopy is a destructive technique, because the ion beam is sputtering the sample while it is being imaged. Knowledge of the sputtering yield is not vital to SIM, but it may be useful to know the rate at which the sample is being consumed.

B. Focused Ion Beam Micro-Machining.

Another early application of focused ion beams using liquid metal ion sources was in FIBM, where it was demonstrated that the ion beam could be used to fabricate lines in *Si* substrates with a width of 0.1 μm[10]. This led to a series of practical applications, all of which require knowledge of the sputtering yield for some ion-target combination.

One of the first practical uses envisioned was the repair of photo-masks used for the manufacture of integrated circuits[11-14]. Opaque defects in the mask are machined away using FIBM, and clear defects corrected by machining light scattering structures in the clear glass substrates. More recently focused ion beam induced deposition has been used to deposit thin opaque films of carbon or other materials in the area of clear defects[15,16]. These are now well characterized applications of focused ion beams, and systems for repairing

photo-masks are commercially available. X-ray mask repair is also possible using similar techniques. Opaque defects are eliminated by FIBM, and clear defects corrected by FIB induced deposition of *Au*.

Modification and failure analysis of integrated circuits using FIBM has developed into another important application[14,17-21]. Conducting traces can be cut to modify circuit operation or repair defects in the circuit. The FIB can be used to machine holes in the passivation of integrated circuits, while retaining their functionality, to allow the probing of the underlying circuitry for trouble–shooting and failure analysis. Perhaps the most important, but least recognized application of FIBM in failure analysis of integrated circuits, is micro-cross sectioning of circuit defects to reveal the three dimensional structure of the circuit and to isolate the source of the defect. As the average feature size of a typical IC continues to decrease, standard metallographic techniques for creating precision cross sections no longer work. The only viable alternative is FIB technology.

Fabrication of opto–electronic devices is another area in which FIBM has become an important tool[22-29]. Structures can be machined into the surface of a semiconductor diode laser, modifying it's optical properties, and producing a laser that could not have been fabricated in any other way, or where alternate fabrication techniques are much more time consuming and less reliable. Coupled cavity and surface emitting

devices have been produced by FIBM, and maskless ion implantation using an FIB has been used to produce gratings for distributed Bragg reflector lasers.

C. Chemically Assisted Focused Ion Beam Micromachining.

Because of the wide variety of potential applications for FIBM, efforts have been made to improve throughput by increasing the sputtering yields of various substrate materials. The most promising technique is chemically enhanced FIBM, where a chlorine or fluorine containing gas is bled into the sample chamber[26,30-38]. The gas adsorbs onto the substrate surface where it reacts chemically, aided by the energy from the ion beam, and the resulting volatile reaction by–products are pumped away. Using this technique, increases in etch rates by a factor of ten, compared to physical sputtering, have been reported for some ion-target combinations.

D. Focused Ion Beam Induced Deposition.

In addition to the circuit modification techniques which use the ion beam to remove existing electrical interconnections, the beam can also be used to fabricate new ones. Connections between layers of a device can be made by redeposition of sputtered material, and conducting lines can be deposited by operation of the LMIS in droplet mode to form a

focused droplet beam[39,20]. More recently thin metal films have been deposited by FIB induced decomposition of metal bearing gases[12,40-51]. Gas bled into the sample chamber is adsorbed onto the surface of the target, and the energy from the ion beam dissociates the adsorbed molecules. Volatile dissociation byproducts are pumped away, and the nonvolatile byproducts form a film on the target surface. Dissociation takes place only where the beam strikes the target, so the metal film can be patterned by appropriately scanning the beam. The properties of the film are determined by the deposition conditions such as the substrate temperature, the gas flux at the surface of the sample, the ion flux, and the choice of gas. The net deposition rate depends on the gross deposition rate and the sputtering rate of the deposited film, since some sputtering is still occurring even during the deposition process. Various metal bearing gases have been used to deposit conducting films of many different materials, including gold, tungsten, iron and aluminum. The resistivities of these films are typically much higher than for the bulk material, but are still low enough for practical applications.

E. Ion Implantation.

Ion implantation using focused ion beams is another active area of interest[27,52-55]. The major advantage of this technique, over conventional broad beam ion implantation, is the ability to tailor the implant profile to

optimize device performance. The small size of the beam also allows the creation of structures which would be difficult or impossible to create using standard techniques. However, the serial nature of the exposure process limits throughput.

F. Microanalysis using Focused Ion Beams.

Finally, LMIS FIB technology is used in sub–micron spatial resolution SIMS. A wide variety of applications have been explored[56-62]. In addition SIMS technology has also been applied to the problem of end point detection when doing FIBM of layered structures[63,64]. Monitoring the appropriate signal provides the ability to halt the machining process at the interface between different layers. This is of particular importance in modification of integrated circuits where there is a danger of destroying the device if the ion beam is allowed to penetrate too deeply.

II. Objectives.

One common factor in most of the above applications is the need to know the removal rate of the material being sputtered. In mask repair it is critical to stop the machining process at the appropriate point, since machining for too short a time will not completely remove the defect, while machining for too long will stain the glass substrate with implanted ions, creating another defect where the original one was

removed. In IC modification, to maintain device functionality, only the desired layers can be machined. Any underlying layers which are inadvertently sputtered may leave the device inoperative. In opto–electronic device fabrication, the size and shape of machined structures are critical to the device's optical properties. A precise knowledge of the sputtering yield is essential in determining these properties. Depth profiling with SIMS also requires an accurate measure of the sputtering yield.

Because of the importance of sputtering yields in the application of FIB technology, the following series of experiments was undertaken.

A. Measurement of Sputtering Yields.

The sputtering yields of single crystal (100) oriented *Si* and *GaAs* were measured as functions of ion energy and angle of incidence for Ga^+ ion bombardment. These materials were chosen because of their importance in FIB applications, particularly integrated circuit repair and opto-electronic device fabrication. In addition, the effects of ion dose, beam scan velocity and ion channeling were investigated. For comparison, the sputtering yield for $Au^{+,\,++}$ bombardment of *GaAs* was also measured, and single crystal (111) oriented *Si* was bombarded by Ga^+ to test the effects of crystal orientation.

B. Comparison to Theory.

The results of the above experiments are analyzed in terms of Sigmund's linear cascade theory of sputtering[65]. A brief overview of the theory is presented to show how the angular and energy dependence of the sputtering yield enter into the theory. The dependence of the sputtering yield on incident angle and ion energy is then compared to theoretical predictions.

C. Vector Scanning.

The above yield measurements were made by machining a rectangular crater of a consistent size and shape, chosen to minimize the effects of redeposition and facilitate the measurement of the sputter crater volume. A real application of FIBM involves the machining of more complicated structures, where the net sputtering yield could be significantly different. To check the applicability to FIBM of the above measurements, they were compared to measurements made for more complex structures typical of FIBM.

In the course of machining these more complex structures, an equation was derived which relates the surface contour to be machined, to the scan velocity of the beam and the sputtering yield of the target. The time dependence of the beam position required to create the desired

surface contour was obtained by solving a nonlinear partial differential equation. Several different contours were machined using this technique. The sputtering yield was measured for one particularly simple example, and was then compared to the yield measurements made for simple rectangular sputter craters. Two other examples illustrate the application of the equation to the production of more complicated surfaces.

1. Experimental Apparatus

This chapter will describe the apparatus used in gathering the experimental data presented below. The data was collected over a period of about 2 years, using two separate but related FIB systems. During this time, the apparatus was constantly evolving, changes were made to incorporate design improvements, and accommodate the research being carried out by other students. While changes to the system generally resulted in improved performance, they also sometimes precluded the possibility of repeating an experiment. This was particularly true of the vector scanning experiments conducted on the first generation system, which could not be continued on the second generation system because of the lack of vector scanning capabilities.

I. The First Generation FIB System.

A. The Ion Gun

The ion gun used on both FIB systems was manufactured by FEI of Hillsboro, Oregon[66]. A schematic diagram of the gun is shown in Fig. 1 - 1. The major components of the gun are: the source assembly consisting of the LMIS, the suppressor and the extractor electrode; the electrostatic lens which contains the beam defining aperture; the beam blanker which includes the blanking plates and beam blanking aperture; and the octupole stigmator/deflector.

In normal operation, the LMIS is biased at the beam accelerating voltage, which is variable between 5 and 25 kV in 5 kV increments. The extractor electrode and the first electrode of the electrostatic lens are biased at the same potential, about -10 kV relative to the source, which results in total emission current from the source of several microamperes. The potential on the suppressor electrode allows for fine adjustment of the emission current without varying the extractor voltage and hence changing the focusing properties of the lens. The beam is focused onto the target by varying the potential applied to the center electrode of the lens. The magnitude of this voltage depends on the

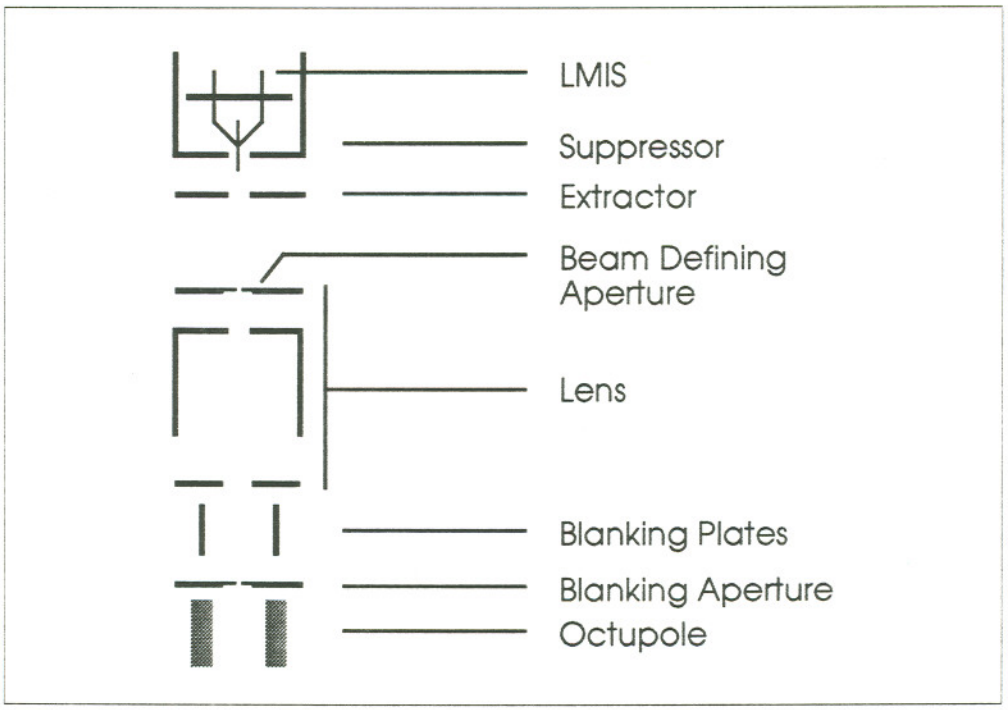

Fig. 1 - 1. Schematic diagram of the FEI single lens ion gun. The major components of the gun are: the source assembly consisting of the LMIS, the suppressor and the extractor electrode; the electrostatic lens which contains the beam defining aperture; the beam blanker which includes the blanking plates and beam blanking aperture; and the octupole stigmator/deflector.

accelerating voltage and working distance. The final lens electrode is kept at ground potential.

The lens was specifically designed to minimize chromatic aberration, which is what limits the spot size in most LMIS FIB systems[67]. Fig. 1 - 2 shows a plot of the spot size and current density of the ion gun for a variety of different beam defining apertures and accelerating voltages. Typical operating conditions for the ion gun were 15 keV accelerating voltage, 2 mrad beam defining aperture, beam current of

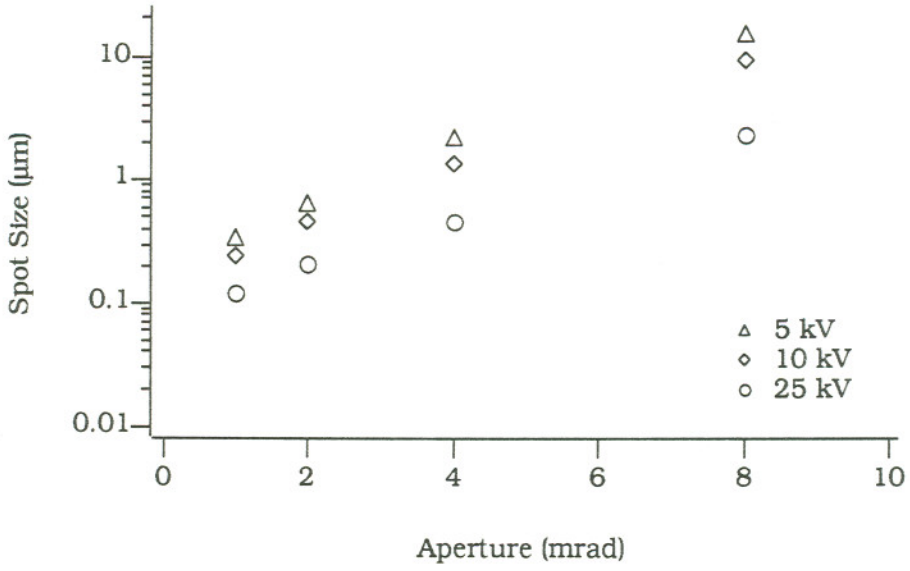

Fig. 1 - 2. Calculated beam diameter as a function of aperture half angle at a 25 mm working distance for the FEI single lens ion column with a *Ga* LMIS. Values were taken from a plot supplied by the manufacturer.

about 0.25 nA, spot size of about 0.3 µm, and current density of about 0.5 A/cm^2.

The focused beam is scanned across the target surface by the octupole deflector, which also provides astigmatism correction and beam offset. Blanking plates are positioned just above the octupole. By applying a voltage across the plates, the path of the beam is shifted so it no longer passes through the blanking aperture. With the beam blanked, the beam current may be measured by measuring the current striking the blanking aperture. To get an accurate reading the aperture is biased at +300 V during the measurement to suppress secondary electron

emission. The accuracy of this technique will be discussed in more detail in the next chapter.

B. Ion Sources.

The ion sources used in the FEI optical column are of the solid needle type first described by Clampitt et al.[5]. Typically, a tungsten wire is electrochemically etched to a point, with a radius of curvature of several microns. The needle is wetted by the liquid metal, and placed in a strong electric field. The electrostatic and hydrodynamic forces on the liquid form it into the characteristic Taylor cone. At the apex of the cone a jet of the order of 1 to 10 nm in radius forms, and at the end of this jet ions are emitted by field evaporation[68-74].

A wide variety of elemental and alloy sources have been made, but only a limited number of them are suitable for the current work. The choice is limited by the desire to compare the experimentally measured sputtering yields to the predictions of the linear cascade theory, which requires that all ions have the same mass and energy. Because the FEI ion gun lacks an $\mathbf{E} \times \mathbf{B}$ filter, only an elemental source that emits ions of a single charge and mass species can be used.

Elemental sources which were available for use included *Al, Au, Bi, Cs, Ga, In,* and *U.* Of these, the *Au, Ga,* and *In* sources are the easiest to work with. All three of these metals wet the tungsten substrate material

without attacking it, and each has a sufficiently low vapor pressure at its melting point to yield a source with a reasonably long lifetime. In the case of *Ga* and *In*, the ion beams produced are composed of nearly 100% singly charged ions[69,72]. Of these the *Ga* source is easier to operate, as it doesn't require heating, and it is in fact the most widely used LMIS for FIB. For these reasons it was chosen as the primary ion source for the first generation FIB system.

C. Vacuum System

The ion gun was mounted on a standard SEM vacuum chamber in place of the original electron optical column. The chamber included a sample stage with 5 degrees of freedom, X, Y, Z, Tilt, and Rotation. As originally constructed, the sample and gun vacuum chambers were pumped by a single large ion pump.The sample chamber pressure was monitored with an ionization gauge, and was typically in the 10^{-7} torr range. The gun chamber pressure was comparable. Sample exchange was performed by venting both chambers. This arrangement was very inefficient, with typical turn around times being about 24 hours. In addition, the characteristics of the LMIS could be altered by each up to air event, so source operation could be quite erratic.

To overcome these difficulties, the vacuum system was modified to provide differential pumping of the two chambers, and an isolation valve

was designed and built so the sample chamber could be vented independently of the gun chamber. This reduced turn around time to about 8 hours, and provided for much more stable source operation by avoiding source contamination. The operating pressure for the ion gun was reduced from the 10^{-7} torr range into the 10^{-8} torr range which also contributed to greater source stability. The typical sample chamber pressure remained in the 10^{-7} torr range.

D. Scan Electronics.

Two different systems were available for controlling the scanning of the beam, one digital and one analog. Digital scan generation was done using a Heathkit model H-207 computer running Z-DOS version 1.0, which was equipped with appropriate digital to analog and analog to digital converters. The digitally generated ramps allowed precise control of the beam for FIBM. A software package written by Micrion Corp.[75] was used for beam control, and provided a variety of control options. Most important was the ability to define a series of scan rectangles, lines, and spots and associated pixel overlaps and dwell times. By combining these elements, complex surface contours could be machined[23,24]. Any series of rectangles, lines and spots and their associated overlaps and dwell times could be stored on disk, and later recalled to reproduce the same structure.

A major drawback of the Micrion software package was the technique used to blank the beam. In a typical micromachining application a feature is machined by repeatedly scanning the beam at a relatively large scan velocity over the area where the material is to be removed. Each repetition removes a small fraction of the total amount of material to be removed. As was shown by Yamaguchi[76,77], the resulting sputter crater is closer to the ideal shape than if the same feature is machined with a single slow scan, even though the ion dose is the same. Unfortunately, the Micrion software package automatically blanked the beam between each repetition of the scan, so for a feature which required several hundred or thousand repetitions to create, a significant amount of machining would occur along the path the beam took when traveling between its blanked and unblanked positions. This was corrected in the second generation system, where the beam was blanked only after the completion of all machining.

In addition to the software package provided by Micrion, several simple programs were written to control the beam using non-linear ramps. The shape of the ramps was determined by using an algorithm developed to relate a desired surface contour to the ramp voltages necessary to produce it[28,29,78]. This will be discussed in more detail in a separate chapter.

Because of the limited speed of the digital scan control, analog ramp generators were used for real time imaging. Column alignment, astigmatism correction, and sample positioning were all done using the analog scan generators. The scan rate could be varied over a wide range, but was typically several frames per second. Slow scans were also possible for recording images photographically.

E. Video Electronics.

A channel electron multiplier (CEM) was used to collect either secondary electrons or secondary ions. When collecting secondary electrons, the anode of the CEM was typically biased at 2 - 3 keV, so an optical isolation system was used to decouple the detector output from the high voltage. For ease of operation, this system was also used for secondary ion detection where the CEM anode was at ground potential. When collecting secondary electrons, the CEM cathode could be biased at several hundred volts to improve collection efficiency.

An operational amplifier converted the current out of the detector into a voltage which was supplied to an optical encoder. The encoder transmitted the signal through a fiber optic link to a decoder which supplied the signal to the video amplifier. The signal out of the video amplifier was used to form an image on a CRT in the same way a

standard SEM image is formed. The gain and offset of the video amplifier controlled the image contrast and brightness.

In addition to the analog video display, the computer provided the ability to capture an image in computer memory, display the image on the computer monitor, and adjust its contrast and brightness. Unfortunately, image resolution was limited to 128 by 128 pixels and 8 shades of gray, so the image quality was rather poor. However, the system did prove useful in cases were it was necessary to limit the ion exposure of the target. It was possible to grab an image of the target and locate the area to be machined from the stored image, avoiding the ion exposure associated with real time imaging. The system also showed the potential applications of image processing to FIBM, and improved image processing capabilities were incorporated into the second generation system.

II. The Second Generation FIB System.

After gaining valuable experience with the FIB system described above, a second generation system was constructed which combined a scanning electron microscope and an FIB column. The advantages of a combined SEM/FIB system are obvious. The resolution of the SEM will allow the examination of machined features at a much higher resolution than is possible with the FIB, providing more detailed information than

the ion beam can about the size and shape of a sputter crater. Additionally, imaging with the ion beam is inherently destructive, so examining a sputter crater results in changes in the crater shape. An SEM eliminates the problem of sample sputtering. Also, with both beams incident at the same point on the target, it was hoped that the machining process could be observed in real time, providing information about the evolution of micro-machined features.

The following description of the second generation system focuses on the operation of the ion gun. Operation of the SEM was substantially unchanged by the addition of the FIB column. The only modifications to the standard operation of the SEM were the improved image processing capabilities provided by a minicomputer which was interfaced to the system. This will be discussed in more detail below.

A. The Ion Gun.

The optical design of the second generation ion column was identical to the first, but the second ion gun incorporated improved construction techniques which allowed for easier maintenance and safer operation. Unfortunately, the second generation column was not as stable as the first, as there were problems with beam drift relative to the target which were not present in the first system. Repeated attempts were made to find the source of the drift, which appeared to be caused by charging of

some component of the ion gun, but the source was never found. Beam drift as opposed to sample stage drift appeared to be the problem, as no comparable drift of the electron beam relative to the sample was observed.

The main effect of the drift was the smearing of sputter crater edges, making measurements of crater volumes less precise. It also limited the ability of the system to study sputter crater evolution. During a typical 30 minute exposure, the beam could drift by as much as 20 microns. This was about the size of the feature being machined, so when such drift occurred the sample was effectively ruined. After several hours of operation, typical drift was about 1 to 2 microns in 30 minutes, which could be tolerated when making sputter craters for measuring sputtering yields, but was still unacceptable for applications which required greater precision, such as micro-machining opto–electronic devices, or studying sputter crater evolution over time scales of more than a few minutes.

B. Ion Sources.

As with the first generation system, a *Ga* LMIS was used most frequently in the second generation system, but, to determine the effects of the ion species on the sputtering process, a *Au* source was also tried. The *Au* source was chosen because of the large mass difference between *Au* and *Ga*, and because it is easier to fabricate and operate than any of

the other elemental sources, with the exception of *In* which is very similar to *Ga*. One disadvantage of the *Au* source is the composition of the resulting ion beam, which contains significant quantities of both Au^{+} and Au^{++} in a ratio of about 1.5:1 at a total tip current of 10μA[72]. The ratio increases with decreasing emission current, but is still only about 3:1 at a total emission current of 4 μA[79]. The different charge species must be accounted for when calculating the sputtering yield, and when comparing the measured yield to the linear cascade theory.

A second disadvantage of the *Au* LMIS, compared to *Ga*, is the much shorter source lifetime, some tens of hours for a typical *Au* source compared to several hundred hours for a typical *Ga* source. The reason for the difference is the relatively high vapor pressure of *Au* at it's melting point, which means that most of the *Au* is lost by evaporation, and very little of it is emitted as ions. Given the relatively short lifetime of the source, and the amount of time required to change sources, it was not possible to collect as much data with the *Au* beam as with the *Ga* beam.

An interesting phenomenon, observable with the *Au* ion beam but not the *Ga* beam, is the effect of the ambient magnetic field on the ion trajectories. The electrostatic fields in the ion gun, and the ambient magnetic field in the vacuum chamber, combine to form a sort of $\mathbf{E} \times \mathbf{B}$ filter. The result is two focused beams, one composed of Au^{+} and the other of Au^{++}, striking the target at slightly different locations. This

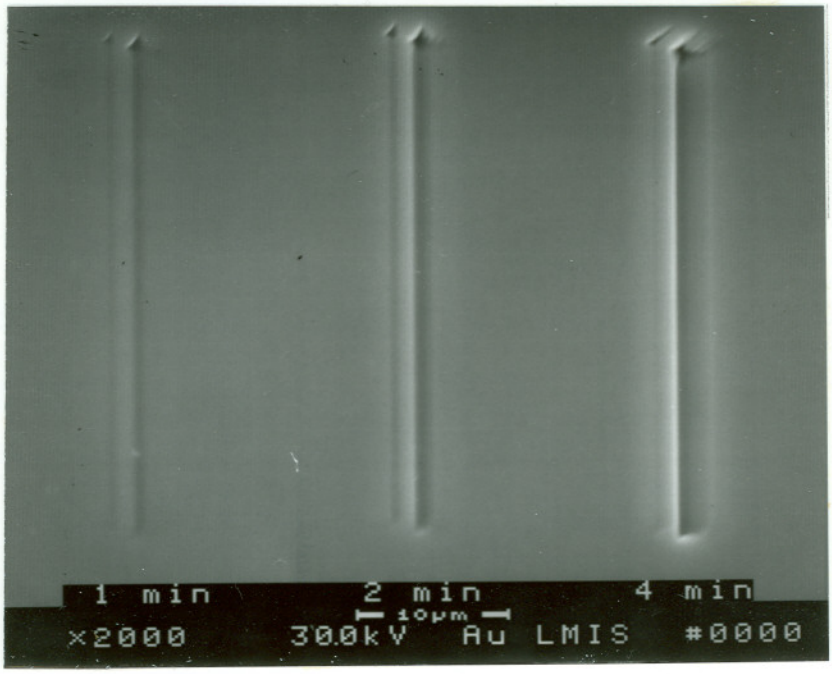

Fig. 1 - 3. Double lines produced in *GaAs* by the *Au* LMIS. The ion gun accelerating potential was 25 kV.

phenomenon was observed in two different ways. First, when imaging the sample the two beams formed two different, overlapping images, one slightly offset from the other. Also, when machining single line scans, two parallel lines were produced spaced about 1.5 µm apart. An example of this is shown in Fig. 1 - 3. A similar effect was seen by Komuro et al. using a *Sn* ion source[80]. This phenomenon makes the *Au* source unsuitable for most FIBM applications.

C. The Vacuum System.

The vacuum chamber of an Amray Inc. model 1830 SEM was modified to accept the ion gun[81]. The ion and electron columns were

aligned so that the same point on the target could be imaged with either gun without changing the target position. With the ion beam normally incident on the target, the electron beam was incident at approximately a 60^0 angle.

Unfortunately, the point at which the two beams met was at a working distance of about 30 mm with respect to the electron beam. The position of this point was limited by the geometry of the vacuum chamber and the size and shape of the ion gun. The long working distance degraded the SEM resolution, but it was still an improvement over the ion beam. Decreasing the SEM working distance to improve resolution meant the area being machined was no longer in the field of view. The ion gun working distance was also quite large, but for the single lens ion gun the beam diameter is not strongly dependent upon the working distance, so this was not an important factor.

One big improvement in the second generation system was the amount of time required for exchanging samples, about 5 minutes in the new system compared to about 8 hours for the old. The main sample chamber in the new system was roughed out with a rotary mechanical pump, and then pumped with an oil diffusion pump equipped with an LN_2 cold trap. Both the ion and electron guns were differentially pumped by their own independent ion pumps, and were equipped with isolation valves which allowed the main chamber to be vented while the two gun

chambers remained under vacuum. The operating pressure in the gun chamber was in the mid 10^{-7} torr range for both guns, and the cold cathode gauge on the sample chamber showed the pressure was less than 1×10^{-6} torr.

The sample stage in the second generation system was another improvement over the first system. The new stage had the same degrees of freedom as the old, but the range of motion of each degree of freedom was much larger. Most importantly, the stage could be tilted up to 90°, so the angular dependence of the sputtering yield could be determined for a wider range of angles than had been possible in the first system.

D. Scan Electronics.

As with the first generation system, the second generation system had two methods for scanning the ion beam. For real time imaging, the electron beam was blanked and the SEM scans, properly conditioned to drive the ion beam, were used to operate the ion gun as a scanning ion microscope. The scan rate could be varied from about 2 frames per second for real time imaging, to several minutes per frame for taking micrographs. In addition, a VAXLab minicomputer, interfaced to a CAMAC crate, was available for beam control[82]. The CAMAC crate contained D/A converters that could control the beam directly, or could

control the output of two analog ramp generators, which in turn controlled the beam.

In practice, the CAMAC crate was too slow to allow direct control of the beam, so the standard mode of operation used the CAMAC crate to control the analog ramp generators. Simple programs were written to set the output of the D/A converters, which in turn determined the amplitude, frequency, and DC offset of the analog ramps. Using this technique, simple lines and rectangles, suitable for the measurement of sputtering yields, could be machined. It was also possible to make more complicated structures by overlapping these features, as mentioned earlier. Unfortunately, it was not possible to continue experimenting with vector scanning.

E. Video Electronics.

The SEM particle detector and associated video electronics were used for real time imaging with either beam. A scintillator and photomultiplier tube were used to detect secondary electrons, but there was no facility for detecting the secondary ions produced by the ion beam. The video signal from the detector was amplified, digitized, and stored in a frame buffer with a resolution of 512 by 512 pixels. The contents of the frame buffer were continuously displayed on a composite video monitor, which acted as the real time display. In standard fast scan mode, the image in

the frame buffer was updated 5 times per second, so real time focusing and astigmatism correction could be done using the digital image. The SEM imaging electronics also provided the ability to do some simple image processing such as image averaging, and gamma correction.

More advanced image processing could be done using the minicomputer, which was equipped with a frame buffer manufactured by Data Translation Inc.[83]. The composite video from the SEM frame buffer was supplied to the microcomputer frame buffer, where it was digitized and made available for manipulation by the computer. Programs could be written to manipulate images in any fashion desired, and images could be written to disk for later retrieval. This capability was most useful when trying to study sputter crater evolution.

The use of the SEM to study the machining process was complicated by the secondary electrons produced by the ion beam. These electrons acted as a source of noise in the electron beam image, and dramatically reduced the signal to noise ratio in the SEM image. It was possible to overcome this to some extent by increasing the amount of current in the electron beam, but increased current degraded image resolution. To use the SEM to monitor the micro-machining process, an alternate approach had to be developed.

The best method for observing the machining process was to periodically blank the ion beam, use the SEM to capture an image, and

then unblank the ion beam to continue machining. Repeating this process at regular intervals allowed the monitoring of the machining process without the interference caused by the ion induced secondary electrons. Additionally, the stored SEM images could be routed to the frame buffer in the minicomputer, and stored for later retrieval. After storing several images, they could be recalled in rapid succession showing the evolution of the sputter crater. This time lapse animation process had the advantage of condensing the time evolution of the sputter crater, making changes which were too gradual to notice in real time much more dramatic.

2. Experimental Technique

Over the years, a wide variety of techniques have been employed to measure sputter yields. This chapter presents a brief discussion of some of those techniques, and looks at their applicability to the case of finely focused ion beams. As will be seen, only one technique lends itself to FIBM. Next, the experimental parameters which can affect sputter yield measurements are discussed. Following this, a brief outline of the experimental procedure is given. Sample preparation and sputter crater measurement are discussed. Finally, the sources of error, and estimates of their magnitudes for a typical sputter crater, are presented.

I. Measurement Techniques.

The sputter yield is defined as the ratio of the number of sputtered target atoms to the number of incident ions.

$$Y = \frac{Sputtered\ Particles}{Incident\ Ions} \qquad 2 - 1$$

To accurately measure the yield, one must accurately measure these two quantities.

A. The Number of Ions.

Measurement of the total number of ions is generally quite simple. The beam current, measured as a function of time, is integrated over the exposure time of the target. For a typical exposure time of about 30 minutes the beam current of a LMIS is quite stable, so the integration becomes a multiplication of the beam current times the exposure time, corrected for the average charge per ion. The correction factor is included to account for the different charge species emitted from the LMIS. As noted earlier, the ions emitted from a *Ga* LMIS are almost 100% Ga^+, so the average charge per ion is very close to 1, but the *Au* beam is composed of two different charge species, Au^+ and Au^{++}, whose relative abundance depends on the total emission current of the LMIS. Their relative abundance must be taken into account when calculating the total number of ions.

B. The Number of Sputtered Particles

Determination of the number of sputtered particles is less straight forward, several techniques have been used by many different people. Perhaps the simplest technique is measuring the mass loss of the bombarded target. Typically, a quartz crystal oscillator is coated with a thin film of the material of interest, which is then partially sputtered away. Assuming the mass loss is uniformly distributed over the surface of the crystal, the change in mass of the film is measured as a change in frequency of the oscillator. Unfortunately, this technique is not well suited to the present circumstances. In FIBM the mass loss is concentrated in an area that is typically some tens of square microns, much smaller than the size of the oscillator, so the change in frequency of the oscillator will not accurately reflect the change in mass. If a larger area is bombarded, the measured yield is not representative of the FIBM process.

Another possible technique involves sputtering through a thin film of known thickness. The resistance between two points, the absorbed current, or the composition of the sputtered material can be used as an indication that the film has been sputtered through. Again, there are several problems associated with this technique. The kinetics of the ion-solid interaction depend on the choice of substrate material, so the

atomic mass of the substrate should closely match that of the thin film. There is also the problem of ion mixing, which smears the interface between layers making it difficult to determine when the film is sputtered through. Also, one must assume that the properties of the thin film, primarily the density and crystallinity, are the same as those of the bulk material. These problems are common to all sputter yield measurements made using this technique, but there is also a problem unique to FIBM.

In broad beam ion etching of a polycrystalline material, the area being machined includes a large number of crystal grains with a wide variety of different orientations, so the effects of crystal orientation are averaged out. The polycrystalline film approximates an amorphous film. This is no longer the case for FIBM, where the size of the machined area can be comparable to the grain size of the film, making the measured yield strongly dependent on the orientation of the particular grain(s) being sputtered. In order to get reproducible results, the film must be truly amorphous, or a single crystal. This is one of the reasons for choosing single crystal target materials for this work.

Finally, a wide variety of methods have been developed for directly measuring the depth of the sputter crater. Some of the possibilities include interference microscopy, profilometry, and mechanical cross sectioning. In the present case, profilometry and interference microscopy cannot be used because of the shape of the sputter craters being

measured. Large incident angles produce craters that have a significant amount of undercutting which is not detectable using profilometry or interference microscopy. Given the nature of the materials being studied and the available equipment, the mechanical cross sectioning technique is best suited to the current situation. It gives a clear view of the crater's profile, including any undercut regions, and allows for an accurate reconstruction of the shape of the crater. This is particularly important when trying to machine the complicated structures typically needed in the fabrication of opto-electronic devices.

Several different methods were available for cross sectioning, the most obvious being the use of the ion beam itself. This idea was discarded, however, because of the large number of craters which needed to be sectioned, and the amount of time needed to section through each crater. Lapping through the craters was also a possibility, but again would have been very time consuming, given the small size of the features being sectioned. The fastest method available was to cleave the samples along a crystal plane that passed through the machined features. As explained below, by properly scribing the samples before machining and carefully aligning the sputter craters relative to the scribe, the sample could be fractured, revealing the cross sectional shape of the sputter craters. This is the technique used in all of the sputter yield measurements described below.

II. Experimental Considerations.

The main purpose of this work is to measure the effect of ion energy and angle of incidence on the sputtering yield, and compare the measured yield to the predictions of the linear cascade theory. But, there are other parameters which may affect the yield. To ensure reproducible results, it must be determined what these parameters are. Possibilities include: the ion dose, which affects the surface composition of the target and in the case of single crystal targets the crystallinity of the target; sputter crater size and shape, which determine the importance of redeposition; crystal orientation of the substrate, which can affect the probability of ion channeling; and the beam scan velocity, which may incorporate several of the above effects.

A. Ion Dose.

One effect of ion implantation is the formation of an altered layer at the target surface. The composition of this layer depends on the ion dose, the rate of ion implantation, the rates at which implanted ions and target atoms are sputtered, and the rate of diffusion of the implanted ions away from the bombarded area. For multicomponent targets preferential sputtering and radiation enhanced diffusion of the target constituents also affect the composition. As the composition of the altered layer

changes, the magnitude and composition of the sputtered flux will also change, since sputtered atoms originate in the top 1 or 2 monolayers of the target[84]. Several attempts have been made to describe altered layer formation. One of the most complete treatments is that of Ho[85].

Altered layer formation was observed in the sputtering of both *GaAs* and *Si*, although the effect was most pronounced for Ga^+ bombardment of *GaAs*. For this particular ion/target combination, altered layer formation was observed quite readily in the form of *Ga* rich droplets on the bottom of the sputter crater. This is illustrated in part (a) of Fig. 2 - 1. The threshold dose for droplet formation depended on a variety of factors, including ion dose, energy, and angle of incidence. Droplet formation has been seen by other investigators for ion bombardment of both *GaAs* and *InP* using a variety of ion sources[86-89]. Similar but less dramatic changes have been noted for In^+ and Ga^+ bombardment of *Si* targets[86,90].

Because Ga^+ bombardment of *GaAs* showed the most obvious effects of altered layer formation, this system was chosen to test the effects of ion dose on the sputtering yield. The results are illustrated in Fig. 2 - 2(a), which shows that for a shallow sputter crater, where redeposition is not significant, the yield remains constant over a fairly wide range of doses. This is not surprising, as the composition of the

Fig. 3 - 1(a). Droplet formation in the bottom of a sputter crater caused by Ga^+ bombardment of *GaAs*.

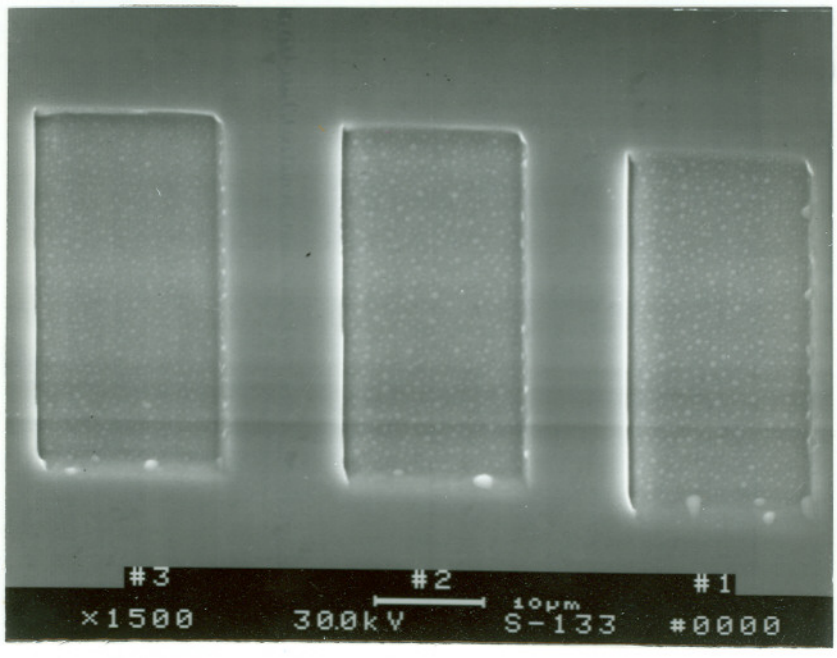

Fig. 3 - 1(b). Amorphization of *Si* by Ga^+ implantation. The amorphized region is less dense than the surrounding crystalline material, and is actually raised above the surrounding surface.

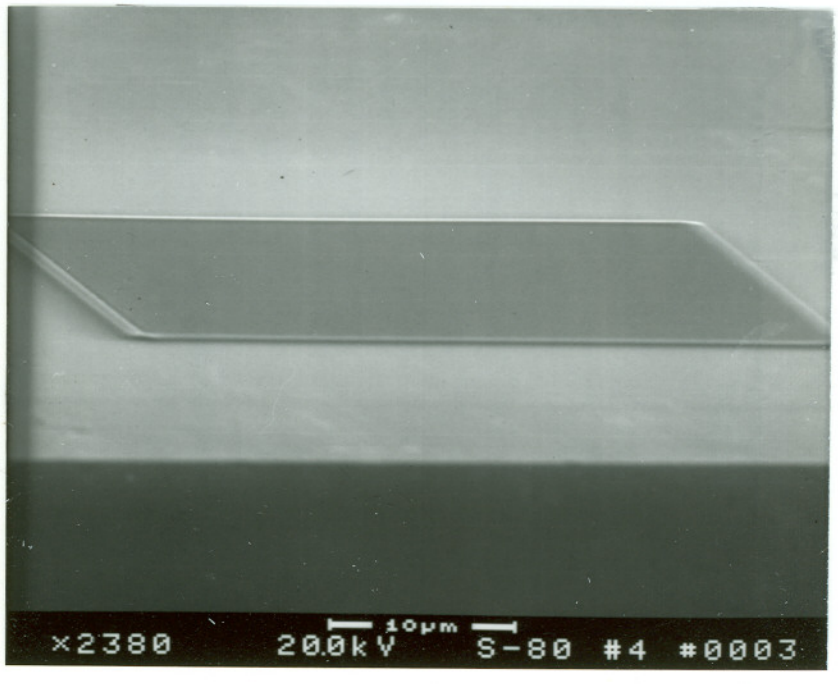

altered layer probably equilibrates at a doses much smaller than those used to create typical FIBM sputter craters[85].

A second effect of ion dose is amorphization of the target by the implanted ions. This can affect the yield in two ways. First, if ion channeling significantly affects the sputtering yield, ion dose can affect the yield through a change in channeling probability associated with target amorphization. It will be shown in the following chapter that, for FIBM of *Si* and *GaAs*, the crystallinity of the target does not significantly affect the sputtering yield, so channeling can be ignored.

Amorphization of the target can also lead to lattice expansion, as was observed for Ga^+ bombardment of *Si*. This is illustrated in Fig. 2 - 1(b), and is caused by the difference in density between the crystalline and amorphous phases of *Si*. The same effect was observed for higher energy *Si* implantation into single crystal *Si* substrates, where it was reported that a dose of about 1×10^{15} ions/cm^2 created a region which was raised above the original surface by 5 to 10 nm[91]. Because the increase in volume is negligible, compared to the volume of the sputtered material, this effect was ignored in the sputtering yield calculations for *Si*. Lattice expansion was not observed for *GaAs*.

B. Sputter Crater Size and Shape.

The size and shape of the sputter crater can also affect the measured sputter yield through redeposition of sputtered material and self focusing of the ion beam. Redeposition is important for high aspect ratio craters. As the crater depth increases, the solid angle subtended by the opening at the top of a crater decreases, decreasing the escape probability of sputtered atoms. Sputtered atoms which cannot escape are redeposited within the crater, resulting in a net decrease in the measured yield.

To illustrate the effects of redeposition, an experiment was performed in which the same ion dose was used to machine a series of rectangular sputter craters with low aspect ratios, and a series of single line scans with high aspect ratios. The results are plotted in Fig. 2 - 2, which shows that the yield is constant over a fairly large range of doses for low aspect ratios, but drops off quite rapidly with increasing dose for high aspect ratios.

Self focusing of the ion beam is another effect which is related to sputter crater size and shape. It also occurs in high aspect ratio craters, where incident ions are reflected from the crater walls, and focused towards the center of the crater, which becomes anomalously deep. Because self focusing affects the crater shape, redeposition may become more pronounced, resulting in a net decrease in the yield. Conversely,

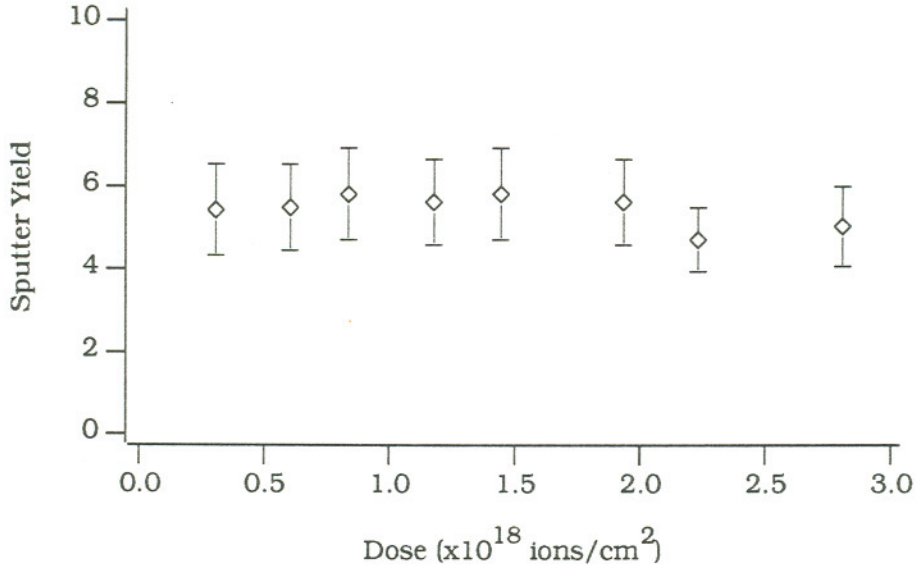

Fig. 2 - 2(a). Plot of the sputter yield as a function of the ion dose for a series of low aspect ratio sputter craters created by Ga^+ bombardment of *GaAs*. The crater aspect ratios were all less than 1, and the yield was fairly independent of dose.

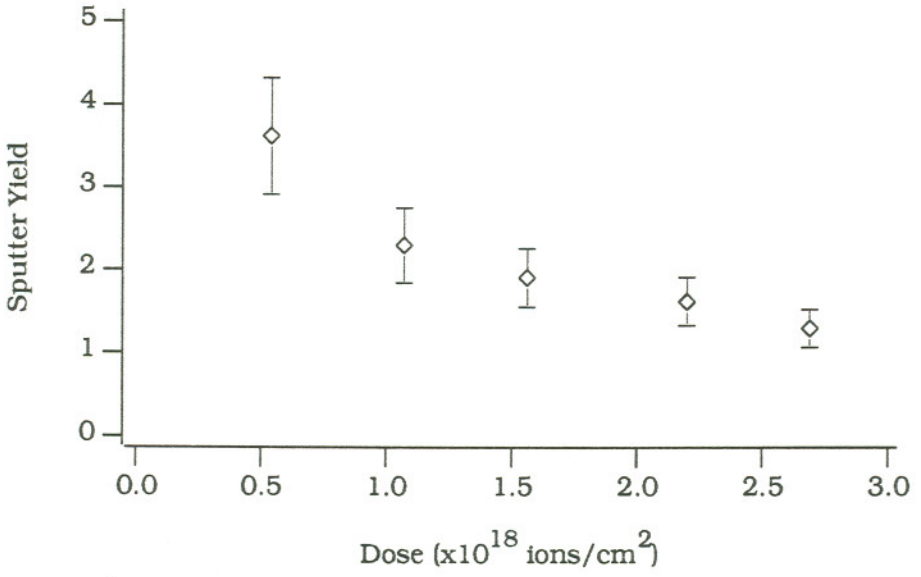

Fig. 2 - 2(b). Ion doses similar to those used above, were used to create a series of high aspect ratio sputter craters, to show the effects of redeposition on the measured yield. The aspect ratios were all greater than 1, and the yield decreased rapidly with increasing dose.

repeated reflection of ions from the crater side walls increases the amount of energy deposited near the target surface, where it will be most efficient in creating sputtered particles. This may result in an increased yield. The net effect on the yield will be determined by which of these phenomena dominates. As seen in Fig. 2 - 2(b), for the case of single line scans, redeposition is the dominant effect.

C. Crystal Orientation.

The crystal orientation of the target material may be important because of ion channeling, which can have a significant impact on the sputtering yield[92]. The effects of channeling should be detectable in two ways. First, if channeling is significant the yield should not be a smooth, monotonically increasing function of the angle of incidence. The sputter yield as a function of incident angle should have local minima at angles where channeling is occurring. Second, for a single crystal target, the sputter yield should change depending on the crystal orientation of the sample, eg. the sputter yield of (100) oriented *Si* should be different from that of (111) oriented *Si*. Neither of these effects was observed, so it appears that crystal orientation does not significantly affect the sputtering yield. The lack of channeling should not be surprising, as the target materials are amorphized at very small ion doses, relative to the

those typically used in FIBM. This will be discussed in more detail in the following chapter.

D. Beam Scan Velocity.

The effects of scan velocity on sputter crater evolution were first reported by Yamaguchi et al., who demonstrated that the scan velocity of the ion beam has a significant effect on the shape of a sputter crater, and the measured sputter yield[76,77]. The yield measured for a crater created with a single slow scan of the beam was much larger than that measured for a crater created with the same ion dose, but with the ions delivered in a series of fast repeated scans. In addition, the single slow scan resulted in a sputter crater with a very nonuniform and nonreproducible profile.

Yamaguchi attributed the increased yield to the angular dependence of the yield, amorphization of the target material, and a reduction in the binding energy of target atoms due to chemical effects of the implanted ions. The most important of these effects is probably the angular dependence of the yield. During sputtering of the target surface, the incident angle of the beam will change as the surface evolves. As will be seen below, for angles less than about 70^0 the sputter yield is a monotonically increasing function of the incident angle, so the evolution

of the target surface will most likely lead to an increase in the sputter yield.

Contrary to the conclusions of Yamaguchi et al., amorphization probably doesn't contribute to the increase. It would be important if channeling had a significant effect on the sputter yield, but as will be shown below this is not the case.

The nonuniformity in the shape of the crater was explained in terms of redeposition of sputtered material. The effects of redeposition are enhanced for a sputter crater created with a single slow scan, because there is no opportunity for the ion beam to return to a previously exposed area and remove the redeposited material. This is not the case for a crater created with repeated fast scans, where the beam continually returns to remove the redeposited material. The result is that a crater created with a single slow scan of the beam will have a significant amount of material redeposited inside the crater, while a crater created with many rapid scans will not.

A factor not mentioned by Yamaguchi et al., is that redeposition may affect the net sputter yield. For craters created with a single slow scan of the ion beam, very few if any ions are used to sputter away redeposited material. For craters created by repeated fast scans, a certain fraction of the incident ions will be used to sputter away material that was redeposited on previous scans of the beam, ions which would sputter

away new material in the case of a single slow scan. The result is that for fast repeated scans the net sputter yield is less than for a single slow scan, but the total number of sputtered atoms is very similar.

The majority of the work reported by Yamaguchi et al. involved the sputtering of *Si* by 30 keV Ga^+ ions, while the current work concentrates on the sputtering of *GaAs*. To test the effects of scan velocity on the sputtering of *GaAs*, experiments similar to those carried out by Yamaguchi were repeated for 20 keV Ga^+ bombardment of *GaAs*. For all of these experiments, beam currents were 0.28 - 0.30 nA, and the total exposure time was 30 min. The size of the sputter crater was about 15 × 30 μm, the same size as a typical sputter crater used in the sputter yield measurements described below.

First, the sputter yield was measured as a function of the total scan velocity over the entire range of values available to the analog ramp generators used in the second generation FIB system. The total scan velocity is defined as the vector sum of the x and y scan velocities. The ion dose was kept constant at about 6.2×10^{17} ions/cm^2, and the pitch of the scan lines was kept constant at 150 nm, about half the beam diameter. The scan velocity was changed by changing the periods of the x and y ramps, while the pitch of the scan lines was kept constant by maintaining a constant ratio between the two periods. The results are plotted in Fig. 2 - 3(a), which shows that over the range investigated the

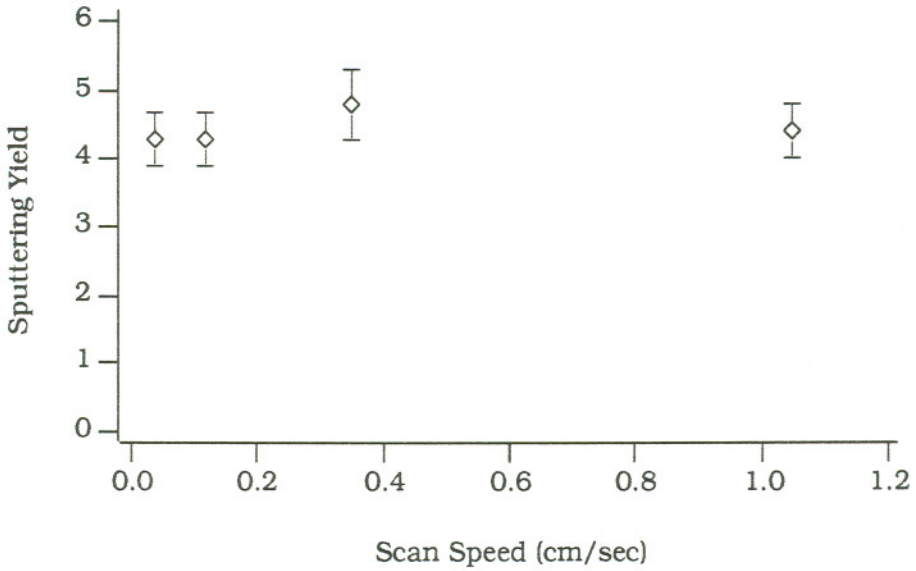

Fig. 2 - 3(a). Sputter yield as a function of the ion beam scan speed. Over the range shown, the sputter yield is independent of the scan speed of the beam.

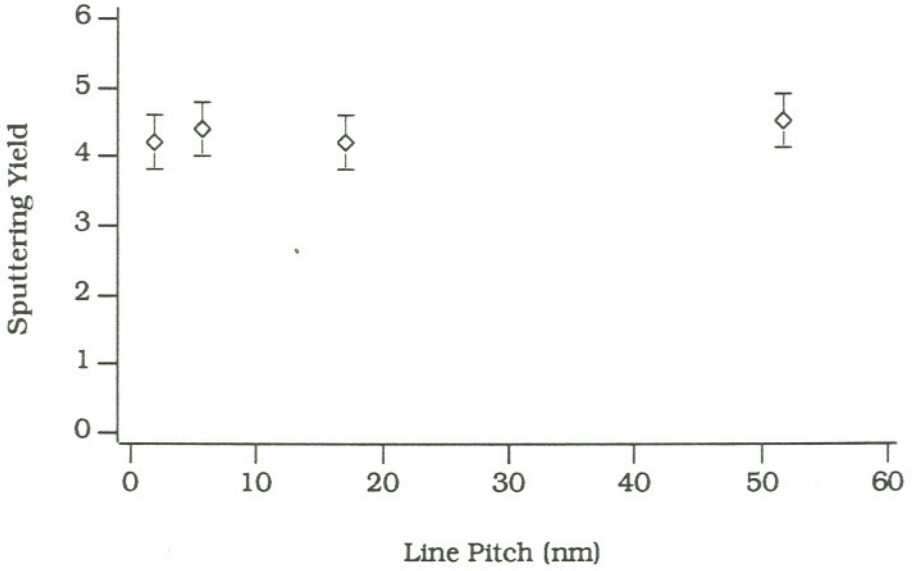

Fig. 2 - 3(b). Sputter yield as a function of the pitch of the scan lines. Over the range shown, the sputter yield is independent of the pitch.

yield is independent of the total scan velocity. This is in good agreement with the results reported by Yamaguchi et al. for Ga^+ bombardment of *Si*.

Next, the sputter yield was measured as a function of the pitch of the scan lines. Here, the period of the y scan was changed while the period of the x scan was held constant. The results of this experiment are shown in Fig. 2 - 3(b), which shows that over the range investigated the sputter yield is independent of the pitch of the scan lines. For this series of sputter craters, the ion dose was kept constant at about 6.9×10^{17} ions/cm^2.

E. Summary.

Of the factors which may affect the sputtering yield, sputter crater size and shape appear to be the most significant. For this reason, a relatively wide, shallow crater was machined when making sputtering yield measurements. The other factors mentioned above, while important under some circumstances, don't appear to affect the sputtering yield for the current set of experimental conditions.

III. Experimental Procedure.

A. Sample Preparation.

The target was a rectangular piece of single crystal *Si* or *GaAs* several millimeters on a side. The *GaAs* samples were cleaved from a single 3" wafer obtained from Tektronix Inc., while the *Si* samples were cleaved from several 4" wafers obtained from Wacker Siltronic Corp.[93,94]. The individual samples were cleaned in acetone and rinsed in ethyl alcohol before being mounted on stainless steel sample holders using a conductive adhesive. No attempt was made to remove the native oxide layer, since the thickness of the oxide layer was negligible compared to the depth of a typical sputter crater, and so had no effect on the sputter yield measurements.

The mounted samples were taken to a scribing machine, where a scribe line several hundred microns long was etched with a diamond stylus. The scribe line allowed the sample to be cleaved into two approximately equal pieces, after it had been machined. The sputter craters were machined at the end of the scribe line, aligned so they would be bisected by the fracture. Typically eight to twelve craters were machined on each sample, the actual number depending on the type of material being machined. For *Si*, the cleaving process was less

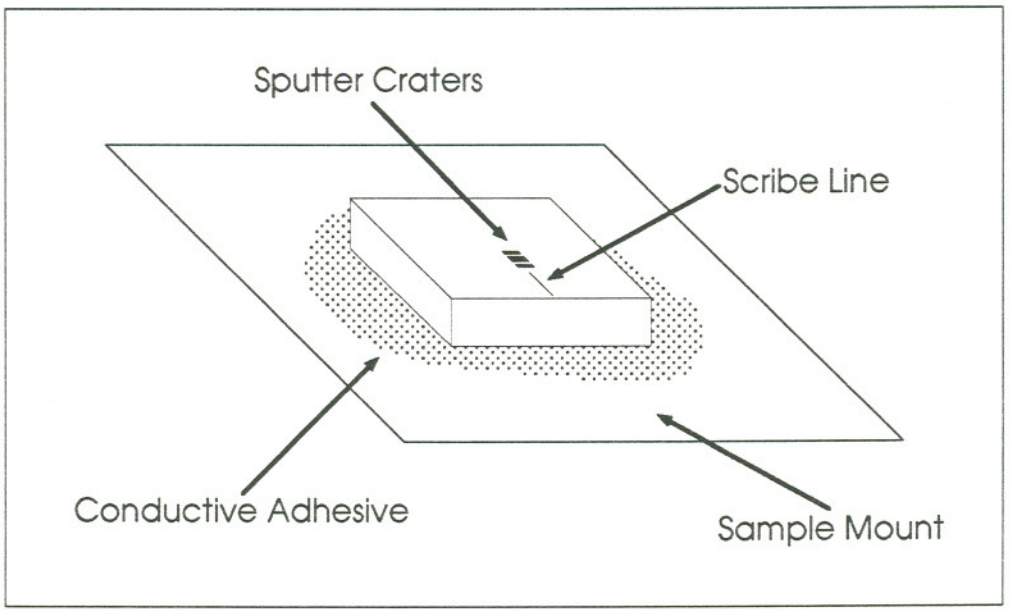

Fig. 2 - 4. Schematic diagram of a typical sample. The scribed piece of *Si* or *GaAs* is mounted to a stainless steel plate with a conductive adhesive, and then mounted on the sample stage of the FIB system.

predictable than for *GaAs*, so the number of sputter craters per sample was kept smaller to minimize the number that were not intersected by the cleave. A schematic diagram of a typical sample is shown in Fig. 2 - 4.

B. Sample Machining.

For sputter yield measurements, the size of a typical sputter crater was about 30 μm long by 15 μm wide, with the depth depending on the target material, ion energy, and incident angle of the beam. The choice of a 30 × 15 μm crater was influenced by several factors. The crater area

was fixed by the amount of time required to sputter a crater of measurable depth: the larger the area, the more time required. For the size chosen, sputter times of 60 minutes for *Si* and 30 minutes for *GaAs* resulted in sputter craters with a minimum depth of about 0.5 μm. The ratio of crater length to width was chosen to make cleaving through the crater as easy as possible, while still avoiding the affects of redeposition. A longer, narrower crater would have been easier to cleave through, but as noted above, for a very narrow crater the affects of redeposition become important.

To keep the crater width and ion dose approximately constant, the amplitude of the y deflection was scaled as $1/cos\theta$, where θ is the incident angle of the beam. The total ion dose was typically between 10^{17} and 10^{18} ions/cm^2.

In the vector scanning experiments, the size and shape of the crater depended on the feature being machined, but some of the same considerations applied. The features had to be small enough to machine in a reasonable amount of time, but large enough to be able to section through. The limited speed of the computer was also a factor. The computer's digital to analog converters were always operated as rapidly as possible to minimize the period of the scan and maximize the scan speed. The maximum possible scan speed was desired in order to avoid the nonlinear effects mentioned previously. Scan speed also influenced

feature size. For a deflection waveform with a fixed period the scan speed scales with the size of the feature, so too small a feature would result in a crater that deviated significantly from the desired shape.

C. Sputter Crater Measurement.

After machining, SEM micrographs were taken of each crater, from which the crater length and width were measured. The sample was then removed from the vacuum chamber, and the conductive adhesive dissolved to detach the sample from the stainless steel sample mount. Next, the scribe line and sputter craters were located using an optical microscope, and the sample was properly oriented for cleaving.

To cleave the sample, it was placed on a firm surface with the machined side down, and covered with a "Kimwipe" laboratory tissue to keep the two halves of the sample from flying apart when the sample actually fractured. Uniform steady pressure was applied at the center of the sample, parallel to the scribe line, using a thin metal shim, such as the back of a scalpel or the blade of a small screwdriver. This method was quite successful when cleaving *GaAs* samples. Almost 100% of the samples cleaved along a smooth straight line that passed through all of the craters. For *Si* samples, the success rate was much lower. The fracture would follow a crystal plane part way across the sample, bisecting some of the craters, before wandering off axis leaving some of

the craters intact. The difference in success rate reflects the different physical properties of the two target materials.

After cleaving, the sample was remounted with conductive adhesive, oriented so the cross section of the sputter craters could be viewed in the SEM, and micrographs were taken showing the cross section of each crater. For sputter yield measurements, the cross sectional area of each crater was measured with a compensating polar planimeter. Each measurement was repeated a minimum of 5 times, and the average was multiplied by the crater length to give the volume. This procedure assumes that the cross section of the crater is constant along its length, which is an approximation, but in general a good one.

D. Beam Current Measurement.

Beam current was measured at the blanking aperture. As described earlier, the aperture and the picoammeter were biased at +300 V to suppress secondary electron emission. Measurements were made immediately before and after sputtering the target, and the average of the two values was used to calculate the total number of ions. The two values were usually within 5% of each other, with the final current generally less than the starting current because of a slow decline in the total emission current typical of a LMIS when operated in the FIB system.

IV. Errors.

The formula used to calculate the sputter yield from the measured parameters was

$$Y = \frac{Length \times Area \times Density}{Ion\ Fluence \times Time} \qquad 2 - 2$$

The crater length and cross sectional area, and the ion fluence are the main sources of error in this equation. Given the length of the average exposure, 30 minutes for *GaAs* targets and 60 minutes for *Si* targets, and the accuracy of the time measurements, typically about 1 sec, the contribution to the error due to time measurements will be ignored. Each possible source of error will be considered in turn. The actual magnitude of the errors varies from crater to crater depending on the size of the crater, and the magnification and quality of the image used to measure it's volume, but in order to illustrate the relative importance of the various errors an estimate will be made of their magnitudes for a typical sputter crater.

A. Errors in Length Measurements.

Length measurements were made using a simple ruler which in principle provided a measurement accuracy of about 0.5 mm. For a typical micrograph with a magnification of about 1500×, a 30 μm long

crater will appear to be 45 mm long, so the apparent accuracy of the length measurement was at worst about 1%. Unfortunately, because the crater edges were not always well defined, the real measurement accuracy was much less. The current density distribution in the beam, beam drift during machining and enhanced edge contrast in the micrographs all contributed to a broadening of the crater edges. In reality, these edge effects contributed an additional uncertainty of 1 to 2 mm to a typical length measurement.

In addition to the measurement accuracy, the accuracy of the micrograph magnification must also be taken into account. This will be dealt with separately, as it also affects the accuracy of the area measurements. The error in magnification is added in quadrature with the measurement error to give the total possible error in the sputter crater length.

B. Errors in Area Measurements.

Area measurements were made with a compensating polar planimeter, with the areas measured being between about 100 and 1000 mm^2. The calibration of the planimeter was checked before each series of measurements and was always found to be accurate to within 1%. This was quite small compared to the other errors which were present, so the calibration error of the planimeter was ignored. In principle, the

planimeter could measure an area to the nearest 1 mm^2, so the apparent error was at most about 1%. But, as with the length measurements, the actual error was larger. The same factors that decreased the accuracy of the length measurements also affected the accuracy of the area measurements.

To insure the reproducibility of the area measurements, each crater was measured at least 5 times. The results were then averaged and a standard deviation was calculated. In cases where the standard deviation of the first 5 values was greater than about 10% of the average area, additional measurements were made until the standard deviation fell below 10%. The standard deviations of about 175 such measurements were averaged, and the result was taken as the measurement accuracy of the planimeter. The average standard deviation was 20 mm^2, so for a typical sputter crate with a cross sectional area of about 500 mm^2, the error in the area measurement was taken to be about 4%. As with the length measurements, the accuracy of the SEM magnification also affected the accuracy of the area measurements.

C. Errors in SEM Magnification.

Obviously, the accuracy of the magnification calibration of the SEM is an important factor in determining the accuracy of the length and area measurements. The magnification was calibrated periodically, using a

series of standards, for operating conditions of 30 kV accelerating voltage and 12 mm working distance. The accuracy of the calibration was generally quite good, and a random check between calibration procedures, under the same operating conditions, showed that after several months of operation, an accuracy of about 5% was maintained. Unfortunately, in the course of taking data it wasn't always possible to reproduce these same operating conditions. The sputter yield data presented below was collected over a period of several months, so normal variations in the optimum operating conditions of the SEM sometimes required a shorter working distance in order to maintain good image resolution. The instrument was designed to compensate for this, but the accuracy of the measurements depended on the accuracy of the compensation.

To check the compensation, photos were taken of the cross section of the same sputter crater for a constant magnification of 5500×, and working distances of 6, 9, and 12 mm. The width of the sputter crater was measured for each micrograph, and the results are summarized in Table 2 - 1. Because the magnification was calibrated for a working distance of 12 mm, the actual width of the crater is taken to be 95 mm with the estimated accuracy of the measurement ± 2 mm. The accuracy of the measurement is limited by the accuracy of the ruler, and the uncertainty in the position of the edges of the sputter crater. These two

Working Distance (mm)	Crater Length (mm)
12	95
9	95
6	93

Table 2 - 1. Measured crater length as a function of the SEM working distance.

sources of error are added in quadrature to find the total possible error in the measurement. All of the width measurements are the same, within the experimental error, so the working distance is not a significant source of error. The accuracy of the calibration of the SEM magnification remains about 5%.

D. Errors in Beam Current.

The final major contribution to the total error comes from errors in beam current measurements. Current measurements were made by connecting a picoammeter to the blanking aperture, and biasing the meter and aperture assembly at +300 V, relative to the surrounding optical column elements, to suppress secondary electron emission. Typical beam currents were about 0.25 nA. The calibration accuracy of the picoammeter was ± 5%, and the meter could in principle measure currents to an accuracy of about 10 pA, or ± 4% of the total current.

Current measurements made using this technique were compared to measurements made using a Faraday cup positioned in place of the

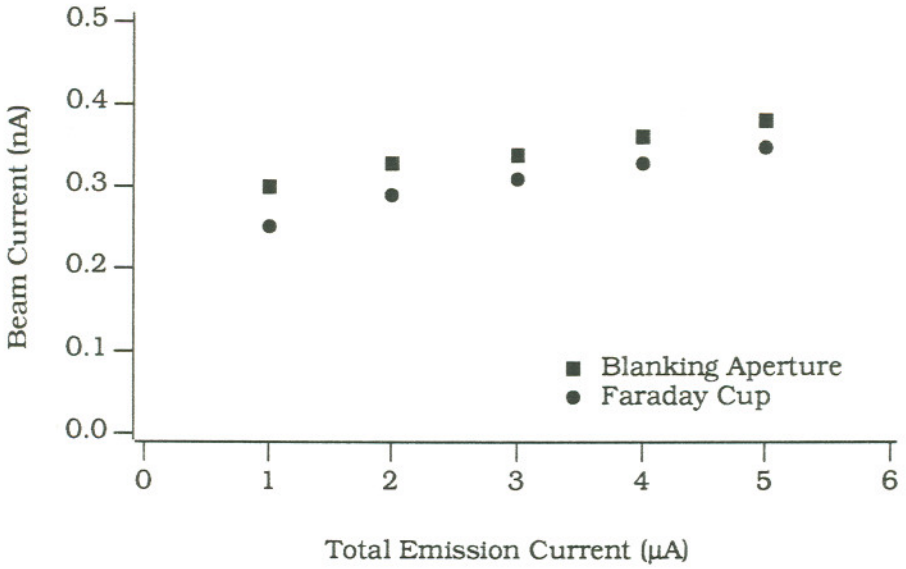

Fig. 2 - 5. Comparison of current measurements made using the blanking aperture and a Faraday cup. The result of the Faraday cup are consistently lower, indicating that the blanking aperture is less efficient at suppressing secondary electrons. The difference in the two measurements is about 10%.

sample. The blanking aperture measurements were consistently higher than those made with the Faraday cup because the aperture was less efficient in suppressing secondary electron emission. The difference between the two measurements was typically about 10%. This is illustrated in figure Fig. 2 - 5, which plots the beam current as a function of the total emission current from the LMIS.

The final source of error in the beam current measurements comes from the instabilities in the total emission current of the LMIS. The total emission current will drift over time as the flow characteristics of the liquid metal on the W needle change. These changes are brought on

primarily by the contamination of the source from material sputtered from the extraction electrode which then redeposits onto the tip. Additionally, electron bombardment of the source from the secondary electrons produced at the extractor can lead to source heating which can also affect the total emission current. The former generally leads to a decrease in current, while the latter probably leads to an increase. More complex processes may also be occurring, but whatever the cause, the change in total emission current of the LMIS is reflected in a change in beam current.

Because of the small fraction of the total current actually used to form the focused beam, changes in the LMIS current are not a very sensitive indication of changes in the beam current. As the total emission current of the LMIS drifted up or down, the beam current also changed in the same direction, but it wasn't possible to quantify the change by simply monitoring the LMIS current. Instead, the beam current was measured immediately before and after machining a sputter crater and the two measurements were averaged. The average value was then used to calculate the total number of ions.

The process of averaging the two measurements assumes that the change in beam current is linear and constant over the entire exposure time of the sputter crater. This was not always true, as changes in the current could take place over time periods smaller than the exposure

time of a typical sputter crater, and may not be exactly linear. The change in current was, however, generally monotonic over the period of a typical sputter crater exposure time, so the two beam current measurements provided an upper and lower limit to the total number of ions. The largest difference between the two measurements was no more than about 4%, so this value will be taken as the contribution to the error in the beam current measurements due to drift in the total emission current of the LMIS.

E. Summary of Errors.

To summarize, the error in the sputter yield measurements can be calculated from

$$\left(\frac{\Delta Y}{Y}\right)^2 = \left(\frac{\Delta l}{l}\right)^2 + \left(\frac{\Delta A}{A}\right)^2 + \left(\frac{\Delta I}{I}\right)^2 \qquad 2 - 3$$

where l is the length of the sputter crater, A is its cross sectional area, I is the primary ion beam current, and the Δ indicates the error in each of these quantities. Each term may be further broken up to show the explicit sources of error.

For the length measurement

$$\left(\frac{\Delta l}{l}\right)^2 = \left(\frac{\Delta l_m}{l_{mm}}\right)^2 + \left(\frac{\Delta l_e}{l_{mm}}\right)^2 + \left(\frac{\Delta M}{M}\right)^2 \qquad 2 - 4$$

where l_{mm} is the length of the sputter crater in mm as measured from the SEM micrograph, M is the magnification of the micrograph, Δl_m is the measurement error of the ruler, Δl_e is the error due to edge effects in the SEM, and ΔM is the error in the magnification. Substituting in the values for the various errors, the error in the length measurements for a typical sputter crater was about 7%.

For the area measurement

$$\left(\frac{\Delta A}{A}\right)^2 = \left(\frac{\Delta A_m}{A_{mm}}\right)^2 + \left(\frac{\Delta A_e}{A_{mm}}\right)^2 + 2\left(\frac{\Delta M}{M}\right)^2 \qquad 2 - 5$$

where A_{mm} is the cross sectional area of the sputter crater in mm^2 as measured from the micrograph, ΔA_m is the measurement error of the planimeter, and ΔA_e is the error due to edge effects. The factor of 2 in front of the magnification error occurs because the area scales as the square of the magnification. For a typical sputter crater the error was about 8%.

Finally, for the current measurement

$$\left(\frac{\Delta I}{I}\right)^2 = \left(\frac{\Delta I_c}{I}\right)^2 + \left(\frac{\Delta I_m}{I}\right)^2 + \left(\frac{\Delta I_{se}}{I}\right)^2 + \left(\frac{\Delta I_d}{I}\right)^2 \qquad 2 - 6$$

where I is the beam current, ΔI_c is the calibration error if the picoammeter, ΔI_m is the measurement error of the picoammeter, ΔI_{se} is the error due to secondary electrons escaping from the blanking

Source of Error	Magnitude
Length Measurement	
Measurement Accuracy	1.1%
Edge Effects	4.4%
Area Measurement	
Measurement Accuracy	0.2%
Edge Effects	4.0%
Beam Current	
Measurement Accuracy	4.0%
Secondary Electrons	10.0%
Drift	4.0%
SEM Magnification	
Measurement Accuracy	5.0%

Table 2 - 2. Magnitude of errors for a typical sputter crater.

aperture, and ΔI_d is the error due to drift in the beam current. Here, the total error was about 11%.

All of the sources of error and their magnitudes are shown in Table 2 - 2. Adding them in quadrature gives the total possible error in the sputter yield measurements, which was about 15%. Note that the values used in this calculation were chosen to be representative of a typical sputter crater, and the actual value for any given crater may be different. Also, in the case of the sputtering of *GaAs*, the sputter yield measurement was repeated 3 times for each set of experimental parameters, so by averaging the 3 different values the error in the measured sputter yield is reduced to about 9%. For *Si*, at least two craters were machined for each set of experimental conditions, so averaging the results reduces the error to about 10%.

3. Sputtering Yields

As mentioned previously, most applications of FIB technology require knowledge of the sputtering yield for the ion/target combination of interest. In mask repair, IC modification, creation of opto-electronic structures, and all other micromachining applications, the depth of a machined feature is determined from knowledge of the sputtering yield. It follows that a method of calculating the yield using existing theories would provide real benefits to the application of FIBM.

Towards this end, a series of experiments was undertaken to measure the sputtering yield of two common target materials, *Si* and *GaAs*. The experimental results were then compared to the predictions of the linear cascade theory of Sigmund[65,95].This is particularly timely, in light of the recent modifications to the theory, which take into account an

improved understanding of how low energy particles interact with a solid during the sputtering process[84,96].

I. The Linear Cascade Theory of Sputtering.

Before presenting the experimental results, a brief overview of the theory will be given.

A. Overview of the Theory.

The linear cascade theory of sputtering was developed to describe the sputtering of amorphous elemental targets by mono-energetic ions. By solving the Boltzmann transport equation for energetic ions in a solid, Sigmund was able to arrive at an expression for the sputtering yield[65]. In the elastic collision regime, i.e. the range of energies where the energy loss of the ion is dominated by elastic collisions, the sputtering yield S as a function of ion energy and incident angle was found to be

$$S(E,\eta) = \Lambda F(0,E,\eta) \qquad 3 - 1(a)$$

The yield is proportional to $F(0,E,\eta)$, the energy deposited by the ions at the surface of the target, where E is the ion energy and η is the direction cosine of the incident ions relative to the surface normal. Additionally, the yield depends on the material dependent constant

$$\Lambda = \frac{3}{4\pi^2}\frac{1}{NC_0U_0} \qquad 3 - 1(b)$$

where N is the number density of the target, U_0 its surface binding energy, which is usually taken to be the heat of sublimation, and C_0 is a constant which arises from the use of a power cross section to describe the scattering of recoiling target atoms. The general form of the power cross section is

$$d\sigma = C_m E^{-m} T^{1-m} dT \qquad 3 - 2$$

where T is the energy transferred to the recoiling particle. For collisions involving particles with energies in the eV range, $m \approx 0$ is a reasonable choice[65]. The same form for the scattering cross section is used in describing the interaction of the incident ions with the target, but with a different choice of m. For the ion energies used in the current experiments, $m = 1/2$ is a good approximation while for lower energies one should use $m = 1/3$[65]. The choice of a power cross section simplifies the process of determining the energy dependence of the sputtering yield, as will be shown below.

For $m = 0$ in Eqn. 3 - 2, the parameter C_0 is defined by

$$C_0 = \frac{1}{2}\pi\lambda_0 a^2 \qquad 3 - 3$$

where a is a Born-Mayer screening radius, and λ_0 is a fitting parameter. Originally, the value for λ_0 was chosen to fit the scattering cross section of Eqn. 3 - 2 to calculations by Robinson, based on a Born-Mayer interaction potential[97]. The fit was based on an extrapolation from the lowest energy interactions for which data was available. Sigmund originally chose $\lambda_0 = 24$ and $a = 0.219$ Å, but recently modified the choice of λ_0 based on calculations of the cross section at lower energies[84]. The extrapolation underestimated the scattering cross section at low energies by about a factor of 2. Based on the results presented in Ref. [84], a value of $\lambda_0 = 50$ was chosen for the current work.

B. Energy Dependence of the Sputtering Yield.

The deposited energy $F(x,E,\eta)$ in Eqn. 3 - 1(a) is roughly Gaussian in shape, especially when the mass of the ion is less than or about equal to the mass of a target atom. This means it can be approximated by an Edgeworth expansion in terms of moments[98,99]. When the result of this expansion is substituted into Eqn. 3 - 1(a), one obtains

$$S(E,\eta) = \frac{\Lambda E}{\langle \Delta x^2 \rangle^{1/2}} \left[\varphi_0(\xi_0) - \frac{1}{6}\Gamma_1 \varphi_3(\xi_0) - \ldots \right] \qquad 3 - 4(a)$$

where

$$\varphi_n = \left(\frac{\partial^n}{\partial x^n}\right)(2\pi)^{1/2}\exp\left(-\frac{\xi^2}{2}\right) \qquad 3 - 4(b)$$

$$\Gamma_1 = \frac{\langle \Delta x^3 \rangle}{\langle \Delta x^2 \rangle^{3/2}} \qquad 3 - 4(c)$$

$$\xi = -\frac{x - \langle x \rangle}{\langle \Delta x^2 \rangle^{1/2}} \qquad 3 - 4(d)$$

$$\xi_0 = -\frac{\langle x \rangle}{\langle \Delta x^2 \rangle^{1/2}} \qquad 3 - 4(e)$$

Comparing Eqn. 3 - 1(a) and Eqn. 3 - 4(a), yields an expression for the deposited energy

$$F(x,E,\eta) = \frac{E}{\langle \Delta x^2 \rangle^{1/2}}\left[\varphi_0(\xi_0) - \frac{1}{6}\Gamma_1\varphi_3(\xi_0) - \ldots\right] \qquad 3 - 5$$

For the power cross section of Eqn. 3 - 2, the moments have the general form

$$\langle x^n \rangle = \left(\frac{E^{2m}}{NC}\right)^n h_n(\eta) \qquad 3 - 6$$

where $h_n(\eta)$ is some function of η. Examining Eqn. 3 - 5, one sees that the first term on the right hand side is proportional to NCE^{1-2m}, which is essentially the nuclear stopping power for the power cross section of Eqn. 3 - 2. The deposited energy can then be written in terms of the nuclear stopping power

$$F(0,E,\eta) = NS_n(E)\,\frac{1}{h_0(\eta)}\left[\varphi_0(\xi_0) - \frac{1}{6}\Gamma_1\varphi_3(\xi_0) - \ldots\right] \qquad 3 - 7$$

Substitution of Eqn. 3 - 6 into Eqn. 3 - 4(e) shows that ξ_0 is independent of the ion energy, which means the term in brackets in Eqn. 3 - 7 is also independent of energy. So, the deposited energy can be written as a product of the stopping power of the ion and some function which depends on the incident angle of the beam, and perhaps the ratio M_2/M_1 and the exponent m.

$$F(0,E,\eta) = NS_n(E)\,\alpha(M_2/M_1,m,\eta) \qquad 3 - 8$$

Substituting Eqn. 3 - 8 into Eqn. 3 - 1 gives

$$S(E,\eta) = \Lambda NS_n(E)\,\alpha(M_2/M_1,m,\eta) \qquad 3 - 9$$

which shows that the energy dependence of the sputtering yield is determined entirely by the energy dependence of the nuclear stopping power.

A power cross section was chosen in Eqn. 3 - 2 for ease of calculation in showing how the sputtering yield depends on the nuclear stopping power. To determine the detailed behavior of the sputtering yield as a function of energy, one should use the most accurate results available for the stopping power. In his original paper, Sigmund used the results

of Lindhard, Nielsen, and Scharff, which are based on Thomas-Fermi theory[65,100]. Since then, refinements have been made based on more realistic forms for the interaction potential and the analysis of experimental results. Recently, Wang et al. used the following expression in their work on ion implantation ranges[101]

$$S_n = 8.462 s_n \frac{M_1}{(M_1 + M_2)} \frac{Z_1 Z_2}{(Z_1^{2/3} + Z_2^{2/3})^{1/2}} \qquad 3 - 10(a)$$

where

$$s_n = 0.5 \frac{\ln(1 + \varepsilon)}{(\varepsilon + 0.10718\varepsilon^{0.37544})} \qquad 3 - 10(b)$$

and

$$\varepsilon = 32.53E \frac{M_2}{M_1 + M_2} \frac{Z_1 Z_2}{(Z_1^{2/3} + Z_2^{2/3})^{1/2}} \qquad 3 - 10(c)$$

In Eqns. 3 - 10, M_1 and M_2 are the mass of the ion and the target, respectively, Z_1 and Z_2 are their atomic numbers, and E is the energy of the ion in keV. This is the energy dependence used in the sputtering yield calculations done below.

There are two important points to consider regarding the above discussion. First, the expression used for the stopping power does not take into account the effects of ion channeling. Application of the linear cascade theory is usually limited to ion bombardment of amorphous

targets. Second, the stopping power does not account for altered layer formation which occurs under high fluence ion bombardment. In addition to influencing the stopping power, this may also change the surface binding energy, which appears in Eqn. 3 - 1(b). For these reasons, it would seem that the linear cascade theory is not applicable to the current experimental conditions.

C. Angular Dependence of the Sputtering Yield.

Sigmund also derived an expression for the angular dependence of the sputtering yield. Using Eqns. 3 - 4 and the relationship between the moments in the coordinate system of the ion, and the coordinate system of the sample

$$\langle x \rangle = \eta \langle X \rangle \qquad 3 - 11(a)$$

$$\langle x^2 \rangle = \eta^2 \langle X^2 \rangle + (1 - \eta^2)\langle Y^2 \rangle \qquad 3 - 11(b)$$

$$\langle x^3 \rangle = \eta^3 \langle X^3 \rangle + 3\eta(1 - \eta^2)\langle XY^2 \rangle \qquad 3 - 11(c)$$

an expression for the variation of the sputtering yield with η is obtained.

$$\frac{S(E,\eta)}{S(E,1)} = \left(\eta^2 + (1 - \eta^2)\frac{\langle Y^2 \rangle}{\langle \Delta X^2 \rangle}\right)^{1/2} \exp\left[\frac{\langle X^2 \rangle}{2\langle \Delta X^2 \rangle}\left(1 + \frac{\eta^2}{1 - \eta^2}\frac{\langle \Delta X^2 \rangle}{\langle Y^2 \rangle}\right)^{-1}\right] \qquad 3 - 12$$

where $S(E,1)$ is the sputtering yield at normal incidence. For $\eta \approx 1$ the above equation can be approximated by

$$\frac{S(E,\eta)}{S(E,1)} = \eta^{-f} = (\cos\theta)^{-f} \qquad 3 - 13(a)$$

where

$$f = 1 + \frac{\langle Y^2 \rangle}{\langle \Delta X^2 \rangle}\left(\frac{\langle X \rangle^2}{\langle \Delta X^2 \rangle} - 1\right) \qquad 3 - 13(b)$$

The value of f depends on the indicated moments, which in turn depend on the choice of m in Eqn. 3 - 2. Sigmund shows that $f = 5/3$ is a good approximation for $M_2/M_1 \leq 3$, independent of the choice of m. At grazing incidence, the assumption $\eta \approx 1$ is no longer valid, so the predictions of Eqn. 3 - 13 no longer hold true.

Returning to Eqn. 3 - 9, the sputtering yield as a function of ion energy and incident angle can be written as

$$S(E,\theta) = \Lambda N S_n(E)\,\alpha(M_2/M_1, m)(\cos\theta)^{-5/3} \qquad 3 - 14$$

The only unknown quantity here is $\alpha(M_2/M_1, m)$, whose functional form has its origins in the Edgeworth expansion of the deposited energy function. The accuracy with which α can be determined depends on the accuracy of the expansion. In his original work, Sigmund presents a numerical result for $\alpha(M_2/M_1, m)$, and shows that the dependence of α on

m is not significant, given the limited accuracy of the power cross section in Eqn. 3 - 2[65]. In a later work, Sigmund compares the numerical result to experimental results, and shows good agreement for mass ratios less than about 3[102].

II. Experimental Results.

Sputtering yield measurements were made, using a *Ga* FIB, for three different target materials, single crystal (100) oriented *Si* and *GaAs*, and single crystal (111) oriented *Si*. For comparison, a *Au* FIB was also used to sputter (100) oriented *GaAs*. The variation of the yield with ion energy, and incident angle was investigated. The results for ion bombardment of *Si* were obtained prior to the results for *GaAs*, but the *GaAs* results are presented first because they are more complete.

A. Ga^+ *Bombardment of (100) Oriented* GaAs.

Twelve different samples were bombarded, three samples each at energies of 10, 15, 20, and 25 keV. Eleven or twelve craters were sputtered on each sample, with the incident angle of the beam varying between 0^0 and 85^0. The results of these experiments are summarized in Fig. 3 - 1 through Fig. 3 - 4, which plot the sputtering yield as a function of incident angle for each sample, as well as the average over the three samples machined at each energy. The plots of the average sputtering

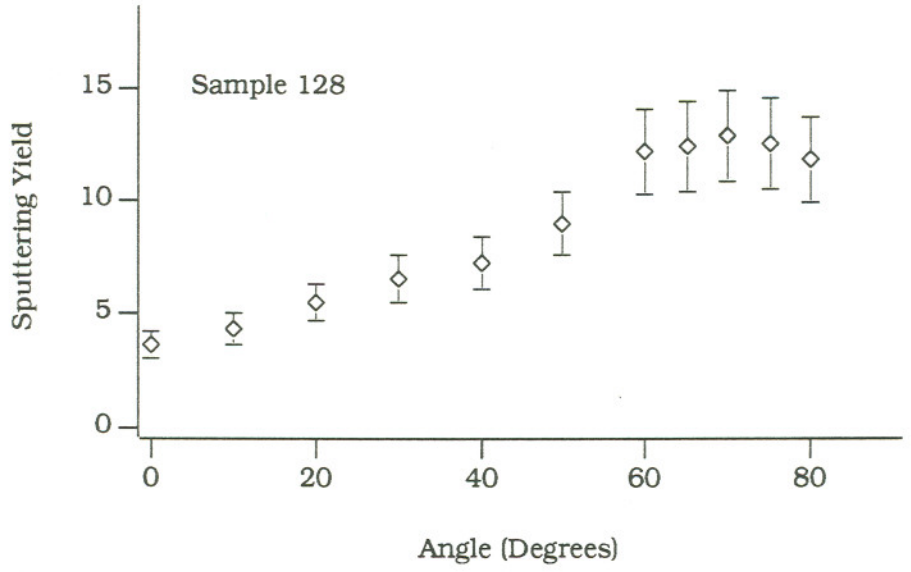

Fig. 3 - 1(a). Plot of the sputter yield as a function of incident angle for 10 keV Ga^{+} ions incident on (100) oriented *GaAs*.

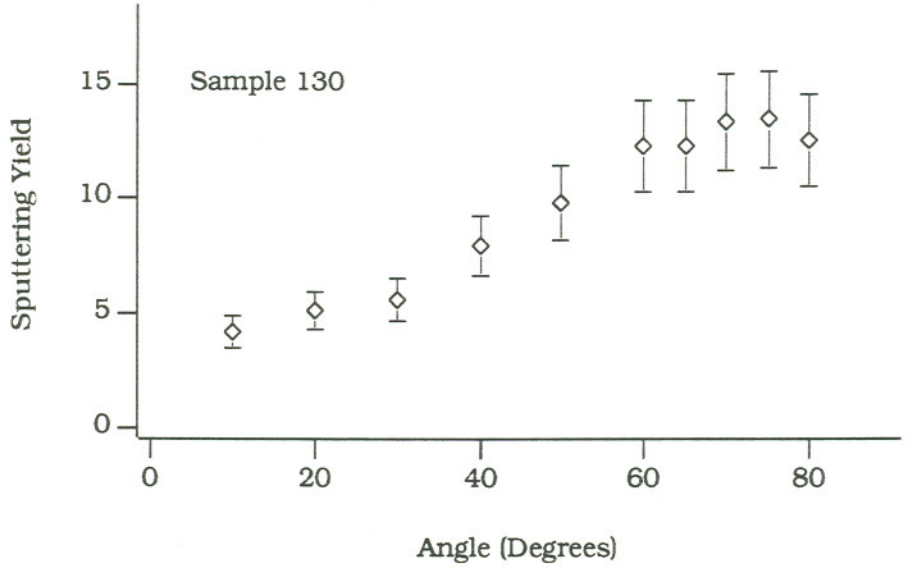

Fig. 3 - 1(b) Plot of the sputter yield as a function of incident angle for 10 keV Ga^{+} ions incident on (100) oriented *GaAs*.

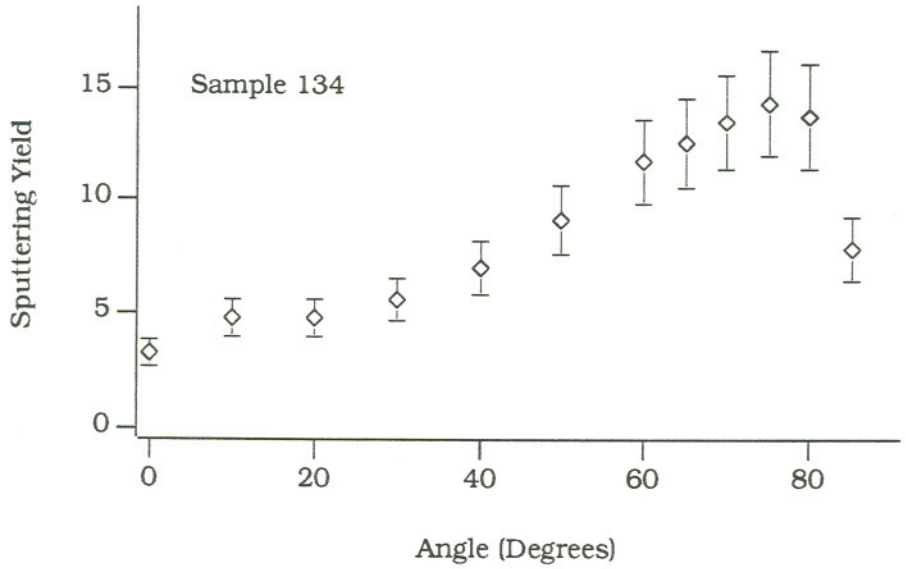

Fig. 3 - 1(c). Plot of the sputter yield as a function of incident angle for 10 keV Ga^+ ions incident on (100) oriented *GaAs*.

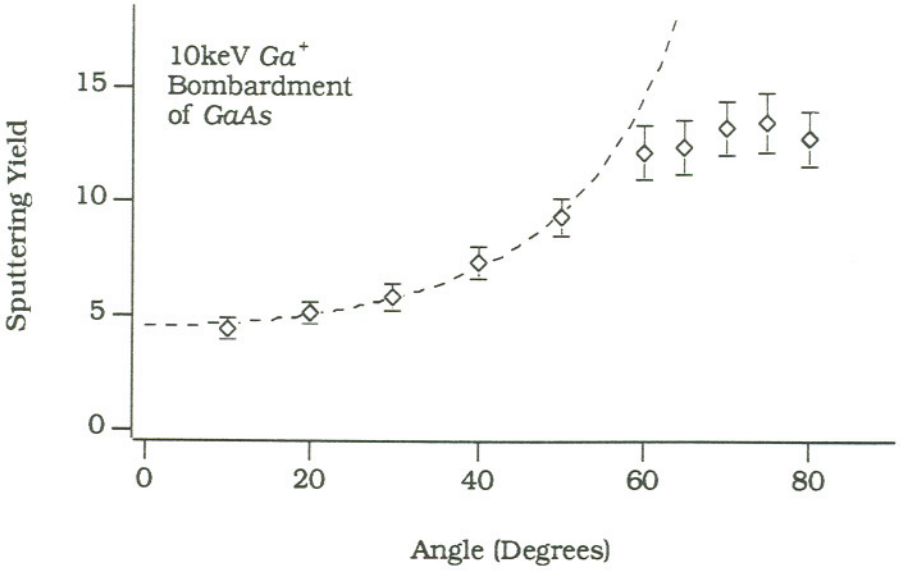

Fig. 3 - 1(d). Average of the results presented in parts (a) through (c). The dashed line represents the angular dependence predicted by the linear cascade theory, which agrees well with the experimental results.

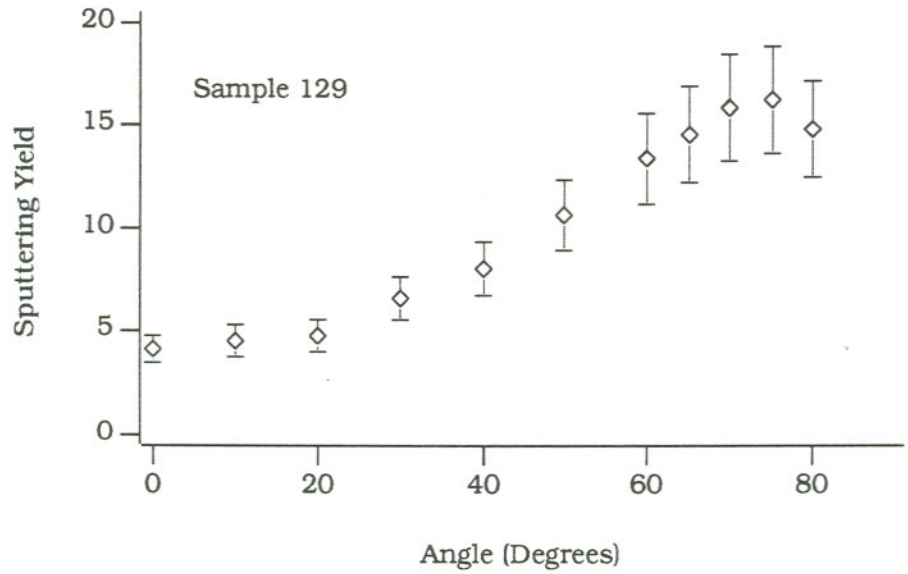

Fig. 3 - 2(a). Plot of the sputter yield as a function of incident angle for 15 keV Ga^+ ions incident on (100) oriented *GaAs*.

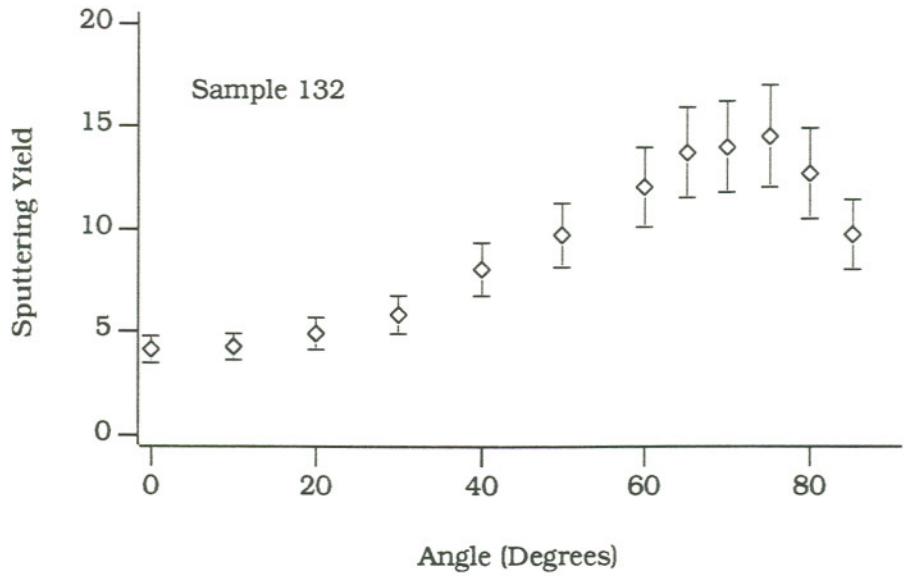

Fig. 3 - 2(b). Plot of the sputter yield as a function of incident angle for 15 keV Ga^+ ions incident on (100) oriented *GaAs*.

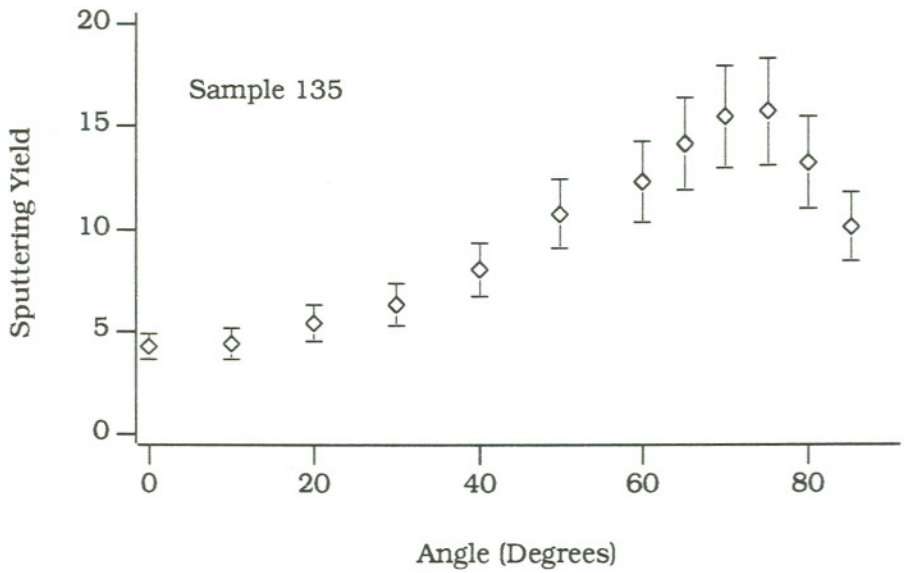

Fig. 3 - 2(c). Plot of the sputter yield as a function of incident angle for 15 keV Ga^+ ions incident on (100) oriented *GaAs*.

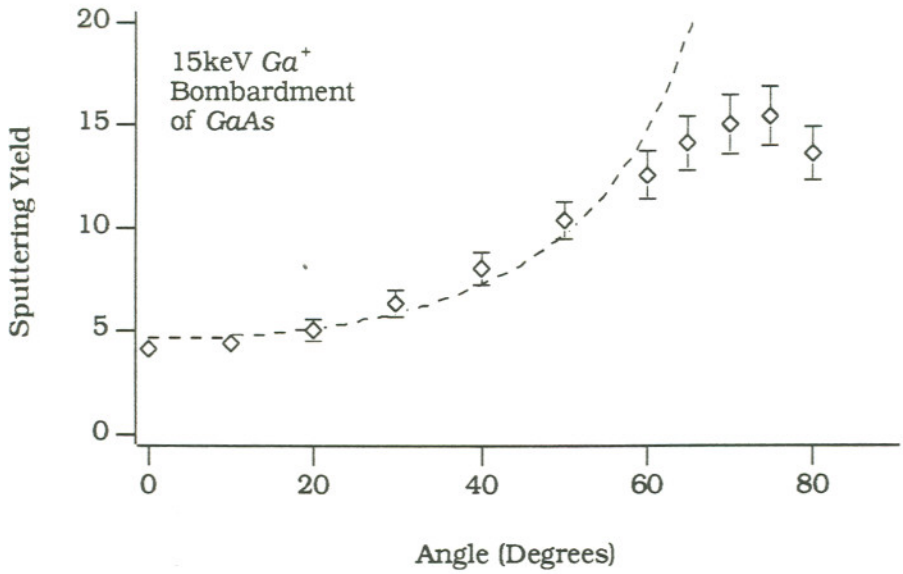

Fig. 3 - 2(d). Average of the results presented in parts (a) through (c). The dashed line represents the angular dependence predicted by the linear cascade theory, which agrees well with the experimental results.

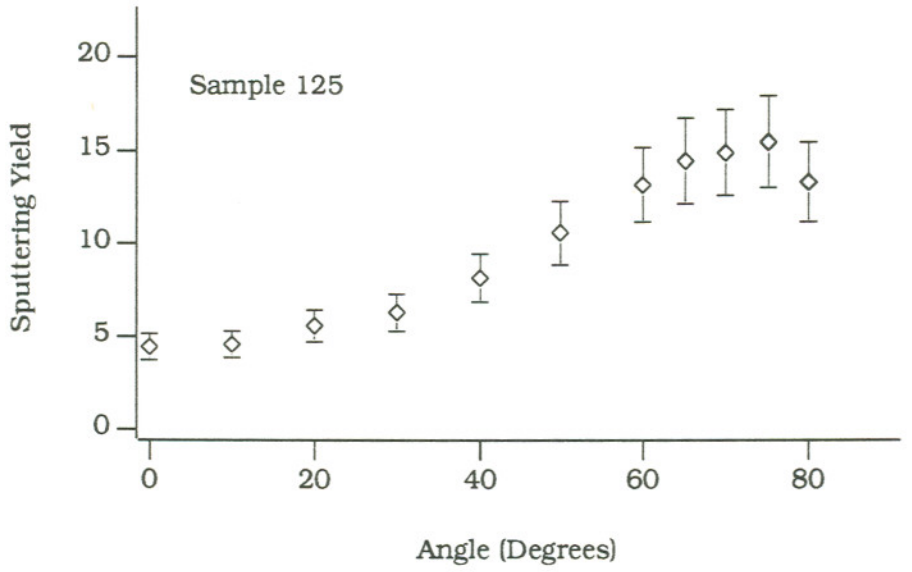

Fig. 3 - 3(a). Plot of the sputter yield as a function of incident angle for 20 keV Ga^+ ions incident on (100) oriented *GaAs*.

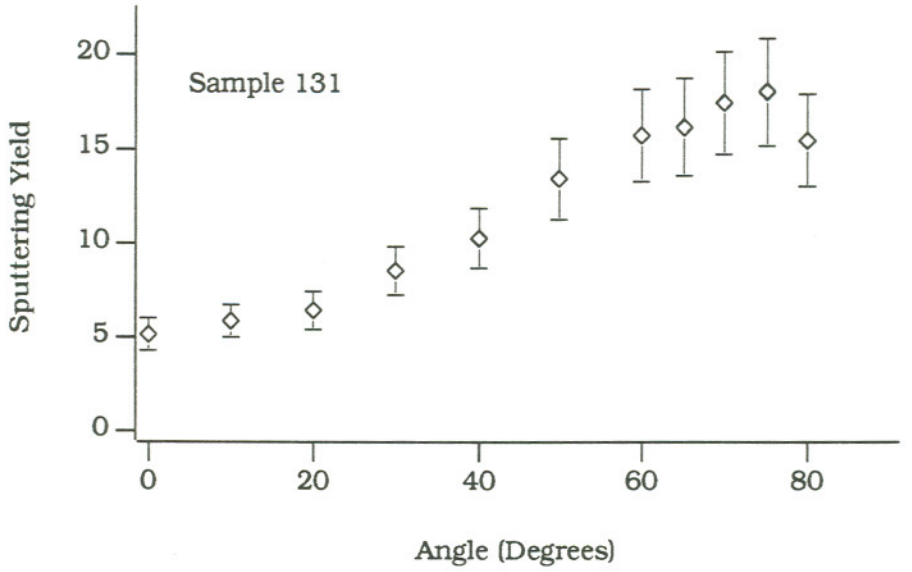

Fig. 3 - 3(b). Plot of the sputter yield as a function of incident angle for 20 keV Ga^+ ions incident on (100) oriented *GaAs*.

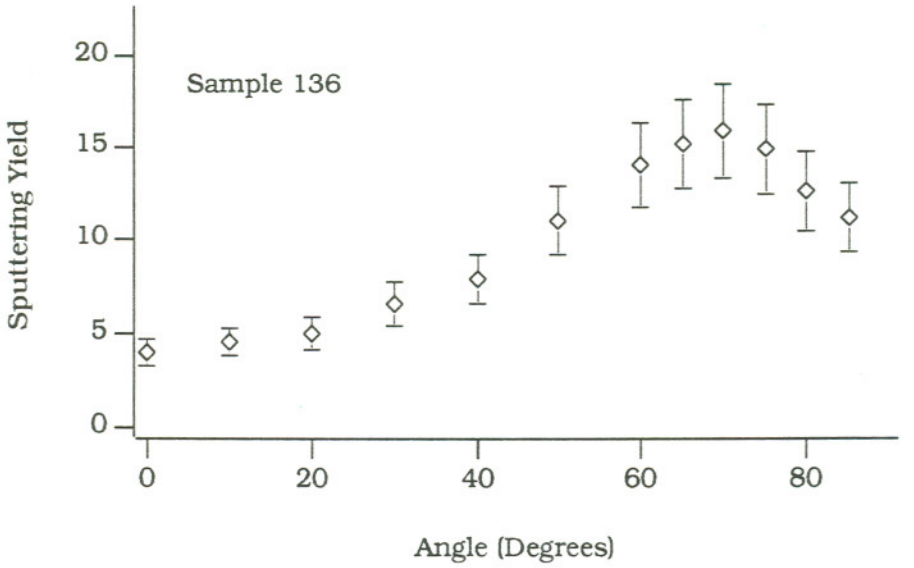

Fig. 3 - 3(c). Plot of the sputter yield as a function of incident angle for 20 keV Ga^+ ions incident on (100) oriented *GaAs*.

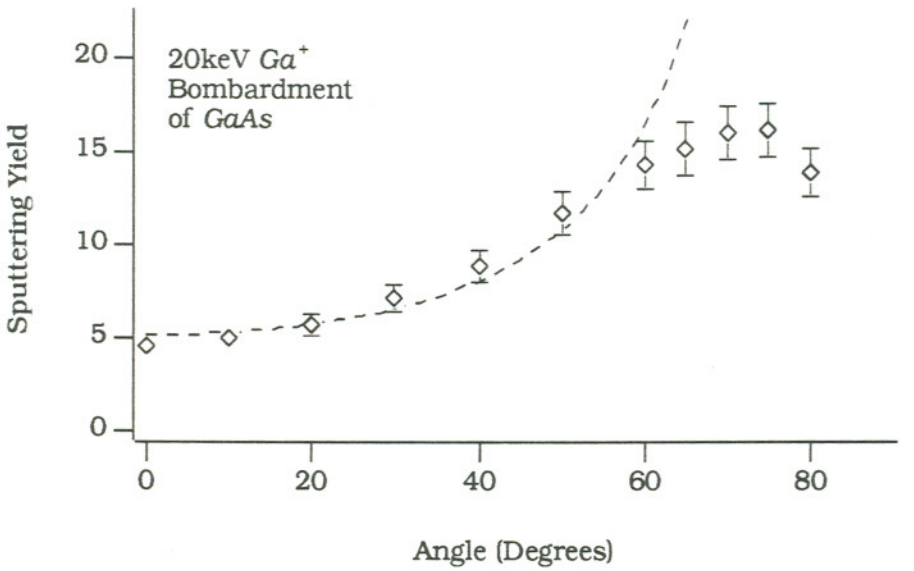

Fig. 3 - 3(d). Average of the results presented in parts (a) through (c). The dashed line represents the angular dependence predicted by the linear cascade theory, which agrees well with the experimental results.

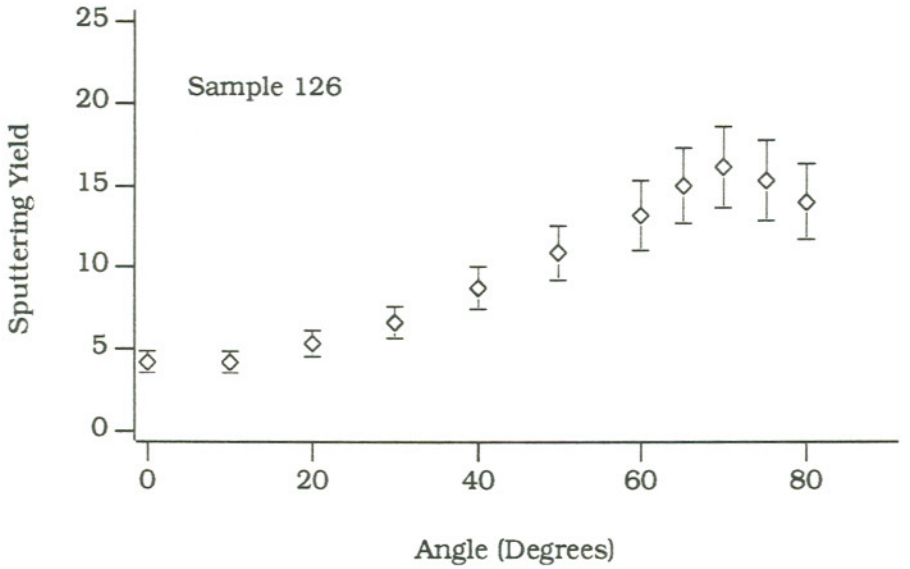

Fig. 3 - 4(a). Plot of the sputter yield as a function of incident angle for 25 keV Ga^+ ions incident on (100) oriented *GaAs*.

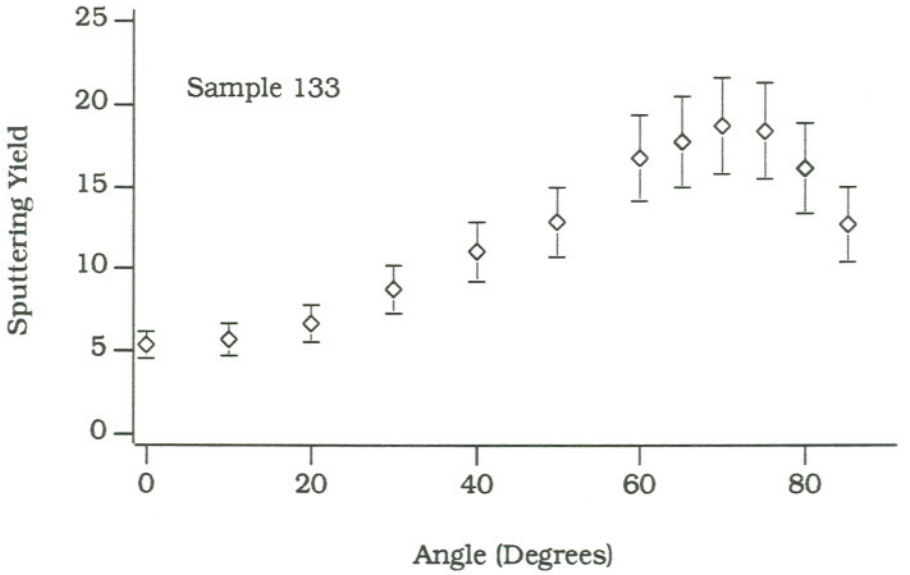

Fig. 3 - 4(b). Plot of the sputter yield as a function of incident angle for 25 keV Ga^+ ions incident on (100) oriented *GaAs*.

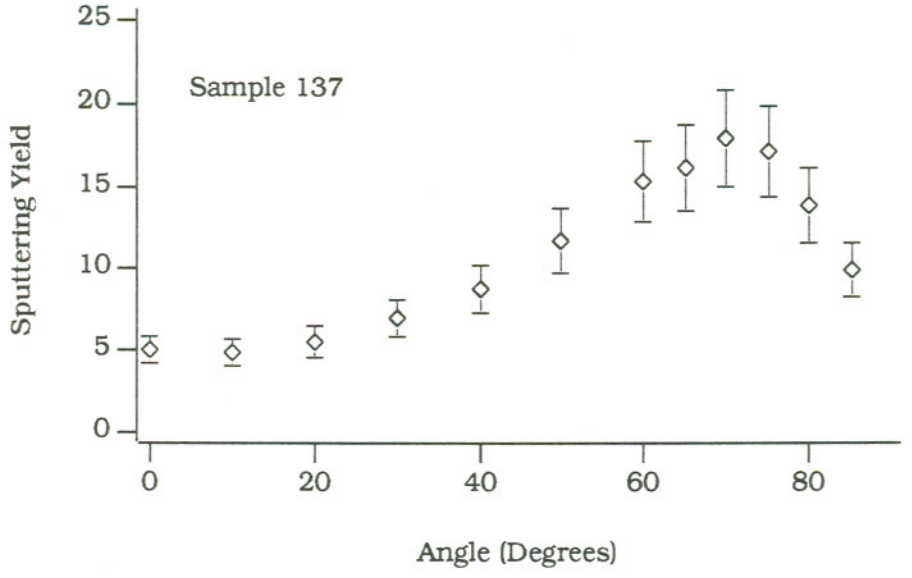

Fig. 3 - 4(c). Plot of the sputter yield as a function of incident angle for 25 keV Ga^+ ions incident on (100) oriented *GaAs*.

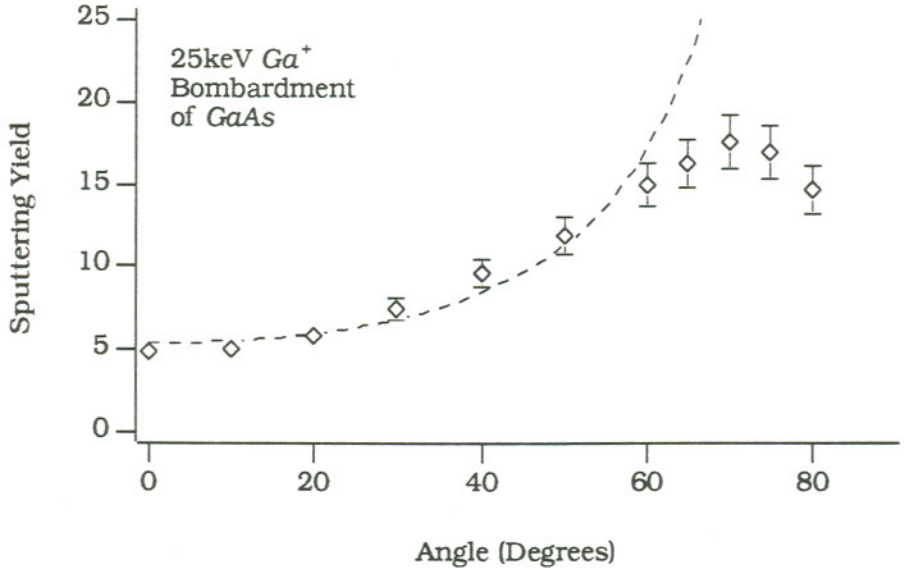

Fig. 3 - 4(d). Average of the results presented in parts (a) through (c). The dashed line represents the angular dependence predicted by the linear cascade theory, which agrees well with the experimental results.

yield include only those points for which there were three values to average.

The characteristic shape of these curves is determined by the energy loss of the ion as it travels through the sample, and the fact that most sputtered particles originate in the top 1 or 2 monolayers of the target[84]. At near normal incidence most of the beam energy is deposited below the surface where it is not likely to contribute to the sputtering process. As the incident angle increases, more energy is deposited near the sample surface where it is available for the production of sputtered particles. This is what accounts for the initial increase in sputtering yield. For very large angles, however, the probability of ion reflection becomes significant, and eventually leads to a decrease in yield.

These two effects combine to give the characteristic shape of the sputtering yield curves. The position of the peak in these curves depends on the mass of the ion relative to the target, the ion energy, and the surface binding energy of the target. Comparing Fig. 3 - 1 through Fig. 3 - 4 shows that over the range of energies studied here, the position of the peak is fairly insensitive to the ion energy, though there may be a slight shift to lower angles as the energy increases.

As noted previously, the angular dependence of the sputtering yield is of the form

$$S(\theta) = S_0(\cos\theta)^{-5/\beta} \qquad 3 - 15$$

A curve of this type was fit to the average yield, and is indicated by a dashed line in part (d) of the figures. Only points with incident angles between 0^0 and 50^0 were included in the fit. The decision on how many points to include was based on a χ^2 goodness of fit test. Including points up to 60^0 increased the χ^2 parameter by about a factor of 3, while only including points up to 40^0 had little effect on the quality of the fit.

The good agreement between the data and the fitted curve is evidence that ion channeling is not an important consideration. If channeling were significant the yield would not be a smooth, monotonically increasing function of the angle of incidence. There would be local minima at angles where channeling had a significant effect. To ensure that the effects of channeling were not being overlooked due to the possible narrow width of the channels, an experiment was performed where the incident angle was varied in 2^0 increments between 0^0 and 16^0. The results of this experiment are plotted in Fig. 3 - 5, and are further evidence that channeling is not an important consideration in the FIBM of *GaAs*.

The absence of channeling should not be surprising. The ion dose used to create a typical sputter crater, about 1×10^{18} ions/cm^2, is well beyond the dose where amorphization of *GaAs* has been seen with much lower energy ion beams. Miyake et al. report that for 1 keV Ga^+

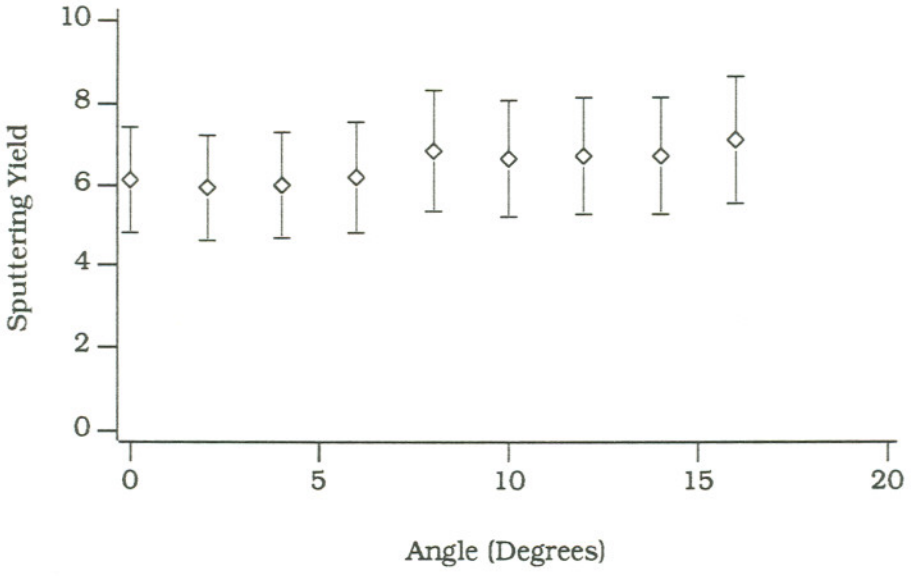

Fig. 3 - 5. Plot of the sputter yield as a function of incident angle for 25 keV Ga^+ ions incident on (100) oriented *GaAs*. For small changes in the incident angle, there is very little change in the sputter yield, indicating that channeling is not important.

bombardment of *GaAs*, a dose of 1×10^{14} ions/cm^2 is required to amorphize the target[103]. Similarly, Williams found that for 3 keV Ar^+ bombardment of *GaAs*, the saturation level for damage was reached at ion doses less than 3×10^{15} ions/cm^2[104]. Given the low ion dose required to amorphize *GaAs*, it seems reasonable to conclude that in the early stages of sputtering an amorphous layer is formed which prevents ion channeling.

Fig. 3 - 6 shows the variation of the sputtering yield with the ion energy. The energy doesn't strongly affect the sputtering yield for the

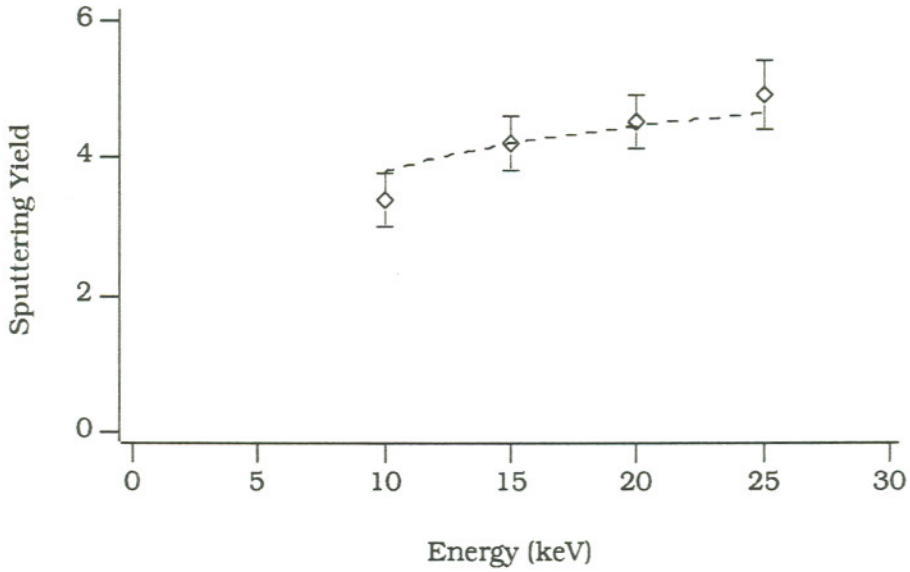

Fig. 3 - 6. Plot of the sputter yield as a function of ion energy for Ga^+ ions incident on (100) oriented $GaAs$. The dashed line represents the energy dependence predicted by the linear cascade theory.

limited range of energies investigated here, but the sputtering yield does appear to increase with increasing energy, as expected.

A curve of the form

$$S(\varepsilon) = S_0 \frac{\ln(1 + \varepsilon)}{(\varepsilon + 0.10718\varepsilon^{0.37544})} \qquad 3 - 16$$

was fit to the data in Fig. 3 - 6 to check that the energy dependence of the sputtering yield agrees with the predictions of the theory. The curve is indicated by the dashed line. The agreement between the fitted curve and the experimental data is good. This, along with the good agreement for the angular dependence of the sputtering yield indicate that it may be possible to apply the linear cascade theory to the current experiment

even though the target material is single crystal and non-elemental, and the ion doses used produce significant changes in the surface composition of the target.

The first step in applying the theory is to calculate the stopping power for the ion/target combination of interest. For a multicomponent target such as *GaAs*, this requires a method for scaling the nuclear stopping power according to the composition of the target. This is usually accomplished in one of two ways. One alternative is to calculate the stopping power for each component of the target and combine the results in a weighted average. A second approach is to calculate an average atomic mass and number, and use these to calculate the stopping power. Because the mass difference between the *Ga* and *As* is minimal, the *GaAs* should closely approximate an elemental target, so the second approach is the one employed below.

A second complication arises from the need to know the surface binding energy of the target. For an elemental target the heat of sublimation is usually used, but for a multicomponent target different components will have different binding energies. Application of the theory requires that they be combined into a single value, presumably by calculating a weighted average. The weighting may be done according to the surface composition or the relative abundances of the various

sputtered species. The latter approach may be more correct, especially if the sputtered flux contains a large molecular component.

Data on surface binding energies for *GaAs* was very difficult to obtain. The only available data appears to be a study by Szymonski and Bhattacharya, who deduced the binding energies for *Ga* and *As* atoms and *GaAs* molecules from the energy spectrum of sputtered particles[105]. According to an earlier work by Szymonski et al., the peak in the energy distribution for a given sputtered species should correspond to half the surface binding energy[106]. For *Ga*, the binding energy was 4.0 eV, for *As* it was 6.0 eV, and for *GaAs* 1.6 eV. An average surface binding energy can be calculated from a weighted average of these values, but there is no good data on their relative abundance. Relative signal amplitudes are given in Ref. [105], but are not corrected for the different detection efficiencies of the different sputtered species.

As a starting point, however, assume the relative abundance is the same as the relative signal intensity. Using the results of Szymonski and Bhattacharya, the average binding energy is then 4.4 eV. Using this value, the sputtering yield as a function of ion energy was calculated, and is plotted, along with the experimentally determined values, in Fig. 3 - 7. The measured yields are about 1.3 times larger than the calculated ones. There are at least three possible sources of error in the calculated values. First is the assumption that the relative signal

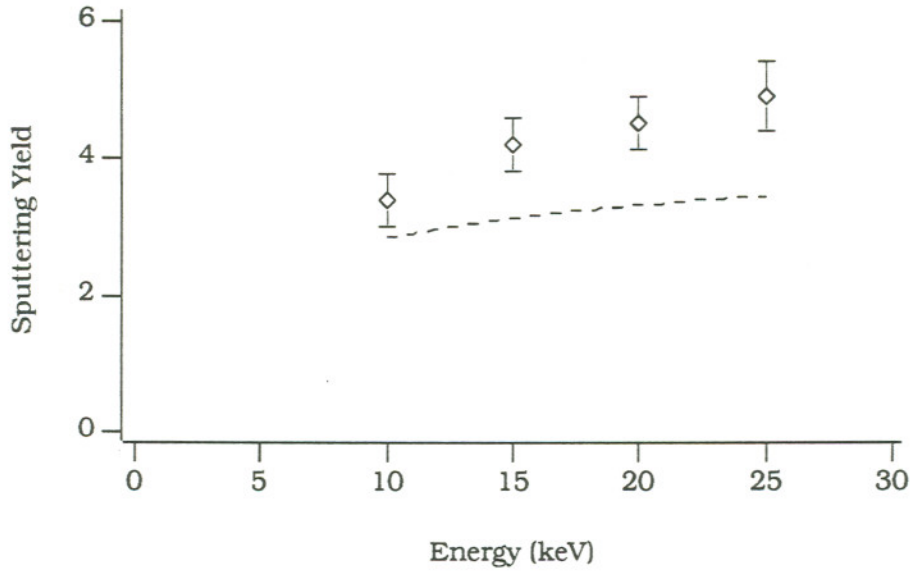

Fig. 3 - 7. Plot of the sputter yield as a function of ion energy for Ga^+ ions incident on (100) oriented *GaAs*. The dashed line represents the sputter yield predicted by the linear cascade theory.

strength is the same as the relative abundance. Second, is the assumption that the relative abundance is independent of the mass and energy of the incident ions. Szymonski and Bhattacharya use 6 keV Ar^+ ions in their work. Third is the chemical differences between the *Ga* and *Ar* bombarded surfaces.

Since the variation of the sputtering yield with energy and angle seems to follow the predictions of the linear cascade theory, and since the surface binding energy is the least well known of the quantities used in the sputtering yield calculation, it seems reasonable to use the binding energy as a fitting parameter to match the experimental results to the theoretical predictions. In Fig. 3 - 6 a curve of the form given in

Eqn. 3 - 16 was fit to the experimental data. The equation of this curve is

$$S(E) = \frac{7.16 \ln\left(1 + 3.6 \times 10^{-3}E\right)}{3.6 \times 10^{-3}E + 0.10718\left(3.6 \times 10^{-3}E\right)^{0.37544}} \qquad 3 - 17$$

where $3.6 \times 10^{-3}E$ is the reduced energy in Eqn. 3 - 10(c). From Eqns. 3 - 9, 3 - 10 and 3 - 17, the surface binding energy is determined to be 3.2 eV. This value can be checked against the yield measurements of the next section for *Au* bombardment of *GaAs*.

B. $Au^{+,++}$ *Bombardment of (100) Oriented* GaAs.

A *Au* LMIS was also used to sputter several *GaAs* samples. The limited lifetime of the *Au* source and the time required to replace the source made it very time consuming to collect data, so less data was collected for *Au* than for *Ga*. Four different samples were machined, two in which the angle of incidence was varied while the accelerating voltage was kept fixed at 20 kV, and two with the beam held at normal incidence while the accelerating voltage was varied between 10 and 25 kV. The results are shown in Fig. 3 - 8 and Fig. 3 - 9.

Fig. 3 - 8 shows the angular dependence of the sputtering yield. As was the case for *Ga* bombardment of *GaAs*, the yield increases smoothly with increasing angle, so channeling is probably not significant. The position of the peak is similar to the position seen with *Ga*. Once again a

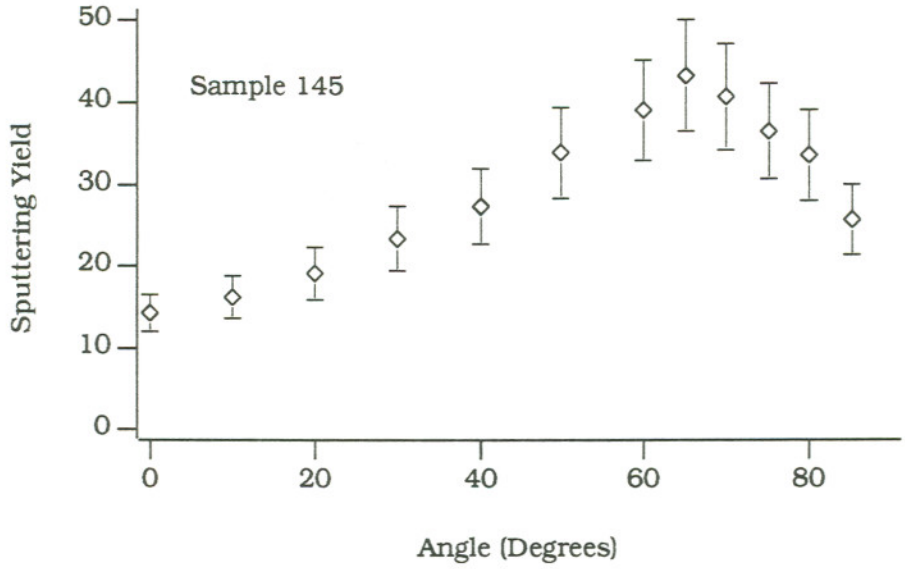

Fig. 3 - 8(a). Plot of the sputter yield as a function of incident angle for 20 kV $Au^{+,++}$ ions incident on (100) oriented *GaAs*.

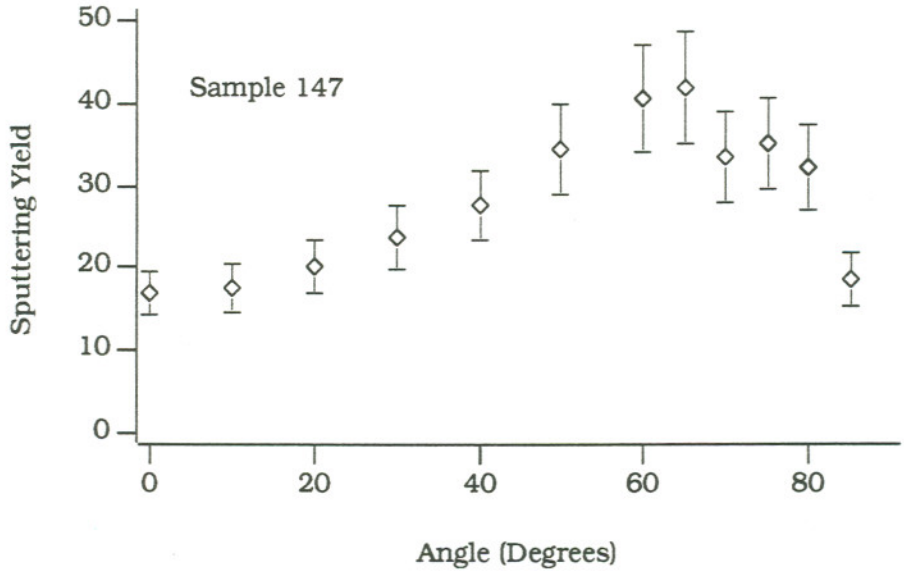

Fig. 3 - 8(b). Plot of the sputter yield as a function of incident angle for 20 kV $Au^{+,++}$ ions incident on (100) oriented *GaAs*.

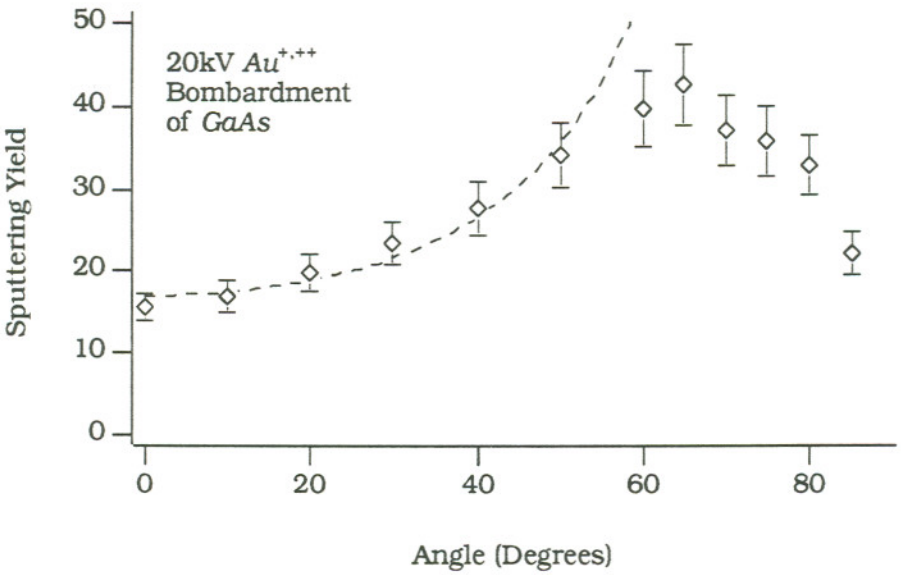

Fig. 3 - 8(c).. Average of the results presented in parts (a) and (b). The dashed line represents the angular dependence predicted by the linear cascade theory, which agrees well with the experimental results.

curve of the form shown in Eqn. 3 - 15 was fitted to the average yield, and is indicated by the dashed line in Fig. 3 - 8(c). As was the case for *Ga* bombardment, the fit is quite good.

The variation of the sputtering yield with the accelerating voltage is shown in Fig. 3 - 9. This is not the same as the energy dependence of the sputtering yield because of the composition of the beam, which contains both Au^{+} and Au^{++} ions. The dashed line in Fig. 3 - 9 is a least squares fit of a linear combination of two terms of the form shown in Eqn. 3 - 16, one term for each ion energy, weighted according to the relative abundance of the different energy ions. There is good agreement between the fitted curve and the experimental data.

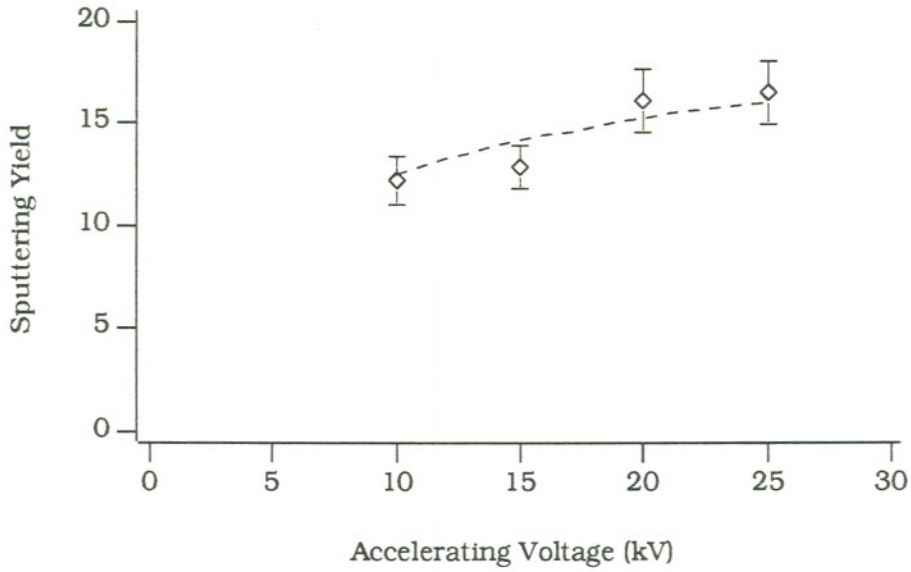

Fig. 3 - 9. Plot of the sputter yield as a function of accelerating voltage for $Au^{+,++}$ ions incident on (100) oriented *GaAs*. The dashed line represents the energy dependence predicted by the linear cascade theory.

As was the case for *Ga* bombardment of *GaAs*, the angular and energy dependence of the sputtering yield agree well with the predictions of the linear cascade theory. The main difference between the two sets of data is the much larger sputtering yield seen for *Au*. This has an interesting consequence in terms of altered layer formation. A paper by Ho shows how the sputtering yield influences the composition of the altered layer[85]. An increase in the sputtering yield results in a shorter time constant for equilibration of the altered layer composition, and a reduced thickness for the layer. The reduced layer thickness, and the fact that *Ga* is not being implanted into the target, means there is less excess *Ga* on

the *Au* bombarded surface than on the *Ga* bombarded surface, which should result in less droplet formation. In fact no droplet formation was noted for *Au* bombardment of *GaAs* under any bombardment conditions.

This, along with the increased yield, makes the *Au* LMIS of interest for fabricating opto-electronic devices, where large amounts of material must be removed and the machined surfaces must be of optical quality. Unfortunately, as seen in Fig. 1 - 3, there are difficulties caused by the composition of the beam which overshadow the benefits, unless efforts are made to eliminate any ambient magnetic fields, or one component of the beam is filtered out.

Fig. 3 - 10 compares the experimentally measured yield to the predictions of the linear cascade theory. The total calculated yield is the weighted average of the yields for the singly and doubly charged ions. The combined yield was at most about 6% larger than the yield for the singly charged ions alone, so even though the doubly charged ions make up about 25% of the beam, their effect on the total sputtering yield is much smaller. This is because the yield increases rather slowly with ion energy.

The calculated yields are based on a surface binding energy of 3.2 eV, as determined from the least squares fit in Fig. 3 - 6. The measured values are about 1.5 times the predicted values. Once again, the most likely source for this discrepancy is the surface binding energy. As noted

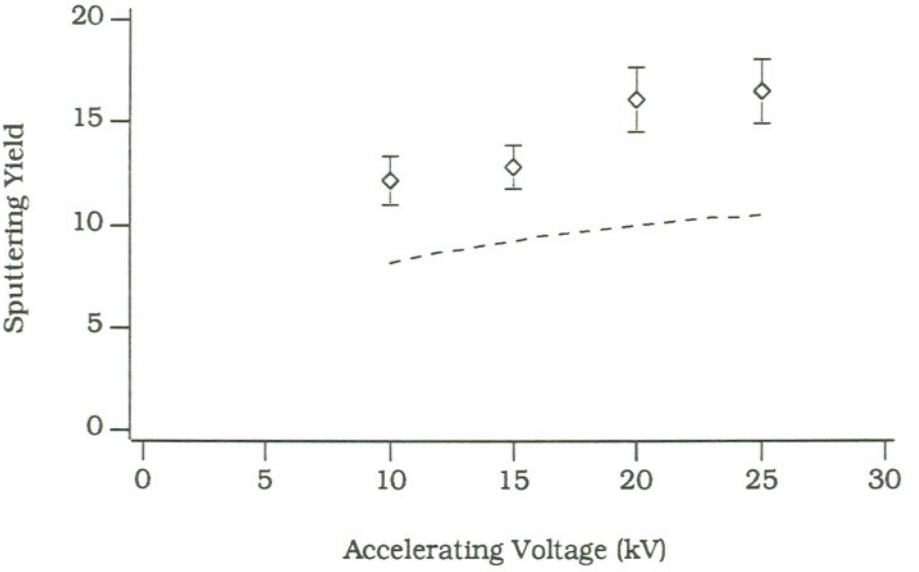

Fig. 3 - 10. Plot of the sputter yield as a function of ion energy for $Au^{+,++}$ ions incident on (100) oriented *GaAs*. The dashed line represents the sputter yield predicted by the linear cascade theory.

above, no droplet formation was observed under any bombardment conditions for *Au* bombardment of *GaAs*, so the composition of the *Au* bombarded surface was obviously quite different from that of the *Ga*.

A new surface binding energy of 2.15 eV was calculated from the least squares fit in Fig. 3 - 9. This is very close to the 2.3 eV obtained in a similar way by Szymonski and Bhattacharya for 6 keV *Ar* bombardment of *GaAs*[105]. It is interesting to note that they do not report any evidence of droplet formation in their work. Apparently, the Ga^+ ion implantation affects the surface binding energy differently than the $Au^{+,++}$ and Ar^+ implantation.

C. Ga^+ *Bombardment of (100) Oriented* Si.

As was done for *GaAs*, the sputtering yield for (100) oriented *Si* was measured as a function of the ion energy and angle of incidence. The *Si* experiments were actually conducted prior to the experiments with *GaAs*, but because of difficulties encountered in collecting the *Si* data the results are less complete. Three factors contributed to the difficulty. First, *Si* is much harder to cleave than *GaAs*, making it more difficult to section through the sputter craters. The data presented here represents only a fraction of the total number of samples machined. A large number of samples were ruined when the cleave failed to section the sputter craters. Second, data collection was more time consuming because of the the lower sputtering yield for *Si*, which increased machining time. Finally, the *Si* experiments were conducted prior to modifications to the system which increased the range of angles available for sputtering experiments. This limited the range of angles to 0^0 - 60^0 rather than the 0^0 - 85^0 possible for *GaAs*.

Fig. 3 - 11 through Fig. 3 - 14 show the variation of the sputtering yield with incident angle for ion energies of 10, 15, 20, and 25 keV. Two samples were machined at each energy and the results plotted in parts (a) and (b) of the figures. The average of the two samples is plotted in part (c). Again, the angular dependence of the yield is compared to theory by a least squares fit of Eqn. 3 - 15 to the average yield. The resulting

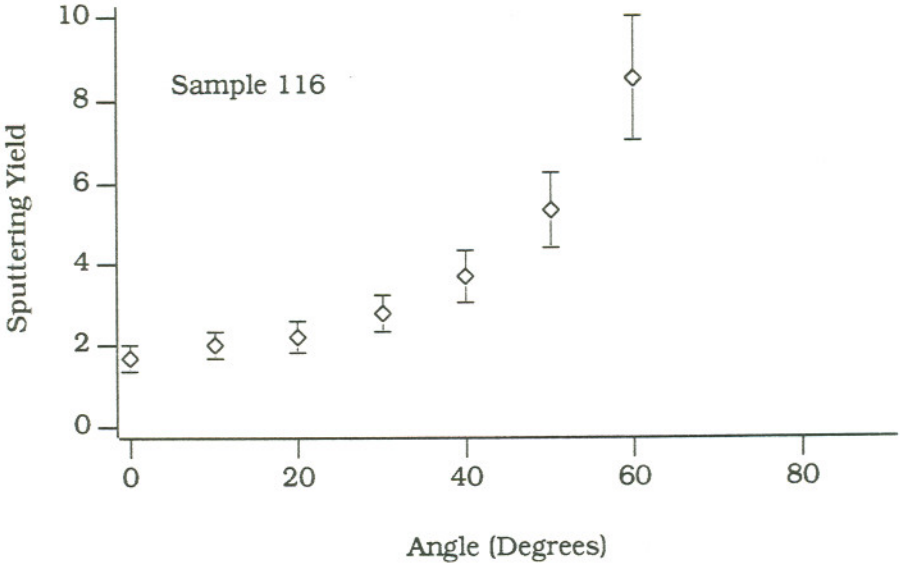

Fig. 3 - 11(a). Plot of the sputter yield as a function of incident angle for 10 keV Ga^+ ions incident on (100) oriented *Si*.

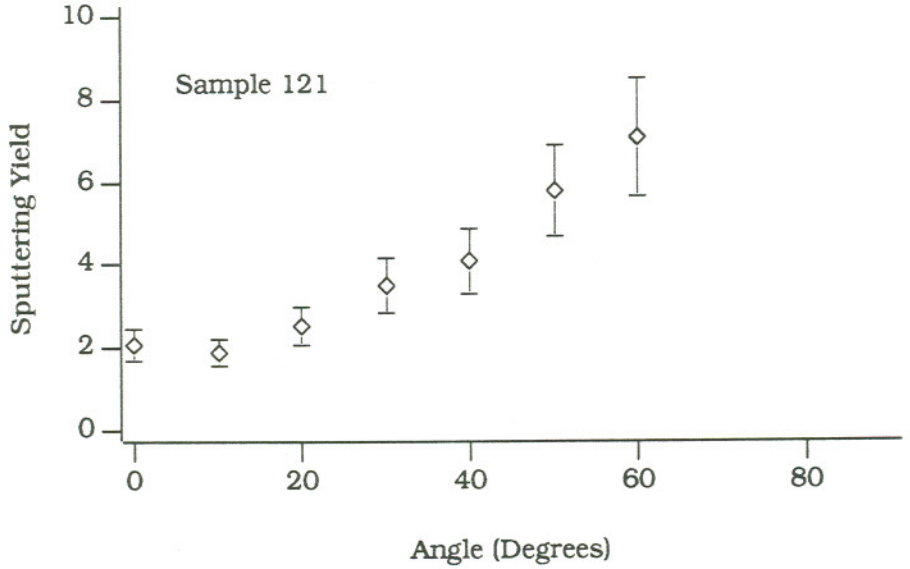

Fig. 3 - 11(b). Plot of the sputter yield as a function of incident angle for 10 keV Ga^+ ions incident on (100) oriented *Si*.

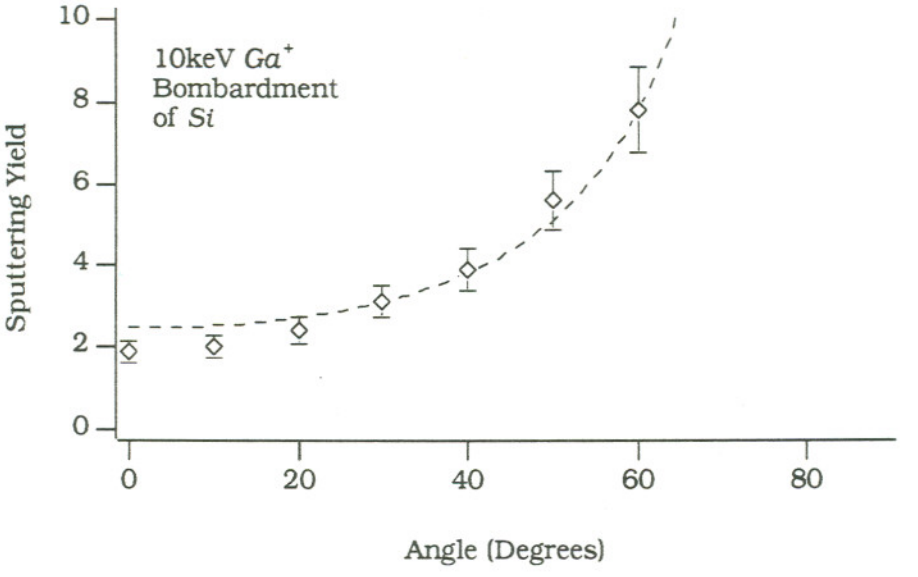

Fig. 3 - 11(c). Average of the results presented in parts (a) and (b). The dashed line represents the angular dependence predicted by the linear cascade theory, which agrees well with the experimental results.

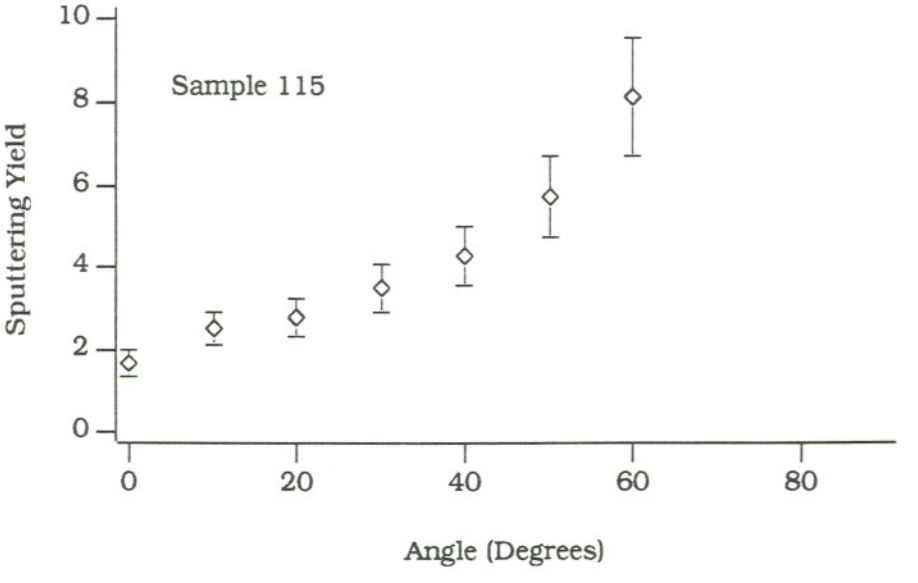

Fig. 3 - 12(a). Plot of the sputter yield as a function of incident angle for 15 keV Ga^+ ions incident on (100) oriented *Si*.

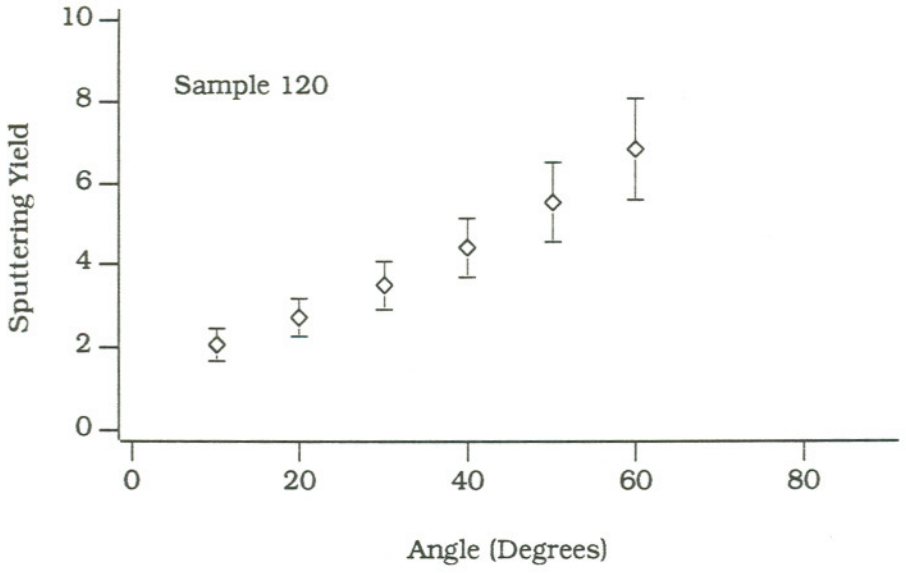

Fig. 3 - 12(b). Plot of the sputter yield as a function of incident angle for 15 keV Ga^+ ions incident on (100) oriented *Si*.

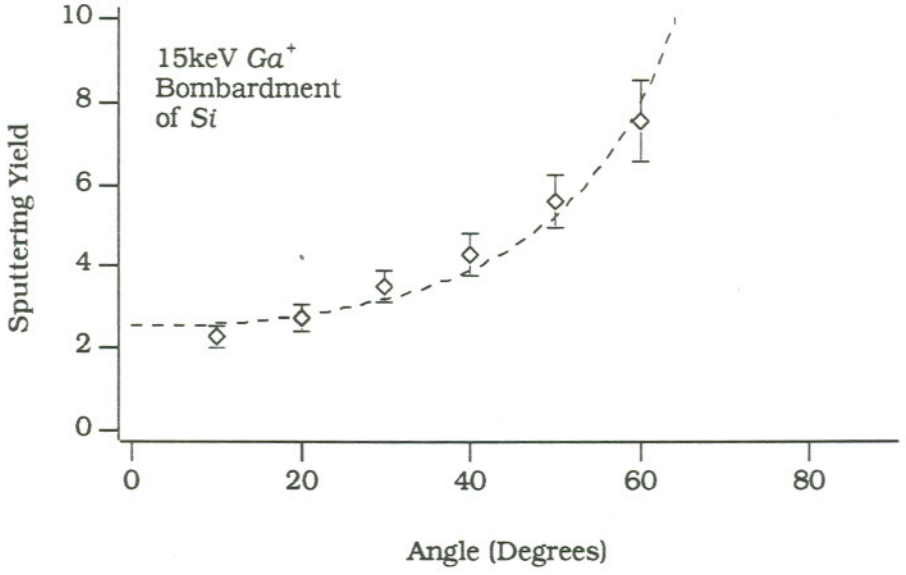

Fig. 3 - 12(c). Average of the results presented in parts (a) and (b). The dashed line represents the angular dependence predicted by the linear cascade theory, which agrees well with the experimental results.

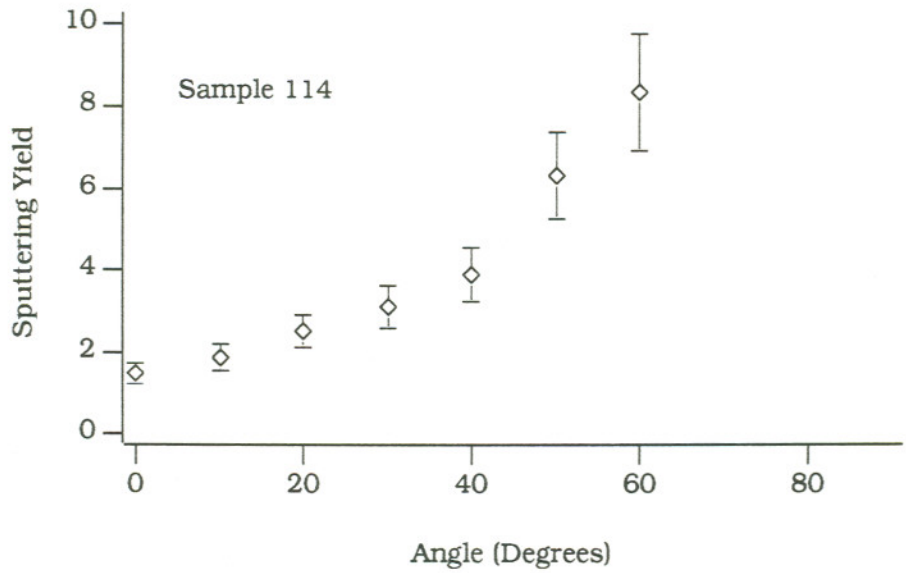

Fig. 3 - 13(a). Plot of the sputter yield as a function of incident angle for 20 keV Ga^+ ions incident on (100) oriented *Si*.

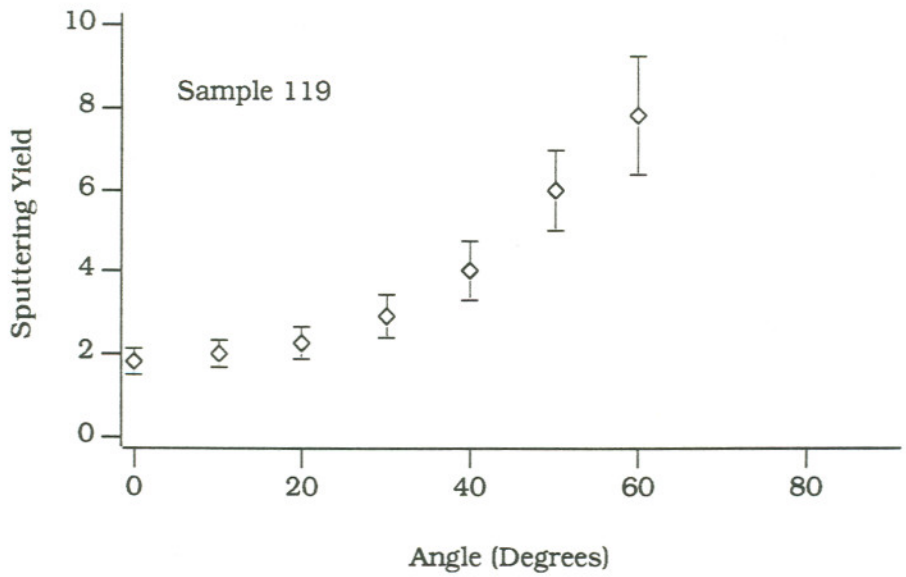

Fig. 3 - 13(b). Plot of the sputter yield as a function of incident angle for 20 keV Ga^+ ions incident on (100) oriented *Si*.

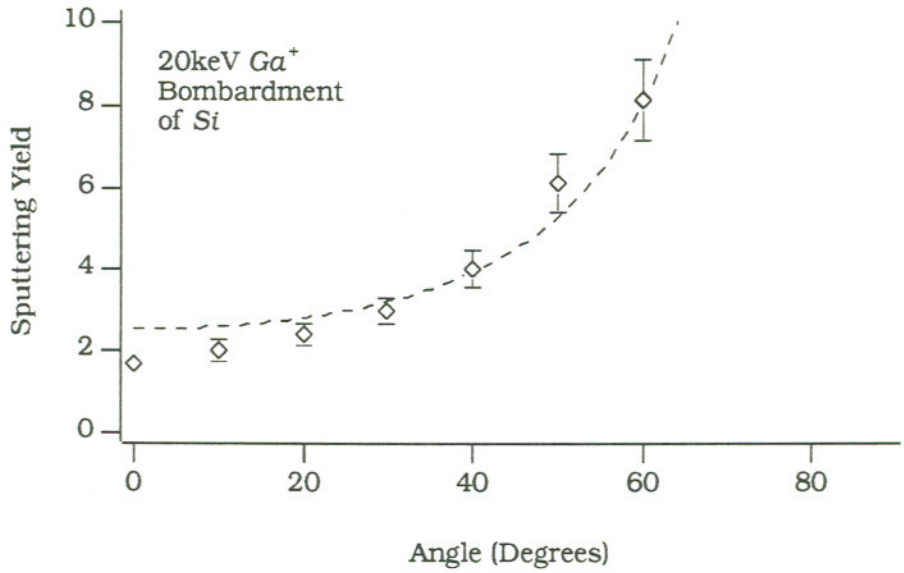

Fig. 3 - 13(c). Average of the results presented in parts (a) and (b). The dashed line represents the angular dependence predicted by the linear cascade theory, which agrees well with the experimental results.

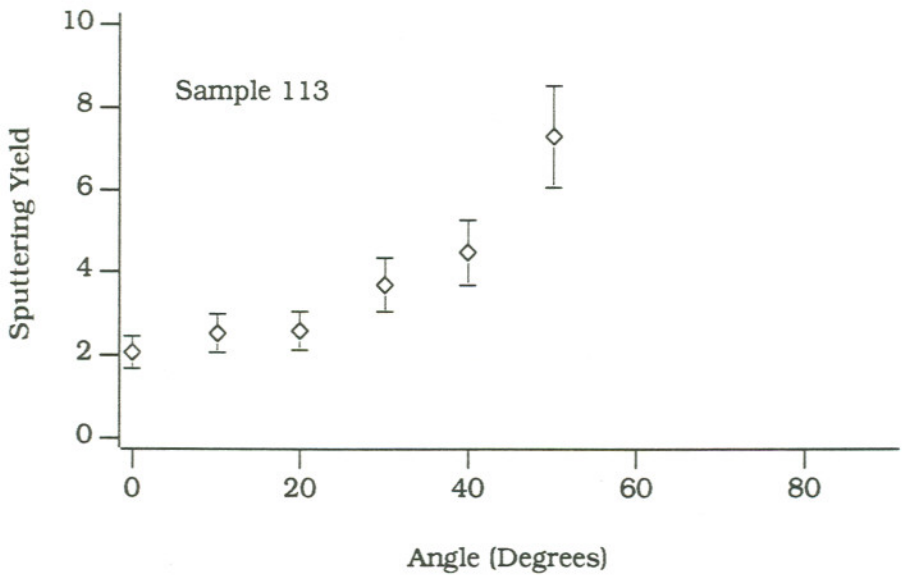

Fig. 3 - 14(a). Plot of the sputter yield as a function of incident angle for 25 keV Ga^+ ions incident on (100) oriented *Si*.

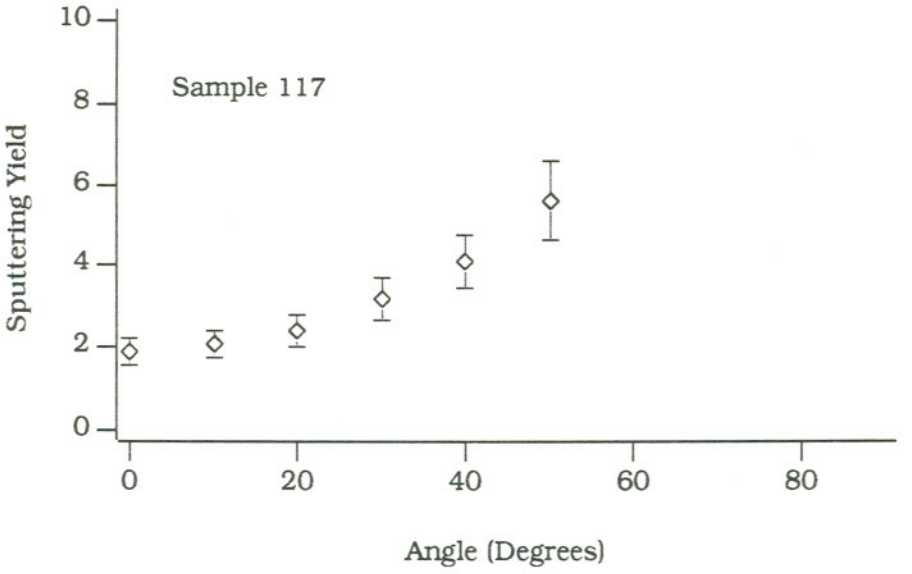

Fig. 3 - 14(b). Plot of the sputter yield as a function of incident angle for 25 keV Ga^+ ions incident on (100) oriented *Si*.

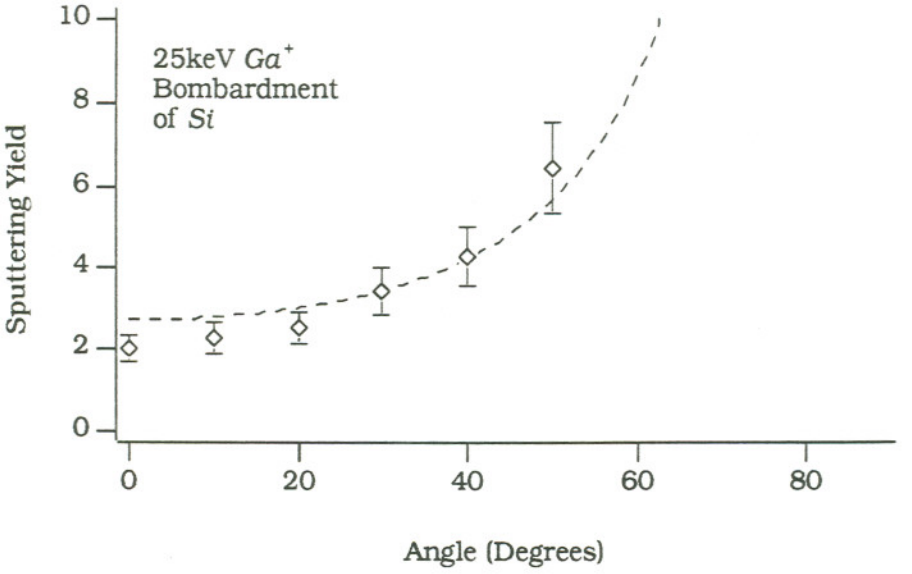

Fig. 3 - 14(c). Average of the results presented in parts (a) and (b). The dashed line represents the angular dependence predicted by the linear cascade theory, which agrees well with the experimental results.

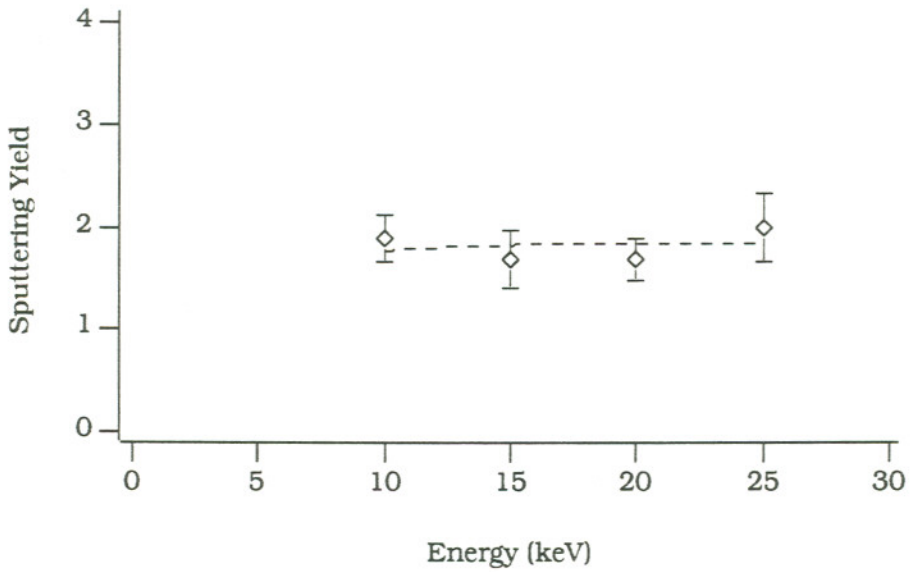

Fig. 3 - 15. Plot of the sputter yield as a function of ion energy for Ga^+ ions incident on (100) oriented *Si*. The dashed line represents the energy dependence predicted by the linear cascade theory.

curve is indicated by the dashed line in part (c). For angles greater than about 20^0, the angular dependence of the yield agrees well with Eqn. 3 - 15, but at smaller angles the yield drops off more rapidly than predicted. The difference is small, but may indicate that channeling is occurring.

Fig. 3 - 15 shows the variation of the sputter yield with ion energy. The shape of this curve differs somewhat from that of *GaAs*. For *Si*, the yield is almost independent of energy. The dashed line is a least squares fit of Eqn. 3 - 16, which shows that the energy dependence closely follows that predicted by the linear cascade theory. The results agree well with those of Ishitani et al., who report a sputtering yield of 1.7 for

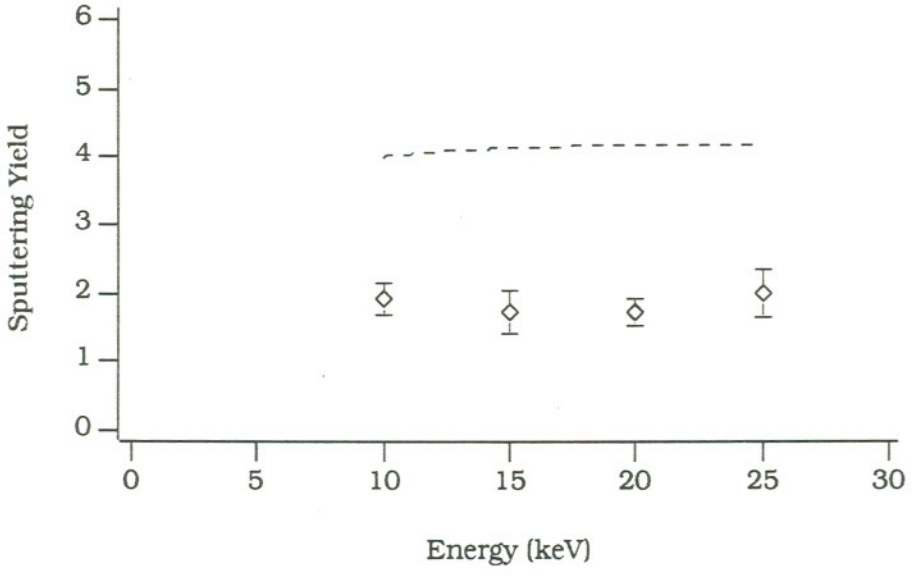

Fig. 3 - 16. The yield as a function of ion energy for Ga^+ ions incident on (100) oriented *Si*. The dashed line represents the sputter yield predicted by the linear cascade theory.

10 keV Ga^+ bombardment of *Si*, and Ochiai et al. who report a sputtering yield of 1.8 for 35 keV Ga^+ bombardment[107,108].

The sputtering yield as a function of ion energy was calculated from Eqn. 3 - 14, and the results are plotted, along with the experimentally measured yield, in Fig. 3 - 16. Unlike *GaAs*, where the theory consistently underestimated the yield, for *Si* the calculated values overestimate the yield by more than a factor of 2. Again, this is consistent with the idea that channeling may be important.

D. Ga^+ *Bombardment of (111) Oriented* Si.

To see if channeling is influencing the sputter yield, several craters were machined in (111) *Si*. A dramatic difference in the measured yields would indicate that channeling is significant because of the different channeling probabilities for the two different crystal orientations. Again, difficulties were encountered in cleaving the samples, but with an added complication peculiar to the (111) crystal orientation.

Si cleaves along the [110] family of planes, which intersect the surface of the (111) oriented crystal to form an equilateral triangle. This means that samples cleaved from the (111) oriented crystal are not rectangular, as is the case for the (100) oriented crystal where the [110] planes meet at right angles. The 60^0 angle between planes means there is a significant probability that the sample will cleave along a direction which is 60^0 from the direction along which the sputter craters are machined. Even though many samples were machined, a large number of them cleaved along the wrong direction. Of those that cleaved along the right direction, a significant fraction did not cleave through the craters.

Even with these difficulties, enough data was collected to allow a comparison with the results for (100) *Si*. The sputter yield was measured at normal incidence for 15, 20 and 25 keV Ga^+ bombardment, and as a function of incident angle for 25 keV ions, but only for angles up to 40^0.

Many more samples were machined in an effort to collect similar data at other energies and over a wider range of angles, but without success.

Fig. 3 - 17 plots the yield as a function of incident angle for 25 keV Ga^+ ions. Part (c) of the figure is the average of parts (a) and (b). The least squares fit of Eqn. 3 - 15, shown as the dashed line in part (c), is again fairly good, but as for (100) *Si* falls off more rapidly than predicted. Again, the difference is fairly small. Fig. 3 - 18 shows the dependence of the sputter yield on ion energy. The dashed line is again a least squares fit of Eqn. 3 - 16, showing that the energy dependence of the yield agrees well with theory. Comparison of the experimental values in Fig. 3 - 18 with the theoretically predicted values of Fig. 3 - 16 shows that the predicted yield is again much larger than the measured value.

This is all consistent with the idea that channeling is influencing the sputtering yield, but Table 3 - 1 shows that within experimental error the yield is the same for the two crystal orientations. This strongly suggests that channeling is not important. This is further supported by the ion dose required to amorphize *Si*. Williams found that for 3 keV Ar^+ bombardment of *Si*, the saturation level for damage was reached at ion doses less than 3×10^{15} ions/cm^2[104]. For 4 keV Ga^+ implantation into (100) oriented *Si*, Lu et al. found that an ion dose of 3.4×10^{15} ions/cm^2 was sufficient to amorphize the target[109]. Finally, Hart et al. found that for 59 keV Ga^+ bombardment of *Si*, the dose required to amorphize the

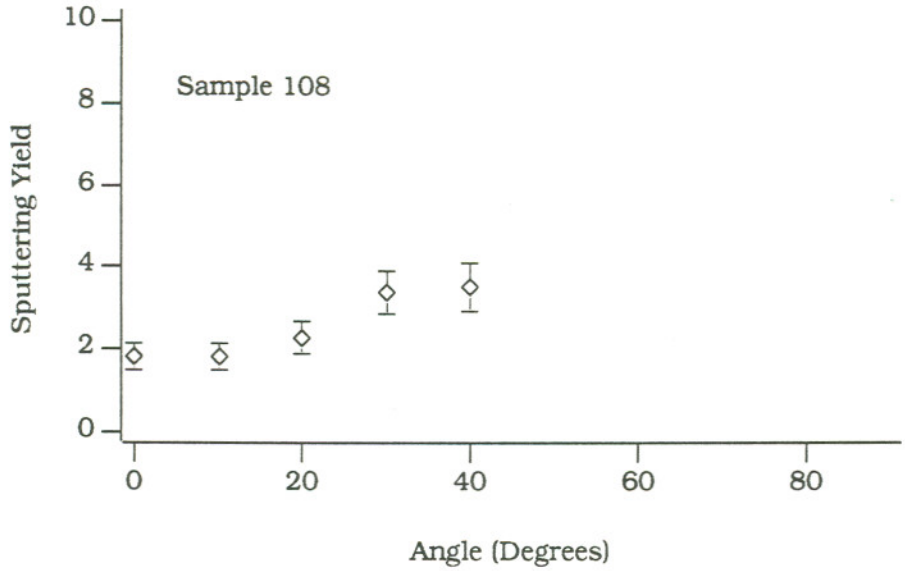

Fig. 3 - 17(a). Plot of the sputter yield as a function of incident angle for 25 keV Ga^+ ions incident on (111) oriented *Si*.

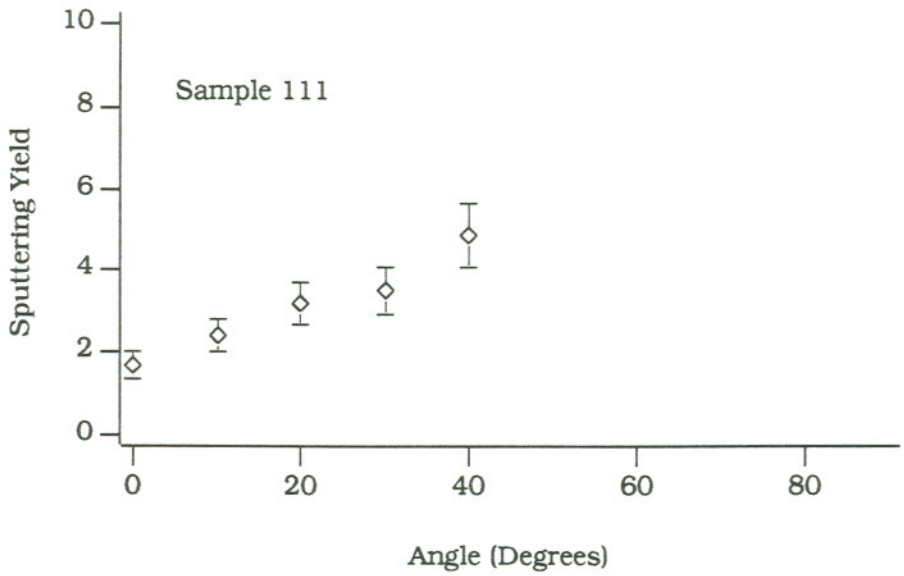

Fig. 3 - 17(b). Plot of the sputter yield as a function of incident angle for 25 keV Ga^+ ions incident on (111) oriented *Si*.

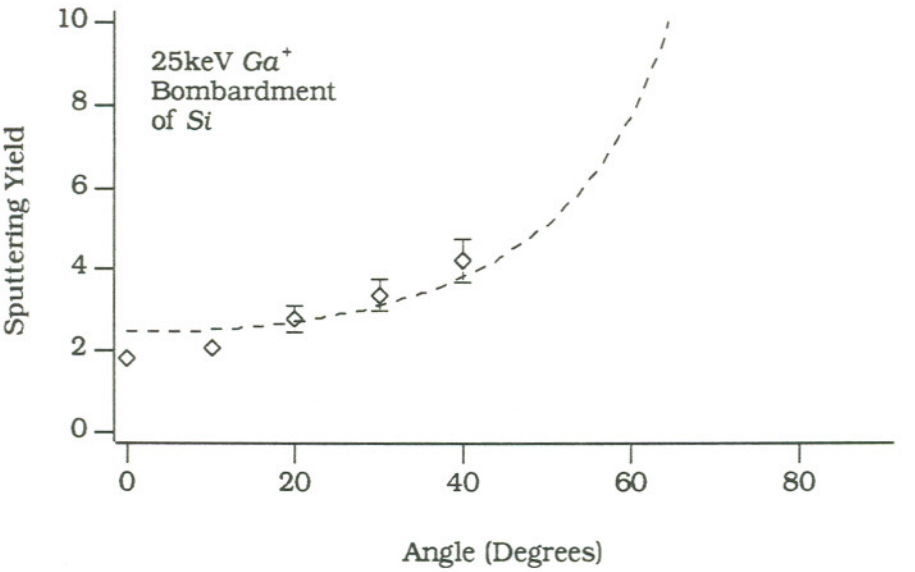

Fig. 3 - 17(c). Plot of the sputter yield as a function of incident angle for 25 keV Ga^+ ions incident on (111) oriented *Si*. The dashed line represents the angular dependence predicted by the linear cascade theory.

surface is on the order of 10^{14} ions/cm^2[110]. All of these are much less than the dose of ~ 1×10^{18} ions/cm^2 used to create a typical sputter crater, indicating that the bombarded surface is amorphized in the very early stages of sputtering.

Given the good agreement between the experimentally measured energy dependence of the sputtering yield and the predictions of the linear cascade theory, the fair agreement with the angular dependence predicted by the theory, at least for angles greater than about 20^0, and the good agreement between the measured yields for the two different crystal orientations, it is once again concluded that altered layer

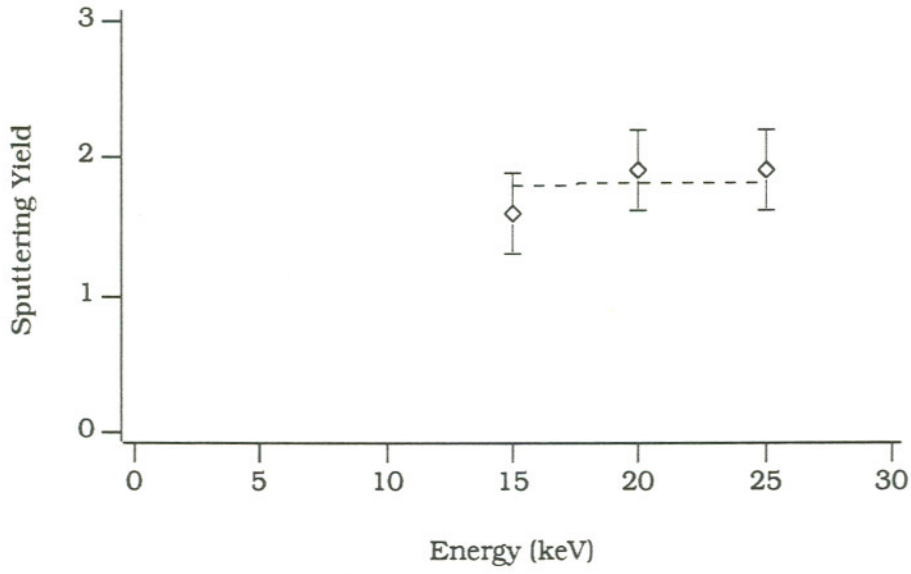

Fig. 3 - 18. Plot of the sputter yield as a function of ion energy for Ga^+ ions incident on (111) oriented *Si*. The dashed line represents the energy dependence predicted by the linear cascade theory.

formation is responsible for the difference between the measured and calculated yields. Using the fitted curve in Fig. 3 - 15 to calculate a surface binding energy results in a value of 10.3 eV, about 2.3 times the binding energy calculated from the heat of sublimation. This value for the binding energy gives good agreement between the measured and calculated yields for both crystal orientations.

E. Summary.

A series of experiments was conducted to determine the dependence of the sputtering yield on ion energy and angle of incidence under bombardment conditions typical of FIBM. The results were then

	(100) Si		(111) Si	
Energy (keV)	Average Yield	±	Average Yield	±
10	1.9	0.2	—	—
15	1.7	0.3	1.6	0.3
20	1.7	0.2	1.9	0.3
25	2.1	0.2	1.9	0.3

Table 3 - 1. Comparison of the sputtering yield for Ga^+ bombardment of two different crystal orientations of *Si*. Within the limits of experimental accuracy, there is no difference in the measured yield.

compared to the predictions of the linear cascade theory. In general, the dependence of the sputtering yield on these two parameters was consistent with the linear cascade theory of sputtering, although at near normal incidence the sputtering yield for *Ga* bombardment of *Si* seems to drop off more rapidly than predicted by the theory. It seems unlikely that this discrepancy is caused by ion channeling, as there is no measurable difference in yield for the two different crystal orientations tested.

Additionally, the theory was not able to accurately predict the magnitude of the yield. This discrepancy is most likely due to uncertainty in the surface binding energy. This uncertainty is twofold. First, in the case of *GaAs* there is no reliable data for the surface binding energy. Second, for both *GaAs* and *Si*, changes in surface layer composition caused by altered layer formation mean the surface binding energy changes depending on the bombardment conditions. This makes it extremely difficult to apply the linear cascade theory to FIBM.

4. Vector Scanning

Having investigated the sputtering yield for creation of simple rectangular sputter craters, it is interesting to try to apply the results to the fabrication of more complex structures. Generally, such structures are fabricated by scanning a series of overlapping rectangular sputter craters. The variation of ion dose with position depends on the overlap[23,24]. However, it has been suggested that a more efficient method of varying the ion dose is to employ the vector scanning techniques commonly used in lithography[23,25,111]. Preliminary results using this technique have been published, but until now a three dimensional model of how to apply vector scanning to FIBM has been lacking[28,29,78]. Such a model is presented here, along with several interesting applications which are analyzed based on the results of the previous chapter.

I. The Model.

In general the depth, z, of a sputter crater, at any point x,y on the target surface, is related to the ion dose by

$$z(x,y) = \frac{D(x,y)\,S(x,y)}{N} \qquad 4 - 1$$

where $D(x,y)$ is the ion dose, $S(x,y)$ is the sputtering yield, and N is the atomic density of the target. The effects of redeposition of sputtered material have been ignored. Note that the variation in the sputtering yield with position, assuming a homogeneous target, is due to the local surface topography which determines the angle of incidence of the ion beam, and hence the sputtering yield.

Assuming that the beam current is uniformly distributed across the diameter of the beam, the ion dose is related to the beam current by

$$D(x,y) = \frac{I_{Beam}\,6.25 \times 10^{18} t_d}{\pi \left(\frac{d}{2}\right)^2} \qquad 4 - 2$$

where d is the beam diameter, and t_d the dwell time at the point x,y. Expressing the dwell time in terms of the scan velocity

$$t_d = \frac{d}{|v(x,y)|} \qquad 4 - 3$$

gives an expression for the ion dose in terms of the scan velocity of the beam

$$D(x,y) = \frac{4}{\pi} 6.25 \times 10^{18} I_{Beam} \frac{1}{d\,|v(x,y)|} \qquad 4 - 4$$

This equation can be substituted back into Eqn. 4 - 1 to give the crater depth as a function of position

$$z(x,y) = \frac{4}{\pi} 6.25 \times 10^{18} I_{Beam}\, S(x,y)\, \frac{1}{Nd\,|v(x,y)|} \qquad 4 - 5$$

If known expressions for $z(x,y)$ and $S(x,y)$ are substituted into Eqn. 4 - 5, and the beam scan velocity is expressed in terms of the time derivatives $\dot{x}$ and $\dot{y}$, the above becomes a differential equation for the beam position as a function of time.

$$z(x,y) = \frac{4}{\pi} 6.25 \times 10^{18} I_{Beam}\, S(x,y)\, \frac{1}{Nd\,\sqrt{\dot{x}^2 + \dot{y}^2}} \qquad 4 - 6$$

In principle, the solution to Eqn. 4 - 6 can be used to control the ion beam and create the desired contour. This is fairly simple if the initial surface is flat so that the sputtering yield is independent of x and y. For this case, Eqn. 4 - 6 reduces to

$$z(x,y) = \frac{c}{\sqrt{\dot{x}^2 + \dot{y}^2}} \qquad 4 - 7$$

where c is a constant.

In practice, things are more complicated. Recall that in deriving Eqn. 4 - 6 the effects of redeposition were ignored. This can only be done for large scan velocities, which means small ion doses and shallow sputter craters. To create deeper contours and still avoid redeposition, large scan velocities and repeated scans must be used. For contours machined using this technique $S(x,y)$ is no longer a constant. It depends on the surface created by previous repetitions of the scan. Eqn. 4 - 6 must be solved rather than the simpler Eqn. 4 - 7. Additionally, a new solution must be found for each repetition of the scan. Depending on the complexity of $S(x,y)$, this may or may not be possible. It may be possible to simplify the process by choosing simple forms for the intermediate contours, e.g., approximate the desired contour by a series of step functions, but in general application of Eqn. 4 - 6 is quite difficult.

II. Examples.

A. Planar Slanted Surface, Part I.

As an example of how to apply Eqn. 4 - 6, consider the contour

$$z(x,y) = ax \qquad 4 - 8$$

which describes a planar surface with slope a in the x direction. There are three reasons for considering this example. First, this shape is of practical interest for fabricating surface emitting diode lasers[23,24,25]. Second, Eqn. 4 - 6 is easy to solve for this contour and the results are easily analyzed, even for deep contours created by multiple scans. Finally, experimental results obtained in producing this contour suggest that Eqn. 4 - 6 reduces to Eqn. 4 - 7 *even for complex contours created with multiple scans.* If this is in fact the case, it greatly simplifies the application of vector scanning to the creation of an arbitrary surface contour.

The contour required for the fabrication of a surface emitting diode laser is several microns wide and several microns deep with a slope of 1. To avoid redeposition, it must be created using multiple scans. Fortunately, because the contour is planar, the sputtering yield is always independent of position, so Eqn. 4 - 6 reduces to Eqn. 4 - 7 for every repetition of the scan, not just the first one. This makes application of the model quite simple. Substituting Eqn. 4 - 8 into Eqn. 4 - 7 gives a differential equation for the beam position as a function of time

$$ax = \frac{c}{\sqrt{\dot{x}^2 + \dot{y}^2}} \qquad 4 - 9$$

Using the technique of separation of variables, the following two differential equations are found

$$\dot{x}^2 - \left(\frac{c}{ax}\right)^2 + b^2 = 0 \qquad 4 - 10(a)$$

$$\dot{y}^2 - b^2 = 0 \qquad 4 - 10(b)$$

Finally, $x(t)$ and $y(t)$ are found by integrating Eqns. 4 - 10

$$x(t) = \pm \sqrt{(x(t_0))^2 \pm 2\left(\sqrt{\left(\frac{c}{a}\right)^2 - (bx(t_0))^2}\right)(t - t_0) - b^2(t - t_0)^2} \qquad 4 - 11(a)$$

$$y(t) = b(t - t_0) + y(t_0) \qquad 4 - 11(b)$$

If the beam position is controlled in accordance with Eqns. 4 - 11, then the contour described by Eqn. 4 - 8 will be produced.

The detailed time dependence of the beam position depends on the magnitudes of the various constants. In particular, because the sputtering yield is a function of the incident angle of the ion beam, which in turn depends on the angle of the contour, the constant c changes for each scan repetition. If the change in slope is to be the same for each repetition, a new solution to Eqn. 4 - 10(a) must be found for each new value of c.

Alternately, examination of Eqn. 4 - 10(a) shows that only the ratio c/a is important. If the contour is machined using a single solution, based on a single value for this ratio, then as c changes a must also change so that the ratio remains constant. For this technique Eqns.

4 - 11 describe periodic functions. There is no requirement that the periods of the two functions be the same, but the ratio of the periods must be an integer to ensure a fixed phase. Additionally, this ratio determines the pitch of the scan lines which should be less than the diameter of the beam to ensure a smooth surface.

The first step in applying Eqns. 4 - 11 is to estimate appropriate values for the various constants. A reasonable value for c/a is found by finding average values for both a and c. For a contour with a slope of 1 created in 1000 repetitions of the scan, on average, $a = 0.001$. The constant c depends on the beam current and spot size, and the target density and sputtering yield. With a *Ga* LMIS and 4 mrad beam defining aperture the single lens ion gun produces a beam current of about 0.25 nA. Interpolation of Fig. 1 - 2 gives a spot size of about 0.35 μm at 15 kV accelerating voltage and 25 mm working distance. The density of the *GaAs* target is 4.43×10^{10} atoms/μm^3. Assuming the angle varies continuously, the average sputtering yield is

$$S = \frac{1}{\theta_c} \int_0^{\theta_c} S(\theta) d\theta \qquad 4 - 12$$

where θ_c is the final angle of the contour. The average yield for a 45^0 contour, based on the fitted curve in Fig. 3 - 2, is 5.7. This give $c = 0.7\ \mu m^2/sec$.

This leaves the magnitude of the y scan velocity, b. The scan rate must be fast enough to avoid the nonlinear effects described by Yamaguchi, but slow enough to ensure adequate overlap of adjacent scan lines so the resulting machined surface is smooth. Previously, it was shown that total scan speeds as low as 5×10^{-2} cm/sec had no effect on the sputtering yield. The minimum y scan velocity in those experiments was actually much smaller, about 2×10^{-4} cm/sec. This should be a reasonable estimate for b.

Using these values for the constants and setting $t_0 = x(t_0) = 0$, Eqns. 4 - 11 become

$$x(t) = \sqrt{700t - 4t^2} \qquad 4 - 13(a)$$

$$y(t) = 2t \qquad 4 - 13(b)$$

where the position is in μm, and the time in seconds. For small values of t, the first term in the radical in Eqn. 4 - 13(a) dominates, and the beam position changes approximately as the square root of time. This was the case for all of the contours actually machined, where $x(t)$ was generally less than about 10 μm.

A computer equipped with the necessary digital to analog converters was programmed to control the beam in accordance with Eqns. 4 - 13, and several contours were machined in *GaAs*. Fig. 4 - 1 shows the beam position as a function of time in the x direction. The sampled points are

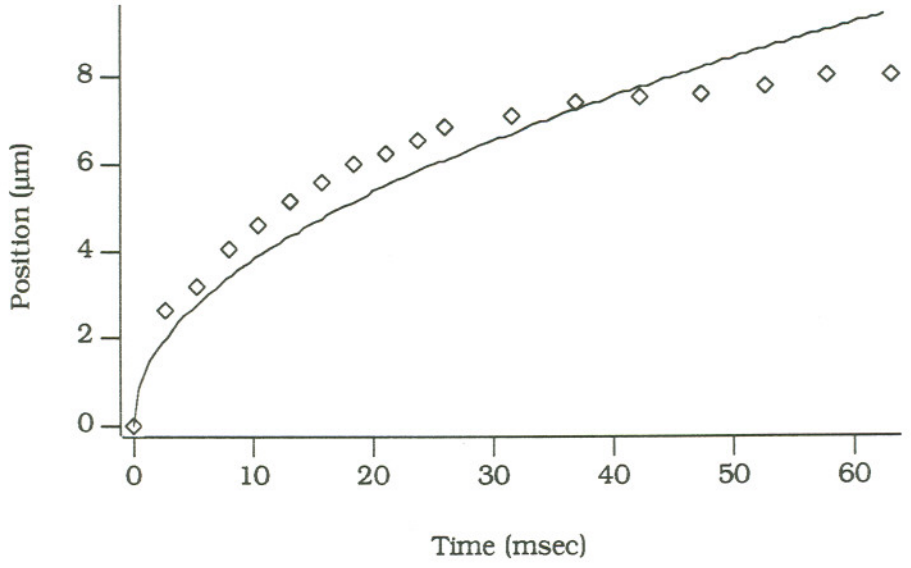

Fig. 4 - 1. The best fit of Eqn. 4 - 11 to the beam position as a function of time for the contours in Fig. 4 - 2.

meant to illustrate the shape of the curve, not the discrete nature of the digitally generated waveform. A curve similar to Eqn. 4 - 11(a) with $t_0 = x(t_0) = 0$ was fit to the data in Fig. 4 - 1, and is indicated by the solid line. There is fairly good agreement between the fitted curve and the experimentally determined beam position. The equation of the curve is

$$x(t) = \sqrt{739t - 56t^2} \qquad 4 - 14(a)$$

where the coefficient of t was varied to give the best fit, while that of t^2 was fixed by the y scan velocity. The velocity of the y scan was increased from Eqn 4 - 13 to simplify programming the computer. The y position as a function of time was a simple linear ramp, described by

$$y(t) = 7.5t \qquad 4 - 14(b)$$

Recall that both of these are periodic functions. The period of the x scan was about 60 msec, while that of the y scan was about 3 sec.

Fig. 4 - 2 shows cross sectional views of the contours machined in (100) oriented *GaAs* with 15 keV Ga^+ ions. As expected, the contours are nearly linear. Those made with fewer repetitions are closer to the ideal shape, as each repetition increases the significance of the discrepancy between the ideal waveform of Eqn. 4 - 14 and the actual beam position as a function of time.

Fig. 4 - 3 plots the slope of each contour as a function of the number of scan repetitions required to create it. The dashed line indicates how the slope should change if the sputtering yield increases according to Eqn. 3 - 15. This is not the dependence exhibited by the actual data points. Instead, the slope increases linearly with the number of repetitions, indicating that a is a constant. Since c/a is fixed, the sputtering yield must also be constant !

To check this, the sputtering yield was measured for each of the contours in Fig. 4 - 2. The results are shown in Fig. 4 - 4, which plots the yield as a function of contour angle. The dashed line represents the average sputtering yield of 7.0 ± 0.4. The figure clearly shows that within

Fig. 4 - 2. SEM photos of the planar slanted surface machined with the time dependence of the beam position shown in Fig. 4 - 1.

1 μm

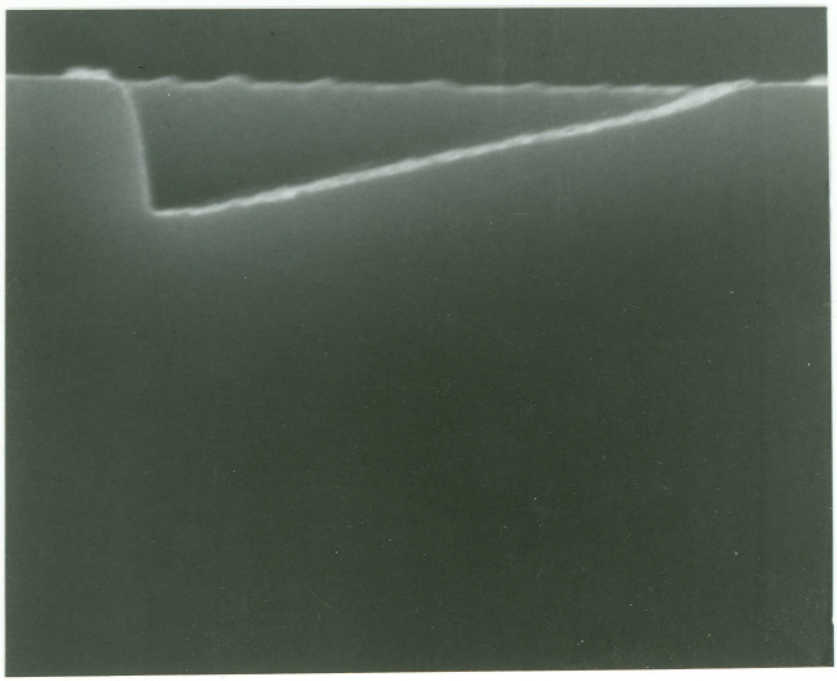

Fig. 4 - 2(b).

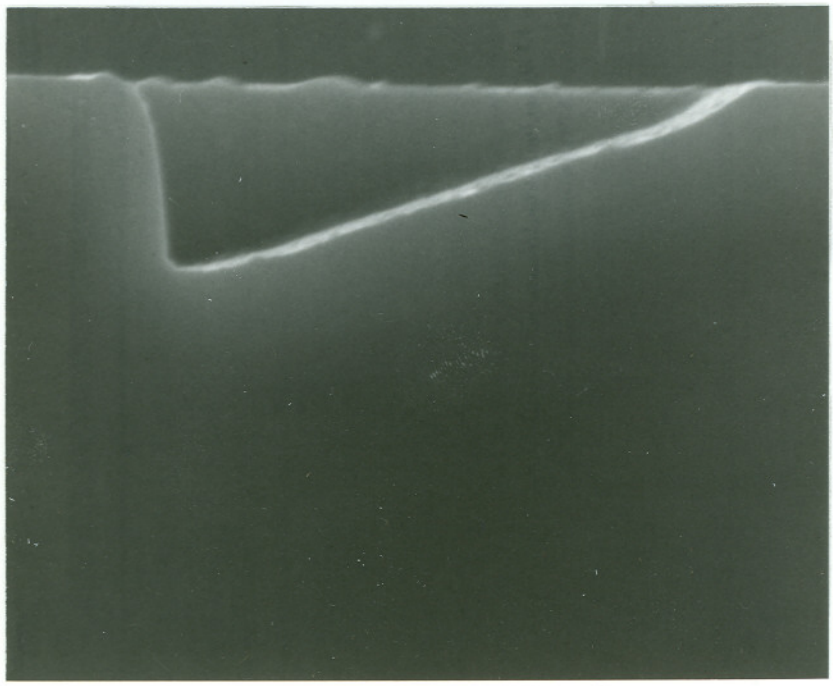

Fig. 4 - 2(c).

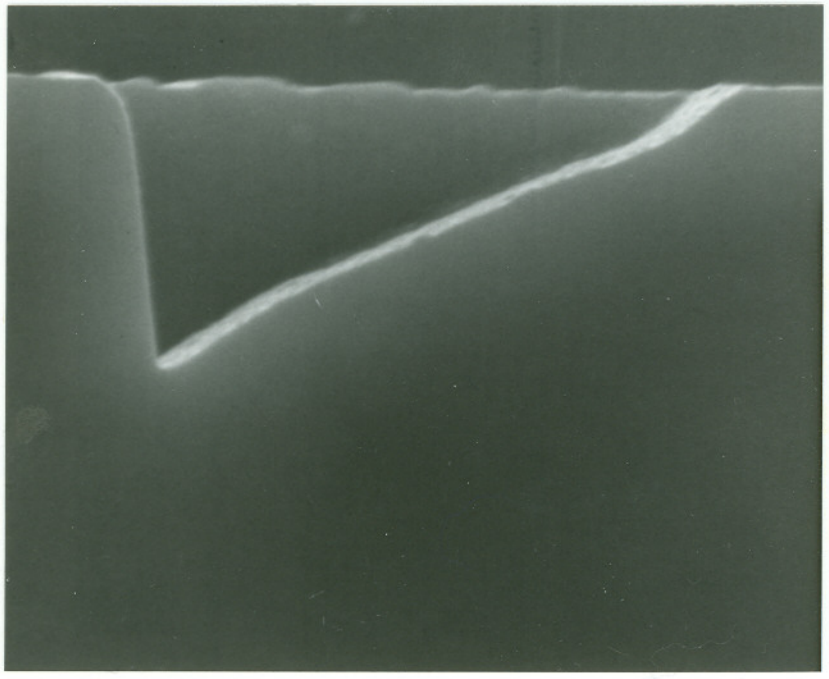

Fig. 4 - 2(d).

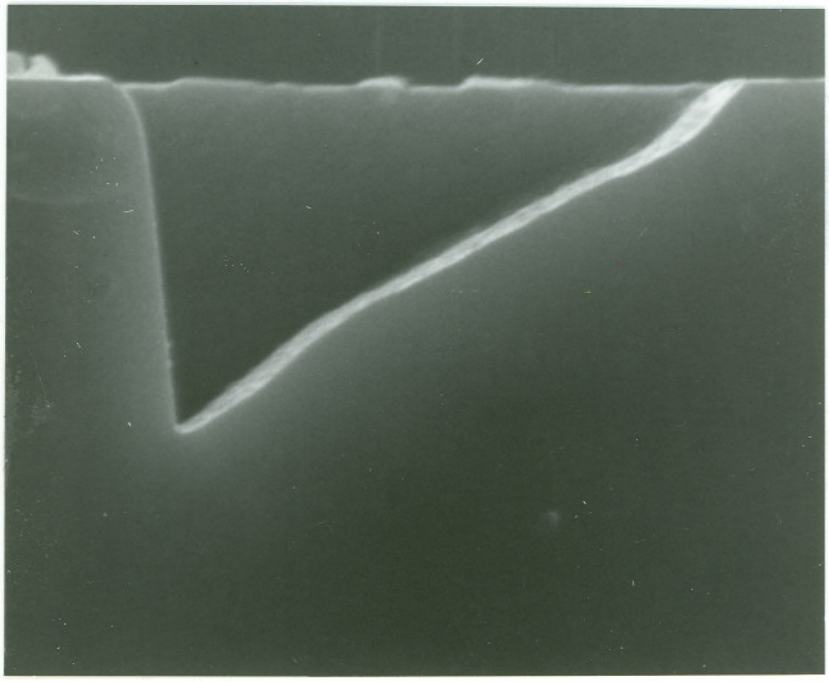

Fig. 4 - 2(e).

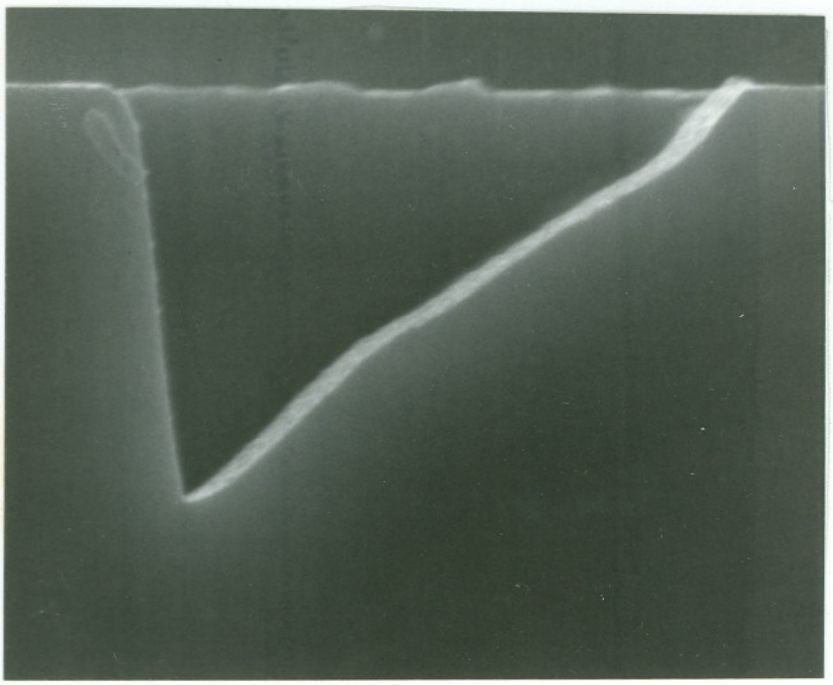

Fig. 4 - 2(f).

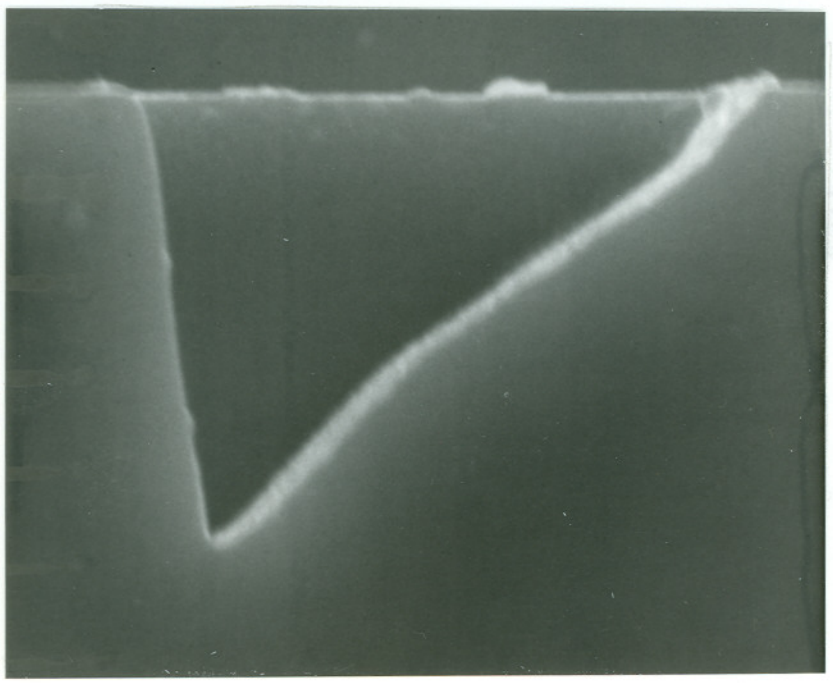

Fig. 4 - 2(g).

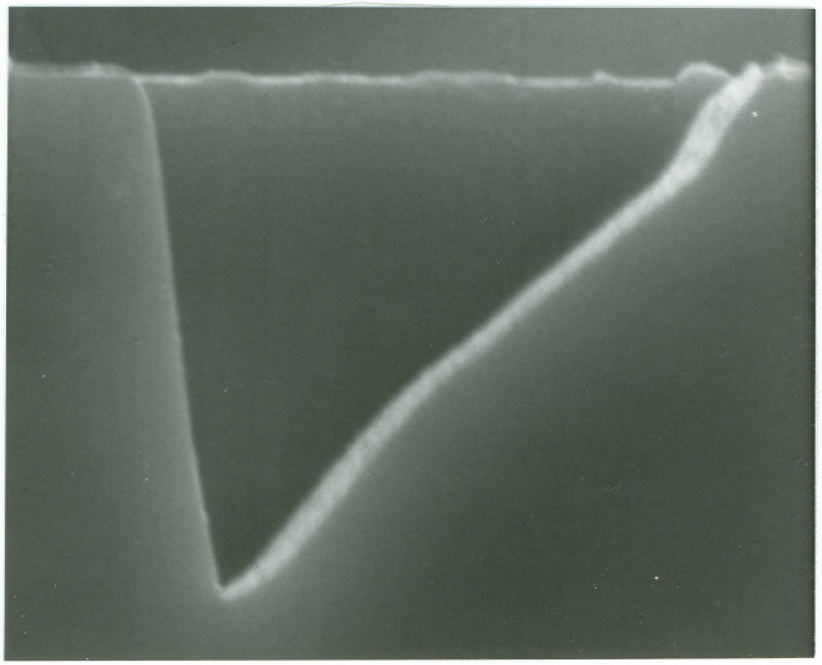

Fig. 4 - 2(h).

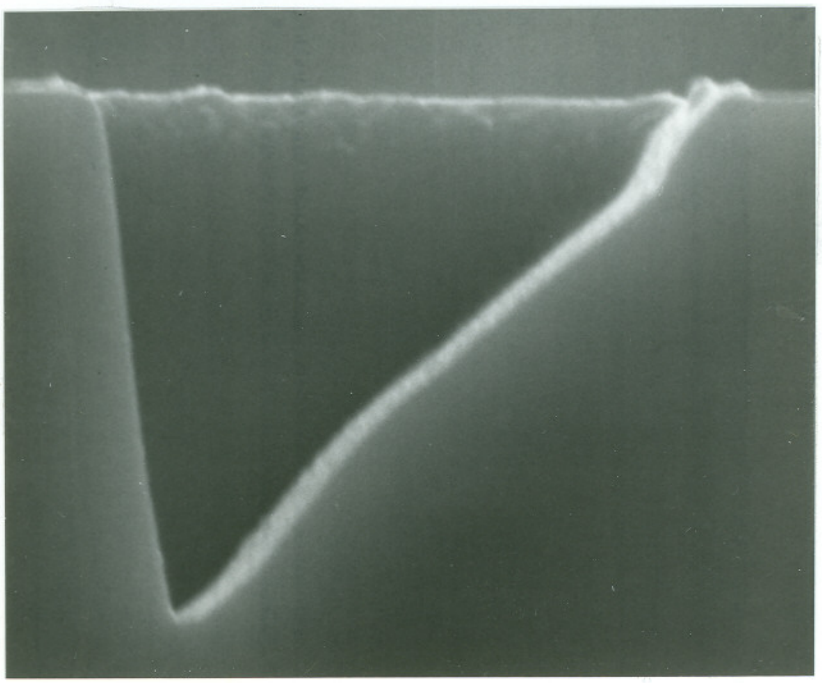

Fig. 4 - 2(g).

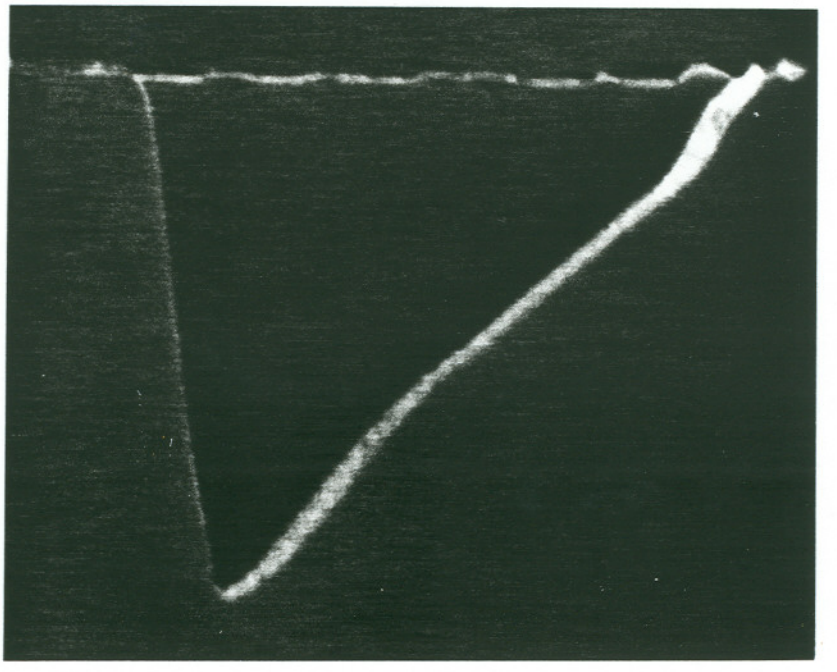

Fig. 4 - 2(h).

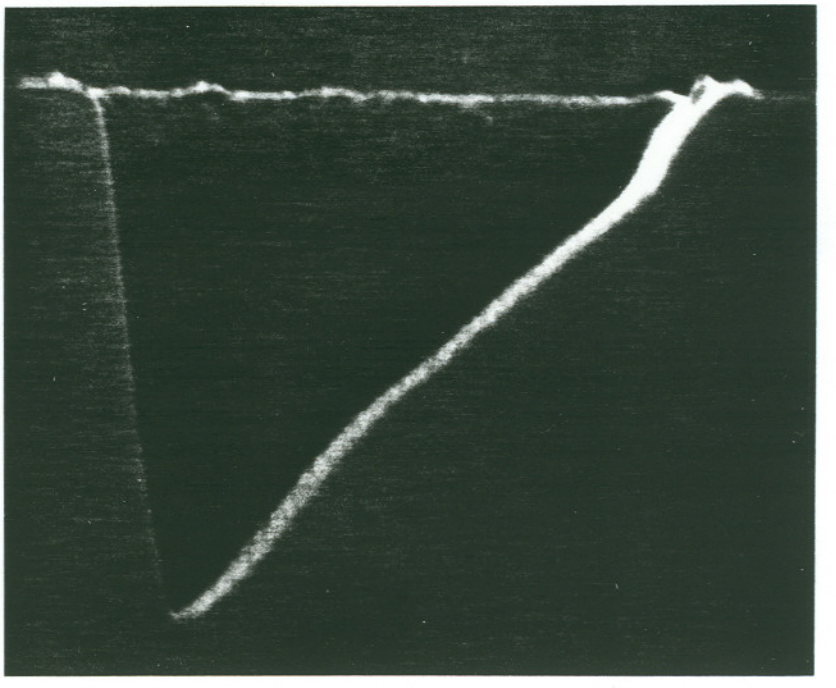

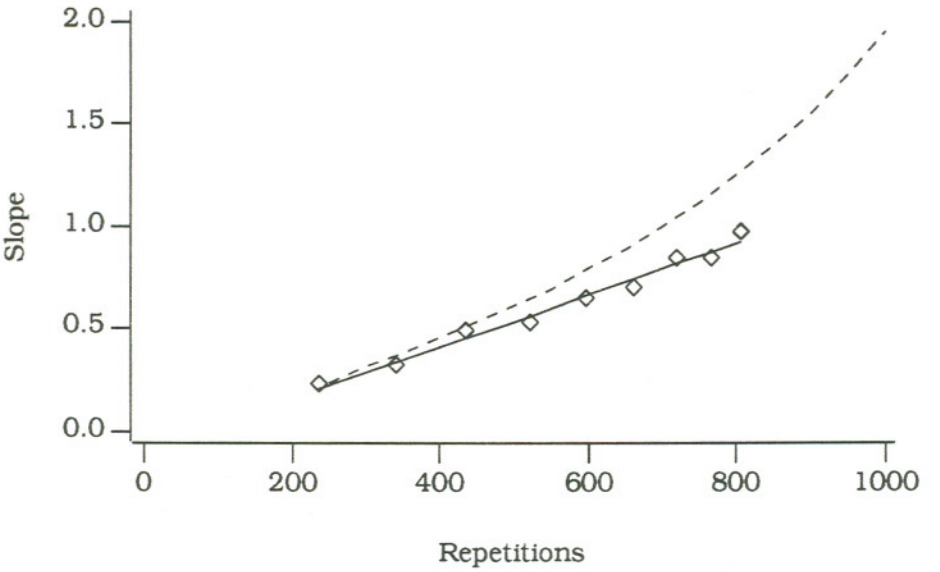

Fig. 4 - 3. Plot of the slope of the contours in Fig. 4 - 2 as a function of the number of repetitions of the scan required to create them. The dashed line indicates the behavior expected if the sputtering yield changes according to Eqn. 3 - 15 as the contour evolves. The solid line is a least squares fit of a straight line, which agrees well with the data, indicating that the sputtering yield can be treated as a constant.

experimental error, the yield is constant. The reason for this is not clear, but a constant yield greatly simplifies solution of Eqn. 4 - 6, which reduces to Eqn. 4 - 7 even for complex contours created with multiple scans of the ion beam.

It is interesting to compare this value for the yield to the yield which is consistent with Eqn. 4 - 14 and the contours of Fig. 4 - 2. Comparing Eqns. 4 - 11(a) and 4 - 14 shows that

$$2\,\frac{c}{a} = 739 \qquad 4 - 15$$

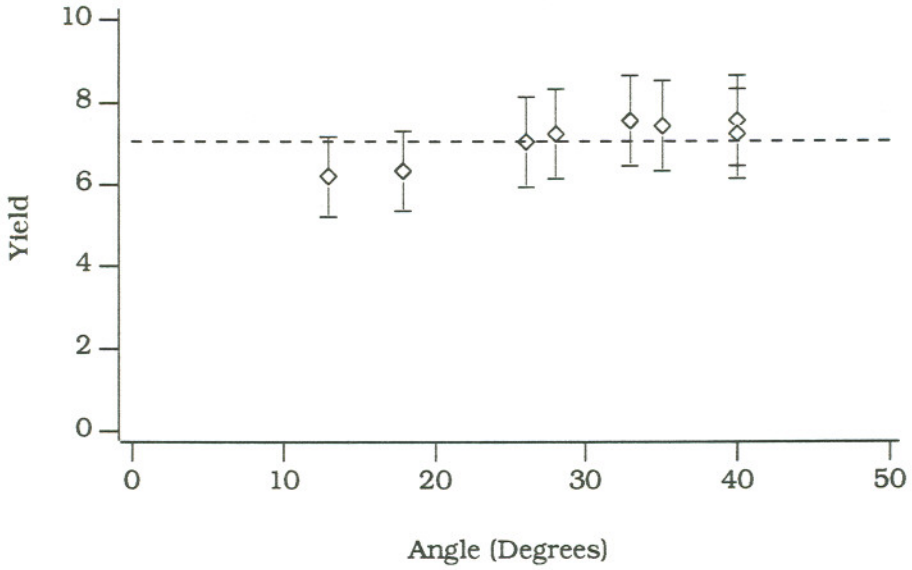

Fig. 4 - 4. Measured sputter yield as a function of the contour angle for each of the contours shown in Fig. 4 - 2. The dashed line represents the average for the 8 contours. Within experimental error, the yield is constant.

Comparing Eqns. 4 - 6 and 4 - 7 gives the definition of c, which along with Eqn. 4 - 15 gives an expression for the sputtering yield.

$$S = 739 \frac{\pi}{8} \frac{Nda}{6.25 \times 10^{18} I_{Beam}} \qquad 4 - 16$$

The measured beam current was 0.26 nA, and from the solid line in Fig. 4 - 3, $a = 1.2 \times 10^{-3}$. Plugging these values into Eqn. 4 - 16, along with the target density and spot size mentioned above, results in a sputtering yield of 3.3, less than half the average measured value.

One reason for the discrepancy may be the fit of Eqn. 4 - 11, to the experimentally determined beam position. All of the data points in

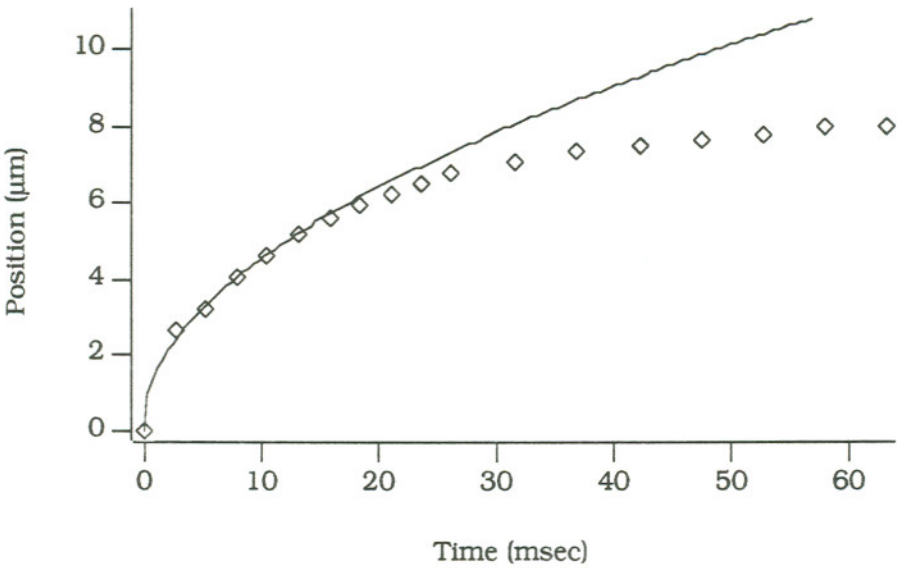

Fig. 4 - 5. The best fit of Eqn. 4 - 11 to the beam position as a function of time for the linear portion of the contours in Fig. 4 - 2.

Fig. 4 - 1 were weighted equally, while the most linear part of the contour is near the center. A new curve fitted to only those points where the contour is linear is shown in Fig. 4 - 5. The figure shows that for large values of t the beam position does not increase as rapidly as required, which agrees with the shape of the contours. Too much material was removed at the deep end of the contour resulting in the nonlinearity observable in most of the micrographs in Fig. 4 - 2.

The equation of the fitted curve in Fig. 4 - 5 is

$$x(t) = \sqrt{1023t - 56t^2} \qquad 4 - 17$$

which results in a larger value for c/a, and a larger sputtering yield. The new value is 4.6, still considerably smaller than the measured value.

Another possible source of error is the beam diameter. The value used in Eqn. 4 - 16 was interpolated from Fig. 1 - 2, which is based on calculations of the optical properties of the ion gun. The reliability of these calculations is generally quite good, but an actual measured value would be more appropriate. Several attempts were made to measure the beam diameter by scanning the beam over a knife edge. Unfortunately, sputtering of the edge made it difficult to obtain reproducible results.

More reproducible results were obtained by sputtering lines a single beam diameter in width, but this method calls into question the appropriate definition of the beam diameter. Fig. 4 - 6 shows how the width of the line changes with exposure time for 15 keV Ga^+ bombardment of *GaAs*. The FWHM of the sputtered lines remains constant, and agrees fairly well with the calculated beam diameter, but it is not a measure of the smallest feature which can be machined. The maximum width of the sputtered lines increases with the ion dose, and is always substantially larger than the FWHM. The increase in maximum width is attributed to the current distribution in the ion beam, and the increased importance of the "beam tails" as the exposure time increases.

Of these two values, the FWHM beam diameter is probably the more useful as it appears to be independent of the ion dose. A slightly larger

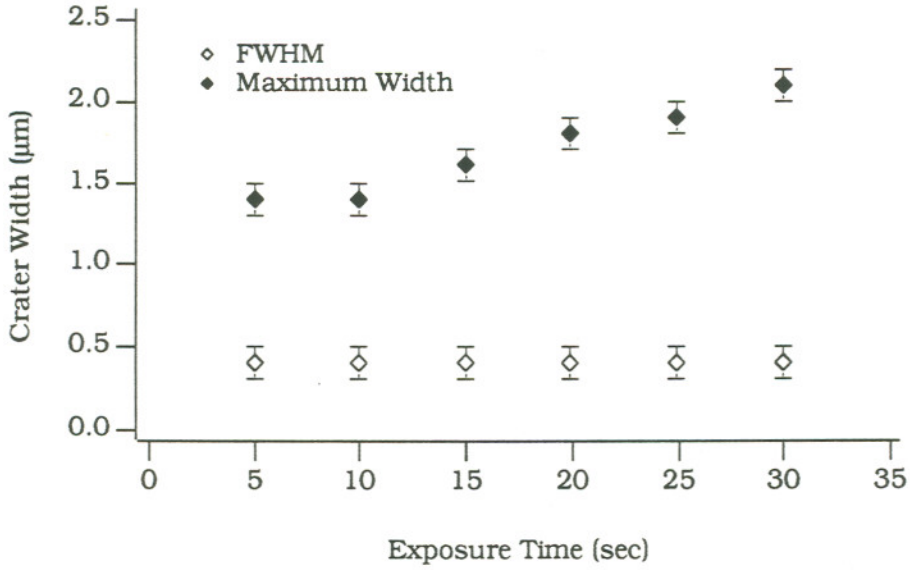

Fig. 4 - 6. Line width as a function of exposure time for single line scans machined in *GaAs* by 15 keV Ga^+ ions. The FWHM width of the lines is constant, while the maximum width increases with increasing exposure time. The increase is due to the increased importance of the beam tails as the exposure time is increased.

value for the beam diameter is required to give good agreement between the calculated yield and the experimentally measured value. This may be due to the assumption that the beam current is uniformly distributed across the diameter of the beam. A beam diameter of 0.53 μm gives excellent agreement between the yield calculated by Eqn. 4 - 16 and the measured yield, and is not far from the FWHM size.

B. *Planar Slanted Surface, Part II.*

While the contours shown in Fig. 4 - 2 are almost linear, there are obvious deviations caused by the difference between the desired beam

position as a function of time, and the actual relationship which existed when the contours were machined. To improve linearity, several attempts were made to control the beam more accurately. The most successful attempts, shown in Fig. 4 - 7, involved decreasing the scan velocity. The figure shows beam position as a function of time in the x direction as well as a least squares fit of a parabola to the sampled points. The fitted curves closely match the data. The agreement is much better than in Fig. 4 - 1 or Fig. 4 - 5. Again, the y scan was a simple linear ramp.

Fig. 4 - 8 shows contours machined with these ramps. They are much more linear than those shown in Fig. 4 - 2, although there are still small deviation from linearity for at least two of them. The nonlinearities that still exist can be explained in terms of redeposition. The contours in parts (a) and (b) of Fig. 4 - 8 were created according to Fig. 4 - 7(a). The scan proceeds from the shallow end of the crater to the deep end, where comparatively large amounts of material are being removed, some of which will redeposit on the contour. The material redeposited on the last repetition of the scan, when there is no opportunity for subsequent scans to remove it, may account for the nonlinearity. The scan shown in Fig. 4 - 7(b), used to create the contours in parts (c) and (d) of Fig. 4 - 8, is probably less prone to redeposition because the amount of material being removed at the end of the last scan is quite small.

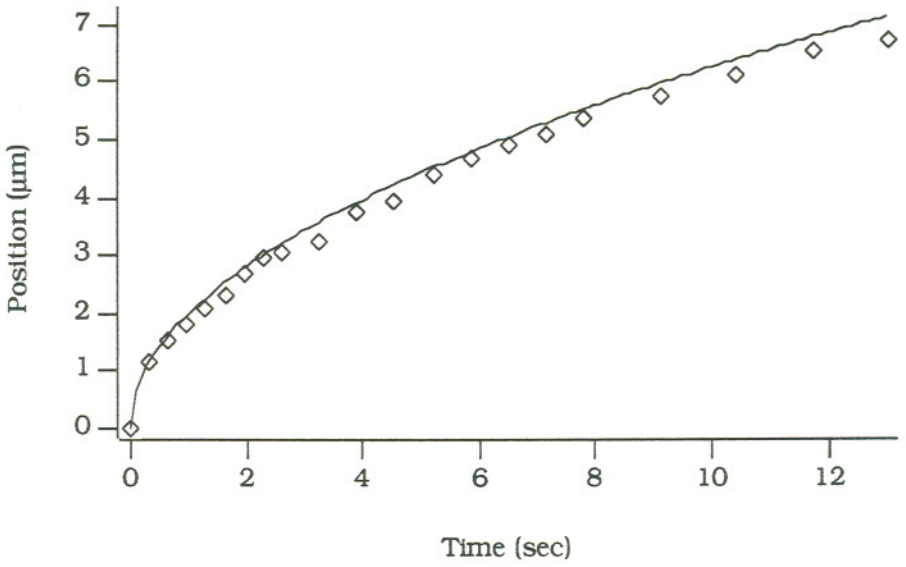

Fig. 4 - 7(a). Beam position as a function of time for the contours shown in Fig. 4 - 8 parts (a) and (b). The agreement between the data and the fitted curve is much better than in Fig. 4 - 1.

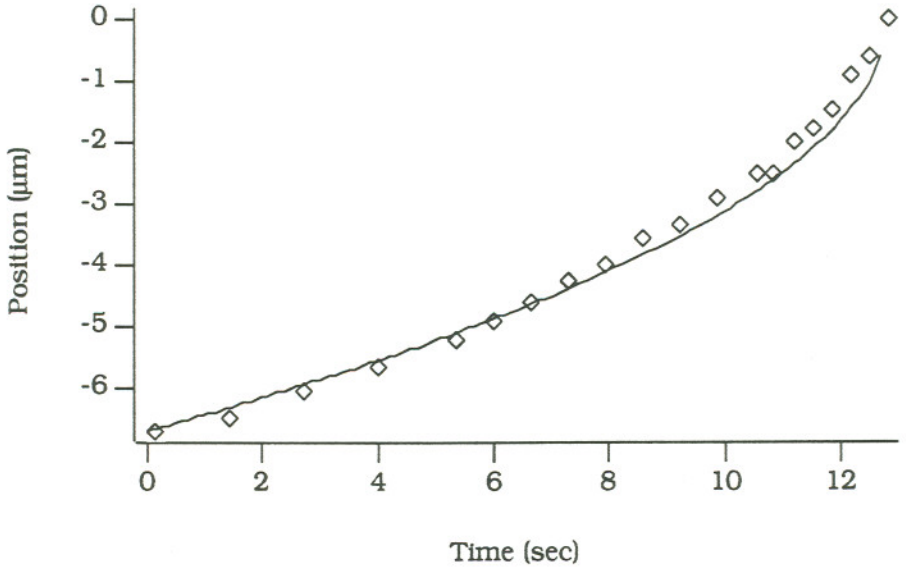

Fig. 4 - 7(b). Beam position as a function of time for the contours shown in Fig. 4 - 8 parts (c) and (d). Again, the fitted curve agrees well with the data.

Fig. 4 - 8. SEM photos of machined contours. Parts (a) and (b) were produced in accordance with Fig. 4 - 7(a).

1 μm

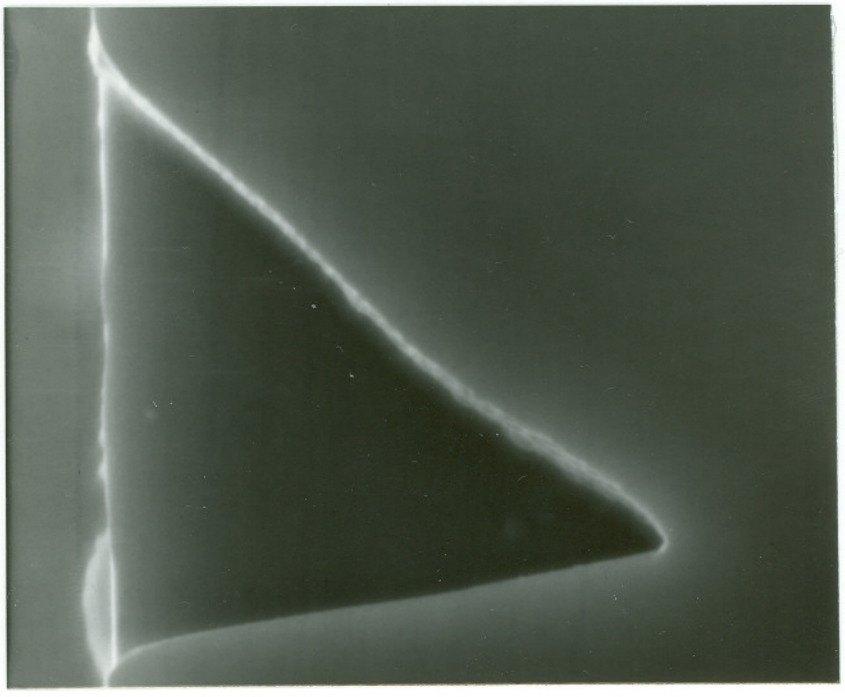

Fig. 4 - 8(b).

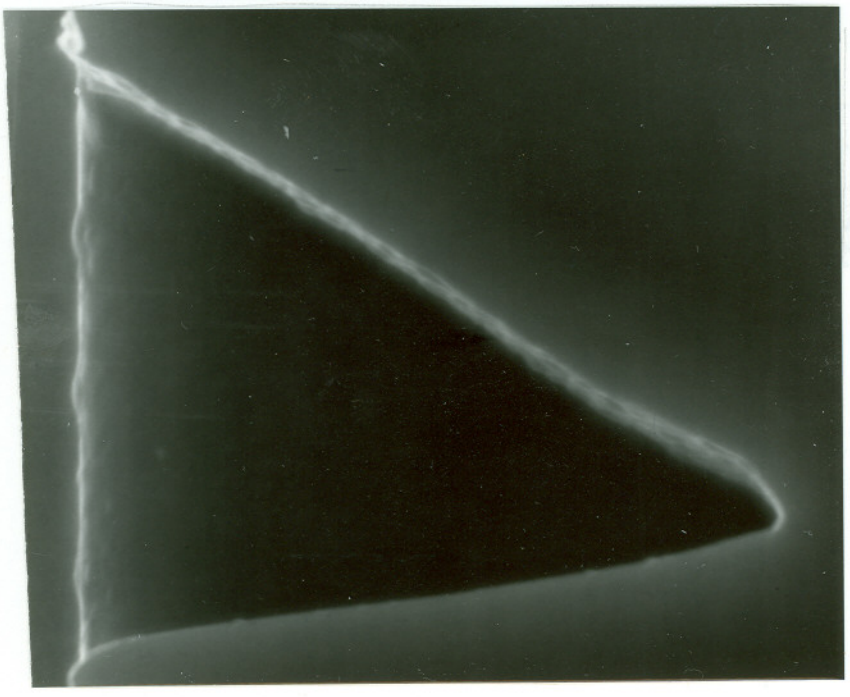

Fig. 4 - 8. SEM photos of machined contours. Parts (c) and (d) were produced in accordance with Fig. 4 - 7(b).

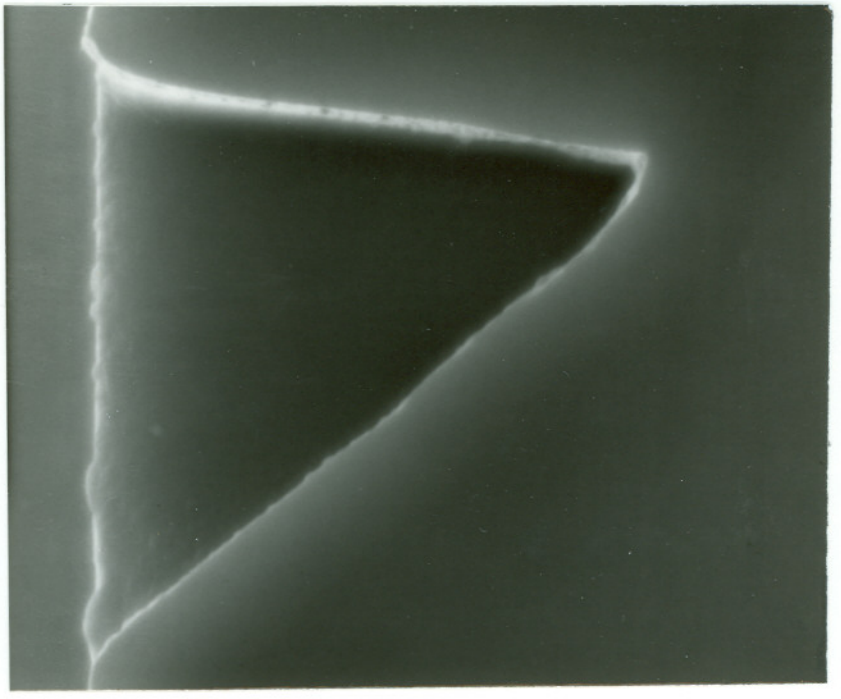

Fig. 4 - 8(d).

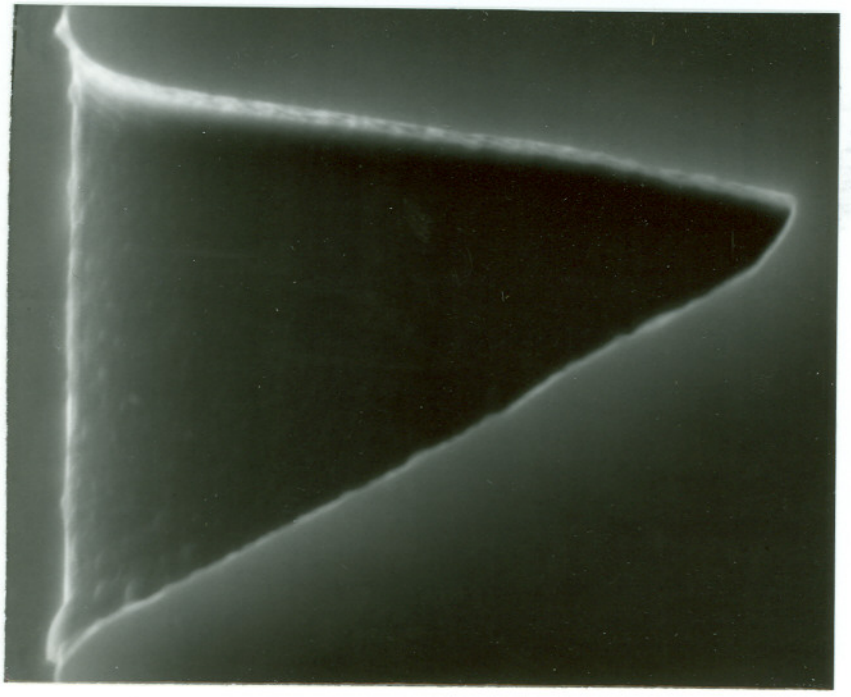

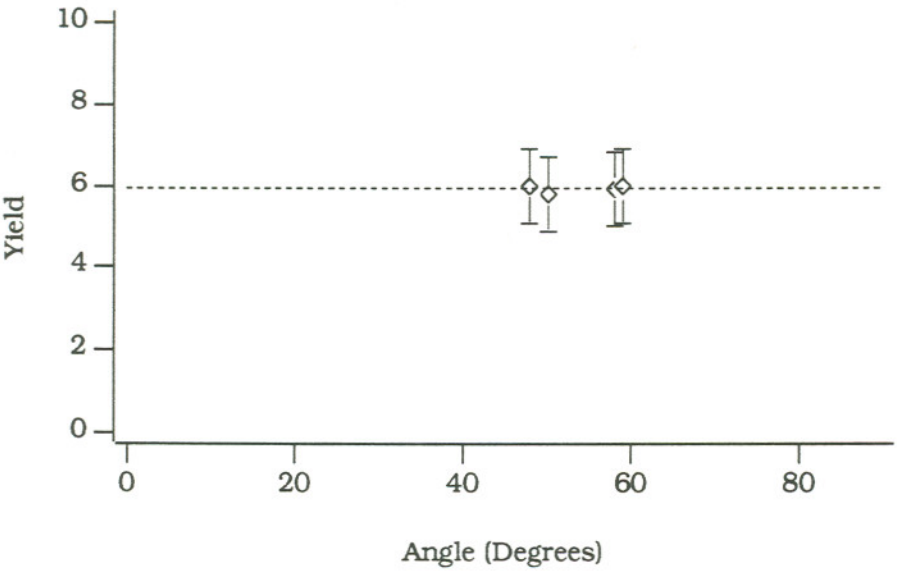

Fig. 4 - 9. Measured sputter yield as a function of the contour angle for each of the contours shown in Fig. 4 - 8. The dashed line represents the average for the 4 contours. Within experimental error, the yield is constant.

The sputtering yield for these contours was measured, and is plotted in Fig. 4 - 9. The average value is 5.9 ± 0.5, and is indicated by the dashed line. This is significantly smaller than the yield measured for the contours of Fig. 4 - 2, even though the angles are larger. Again, this is contrary to the angular dependence of the sputtering yield observed in the previous chapter.

Even though the contours of Fig. 4 - 2 and Fig. 4 - 8 were made under very similar conditions, the measured sputtering yield for the two sets of contours is quite different. The reason for the difference is not clear. Effects such as scan speed and redeposition can probably be ruled out. The average scan speed for the contours in Fig. 4 - 8 was smaller than

that of the contours in Fig. 4 - 2, but did not lead to a larger sputtering yield. Similarly, the yield for the deep, narrow contours is larger than that of the shallow, wide rectangular sputter craters of the previous chapter.

C. Planar Slanted Surface, Part III.

As stated previously, one of the reasons for creating a planar slanted surface is to fabricate a surface emitting diode laser. The contour shown in Fig. 4 - 8(d) is nearly ideal. It is quite linear, has an angle close to 45^0, and is the appropriate size, but there is still one problem. The crater wall opposite the machined contour forms one mirror of the optical cavity of the laser, and must be perpendicular to the top surface of the sample. Unfortunately, in all of the machined contours presented so far, this wall exhibits an angle of about 83^0 with respect to this surface.

The reason for this angle is twofold. First, the current density distribution of the ion beam makes it impossible to create an ion dose distribution with the infinite gradient required to produce a vertical surface. Second, at large incident angles similar to the angle at which ions are incident on the wall opposite the contour, ions are reflected from the target surface without depositing enough energy to cause sputtering. The sputtering yield of the "vertical" wall falls to zero before the wall is truly vertical.

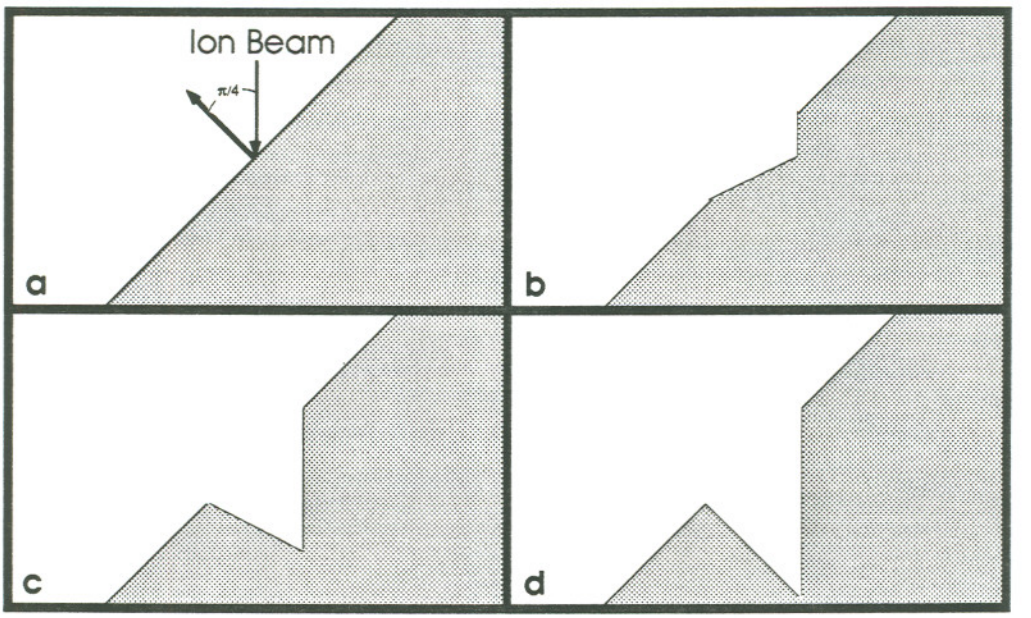

Fig. 4 - 10. Machining of a planar slanted surface with the ion beam incident at 45^0 relative to the surface normal. For a large enough ion dose, this method allows for creation of a surface which is parallel to the surface normal, and will act as one of the mirrors in the oscillating cavity of the diode laser.

Attempts were made to compensate for these effects. For example, the sample was tilted slightly to try and compensate for ion reflection. This increased the angle from 83^0 for a contour created with a normally incident beam, to 84^0 with the beam incident at 5^0, and 87^0 for a 10^0 angle of incidence. Larger angles may have increased the angle even further, but the sample tilt also effected the linearity of the contour. This may be due to ion reflection from the "vertical" wall.

A more successful attempt involved tilting the sample by 45^0 and using the beam to create the "vertical" wall while the 45^0 contour was defined by the angle of incidence. This is illustrated in Fig. 4 - 10 which

shows schematically how the contour evolves. Contours actually machined using this geometry are shown in Fig. 4 - 11. The beam position as a function of time was similar to that of Fig. 4 - 7(a), the only difference being the amplitude of the full scale deflection of the beam. Because of the tilt of the sample, the size of the contour is actually larger than the maximum deflection of the beam. Unfortunately, the ion doses used were too small to create a vertical wall, but it is evident that such a wall would be created for a large enough dose.

A plot of how the slope of the contour changes with the number of scan repetitions is shown in Fig. 4 - 12. Note that the slope of the surface starts at 1, in the coordinates of the ion beam, corresponding to the tilt of the sample relative to the beam. As in the case of normal incidence, a least squares fit of a line to the data points shows that the change in slope is linear as the number of repetitions increases. Again, this is evidence that the sputtering yield does not change with the angle of the contour.

The sputtering yield as a function of the contour angle is plotted in Fig. 4 - 13. The average value is 5.1 ± 0.3, indicated by the dashed line. This is nearly the same as the 5.9 ± 0.5 measured for the contours of Fig. 4 - 8, which were made with a similar time dependence of the beam position. The reason for the smaller sputter yield is not clear. According to the results for a rectangular sputter crater, an incident angle of 45^0

Fig. 4 - 11. SEM photos of the contours machined with the sample tilted relative to the incident ions.

1 μm

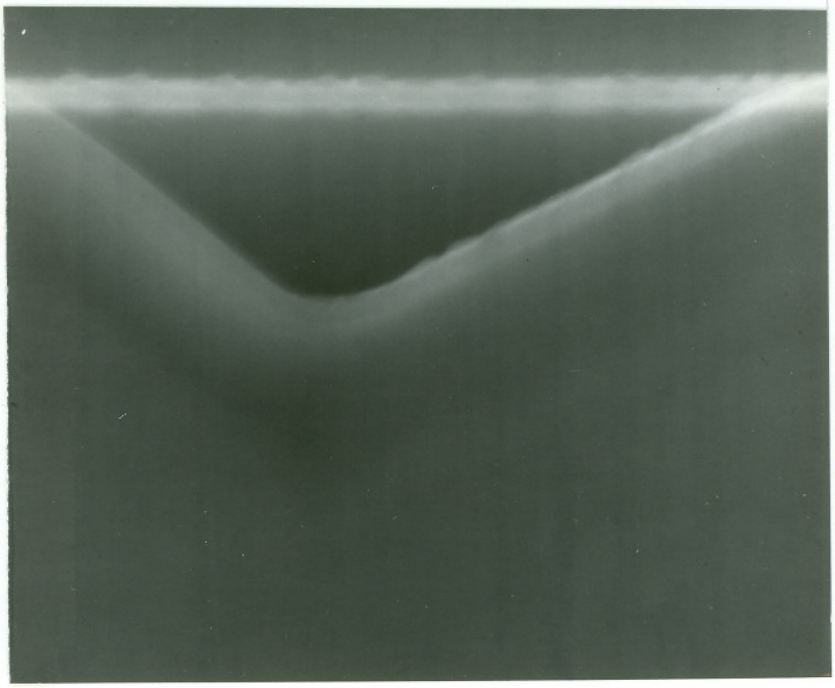

Fig. 4 - 11(b).

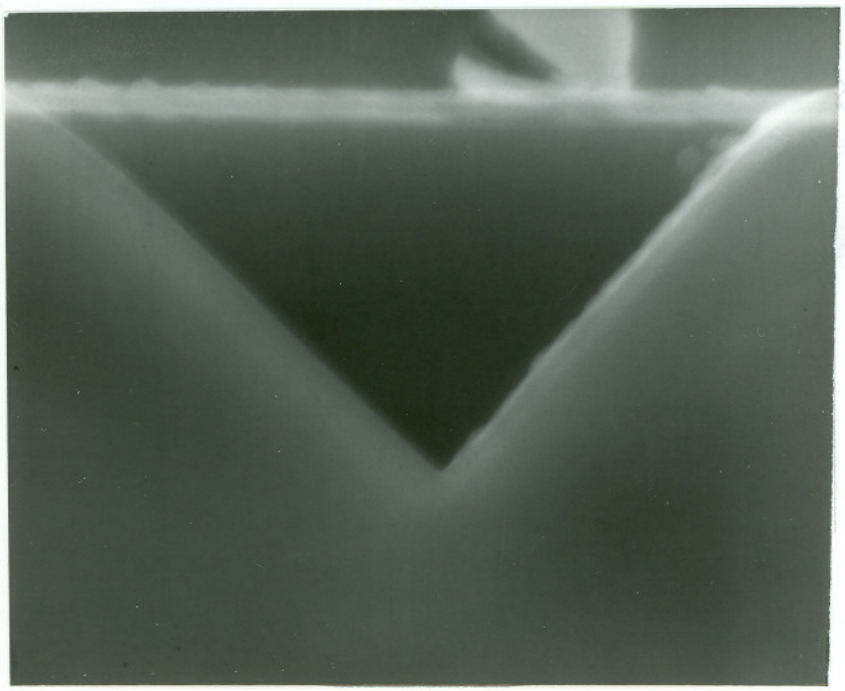

Fig. 4 - 11(c).

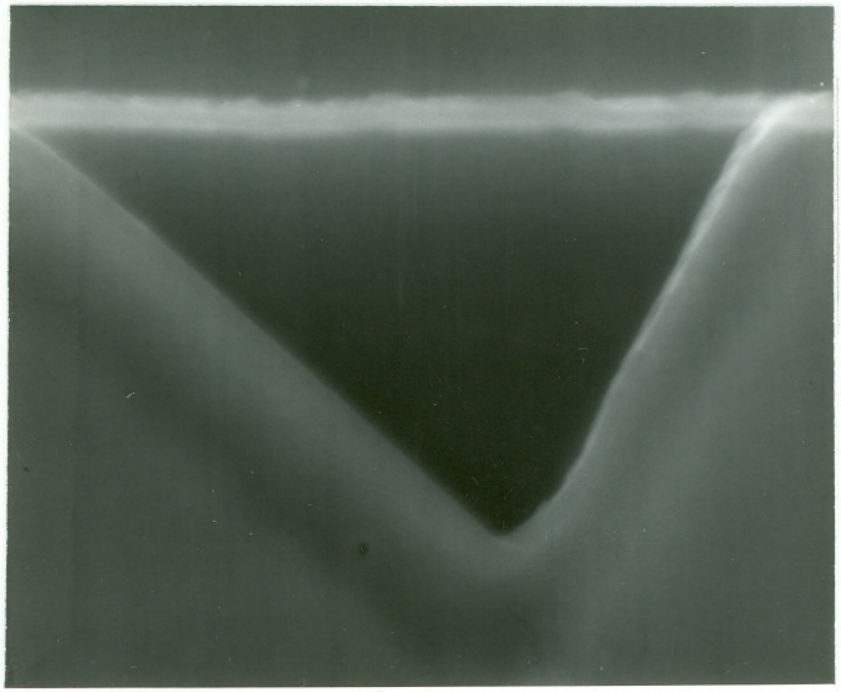

Fig. 4 - 11(d).

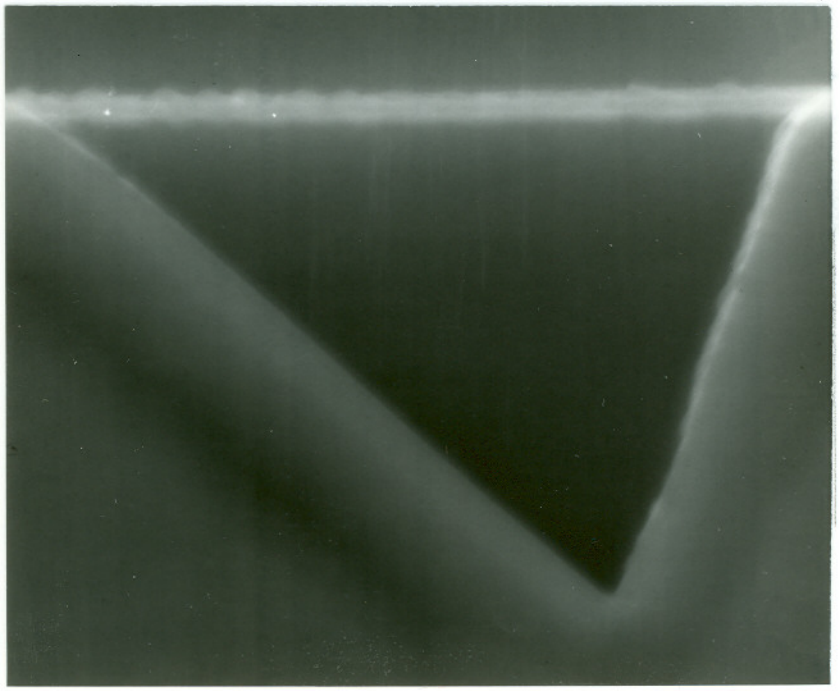

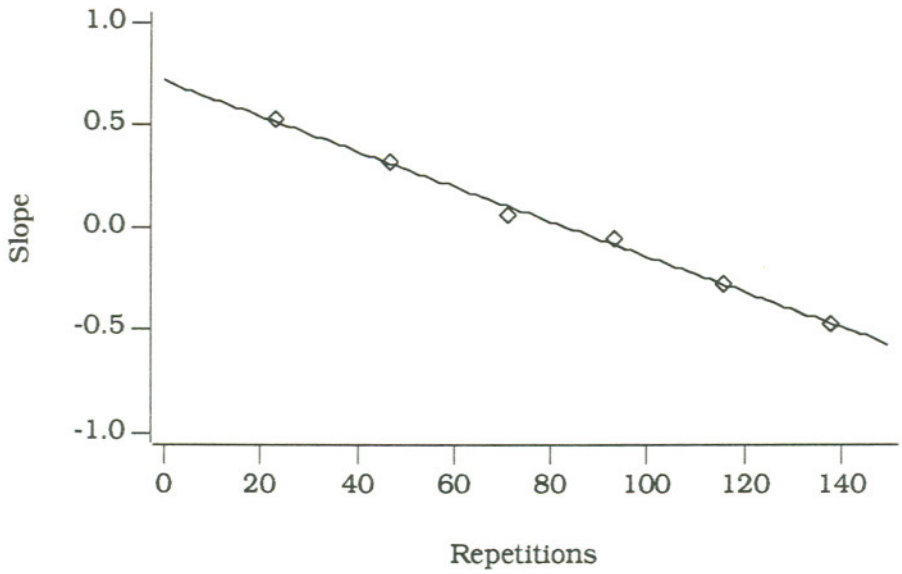

Fig. 4 - 12. Plot of the slope of the slanted surfaces shown in Fig. 4 - 11 as a function of the number of repetitions of the scan. A least squares fit of a line to the data shows that the relation is in fact linear.

results in a substantial increase in the sputter yield. This is further evidence that the angular dependence of the sputtering yield found for the creation of rectangular sputter craters is not applicable to FIBM of more complicated features.

D. Sinewave Surface.

As a second example of applying Eqn. 4 - 6 consider a sinusoidal surface described by the equation

$$z(x,y) = a\sin x \qquad 4 - 18$$

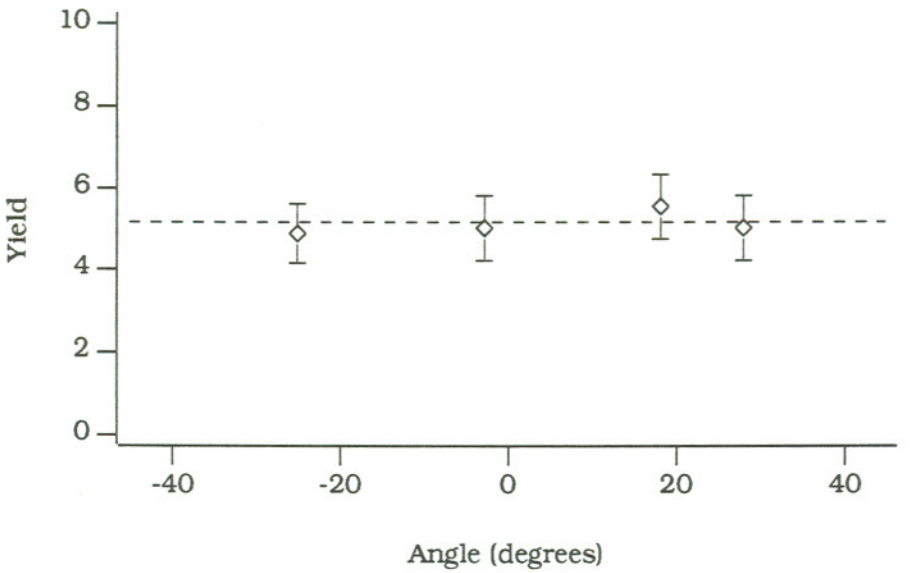

Fig. 4 - 13. Measured sputter yield as a function of the contour angle for each of the contours shown in Fig. 4 - 11(Note, this is not the same as the angle of incidence). The dashed line represents the average for the 4 contours. Within experimental error, the yield is constant.

Again, through the technique of separation of variables two differential equations are found for the beam position as a function of time.

$$\dot{x}^2 - \left(\frac{c}{a\sin x}\right)^2 + b^2 = 0 \qquad 4 - 19(a)$$

$$\dot{y}^2 - b^2 = 0 \qquad 4 - 19(b)$$

The solution to Eqn. 4 - 19(b) is trivial, while Eqn. 4 - 19(a) can be integrated to get t in terms of x.

$$t - t_0 = -\frac{1}{b}\ln\left[\frac{\frac{ab}{c}\cos x + \sqrt{1 - \left(\frac{ab}{c}\sin x\right)^2}}{\frac{ab}{c}\cos x_0 + \sqrt{1 - \left(\frac{ab}{c}\sin x_0\right)^2}}\right] \qquad 4 - 20$$

In order to invert this equation and get x in terms of t, some simplifying assumptions must be made.

First, note that for the radical in Eqn. 4 - 20 to be real for all values of x requires that

$$\frac{ab}{c} \leq 1 \qquad 4 - 21$$

where a is the amplitude of the sine wave, b is the magnitude of the y scan velocity, and c is the same constant as in the previous example. As shown above, for 15 keV Ga^+ bombardment of $GaAs$ using the single lens ion gun $c \approx 1\ \mu m^2/sec$, so creation of a sine wave 1 μm in amplitude requires a y scan velocity less than about 1 μm/sec. In fact, for the current application the y scan velocity was limited by the speed of the computer to a value much smaller than this. The y scan velocity actually used was about 0.03 μm/sec, which makes

$$\frac{ab}{c} << 1 \qquad 4 - 22$$

Setting $t_0 = \cos x_0 = 0$, and using Eqn. 4 - 22, Eqn. 4 - 20 can be approximated by

$$t \approx -\frac{1}{b} \ln\left[1 + \frac{ab}{c} \cos x\right] \qquad 4 - 23$$

Eliminating the logarithm from the right hand side of Eqn. 4 - 23 gives

$$\exp[-bt] \approx \left[1 + \frac{ab}{c} \cos x\right] \qquad 4 - 24$$

For sufficiently small values of t, the left hand side of Eqn. 4 - 24 can be approximated by

$$\exp[-bt] \approx 1 - bt \qquad 4 - 25$$

Combining Eqn. 4 - 24 and Eqn. 4 - 25 gives a solution for $x(t)$ of the form

$$x(t) \approx \arccos\left[-\frac{c}{a}t\right] \qquad 4 - 26$$

By adding together a series of terms of the form

$$x(t) \approx x_0 + \arccos\left[-\frac{c}{a}(t + t_0)\right] \qquad 4 - 27$$

a relationship between beam position and time similar to that shown in Fig. 4 - 14 is obtained. A similar time dependence was used to create the contour shown in Fig. 4 - 15(a). As predicted, the machined surface is sinusoidal. The amplitude of the sinewave is 1.3 μm, and the period is 2.1 μm. Examination of Fig. 4 - 14 shows that the beam position changes almost linearly with time, the deviations from linearity are quite small, but the resulting machined surface is markedly nonlinear.

The same computer generated waveform used to create the contour in Fig. 4 - 15(a) was also used to create the contour of Fig. 4 - 15(b). The only difference between the two was the full scale deflection of the ion beam. The contour in part (b) is about 0.7 times the size of the contour in part (a), and the corresponding decrease in the scan velocity of the ion

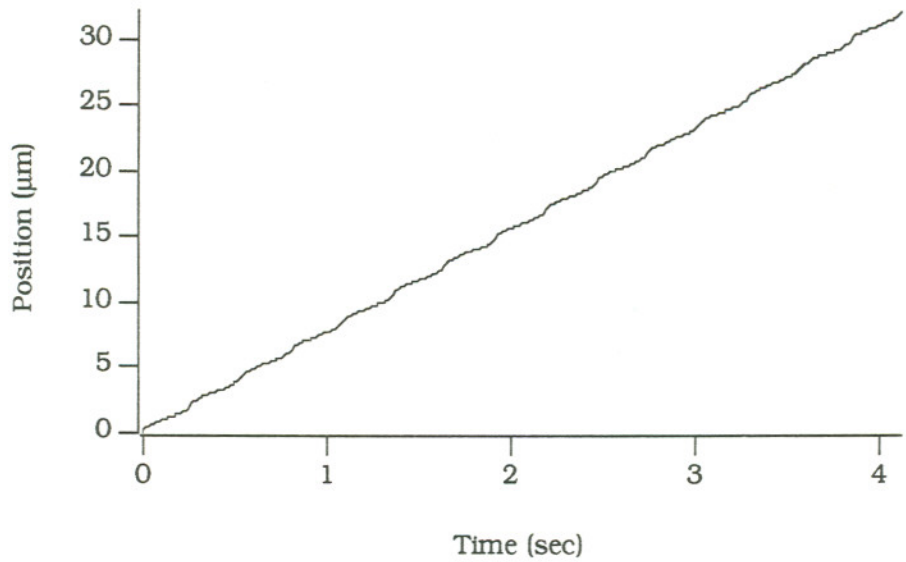

Fig. 4 - 14. Example of the beam position as a function of time required to create a sinewave surface. This is similar to the time dependence of the beam position used to create the contour in Fig. 4 - 15(a).

beam and increase in depth of the contour was sufficient to make second order effects, such as redeposition and self focusing, have a significant effect on the shape of the contour. This could most likely be avoided by using multiple rapid scans of the beam. Unfortunately, in this instance the limited speed of the computer made it impossible to use this technique. Each contour was created with a single scan which took approximately 16.5 min to complete.

Fig. 4 - 15. SEM photos of the machined contours. The same computer program was used to create both contours, but second order effects such as redeposition and self focusing of the beam effected the shape of the contour in part (b).

5 μm

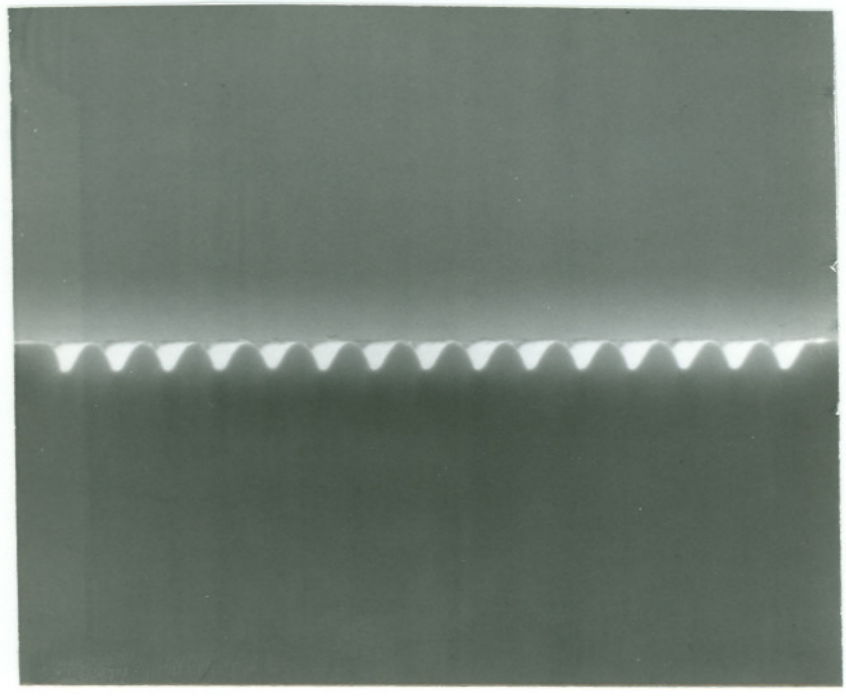

Fig. 4 - 15(b).

5 μm

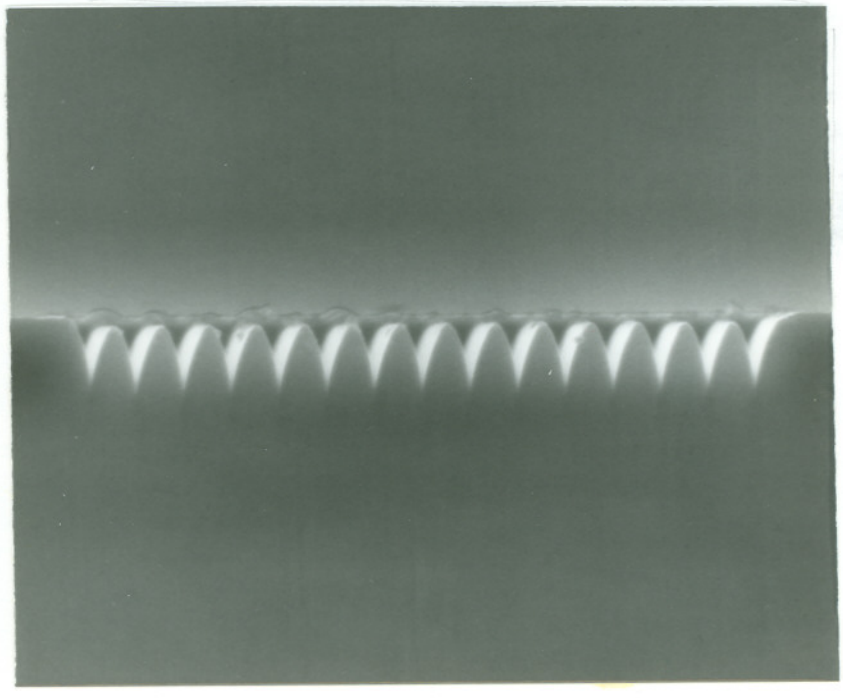

E. 3-D Dome-Shaped Surface.

So far, the depth of all the machined contours has been independent of y. The primary reason for this is simplicity. Because the technique of separation of variables can be used, solution for the appropriate time dependence of the beam position is very simple. Similarly, it is easy to compare the shape of the machined contour to the desired shape. A second consideration was the speed of the computer used to control the beam. Complicated contours mean slow scan speeds where secondary effects become important, effects which were ignored in deriving Eqn. 4 - 6 but which were already affecting the shape of the sinewave contours of the previous section. However, even with these limitations it is interesting to see if more complicated contours can be fabricated.

Consider a contour of the form

$$z(x,y) = \frac{a}{\sqrt{\left(\frac{1}{\sin x}\right)^2 + \left(\frac{1}{\sin y}\right)^2}} \qquad 4 - 28$$

A three dimensional plot of this contour is given in Fig. 4 - 16 (Note that in the limit as x or y approaches $n\pi$, where n = 0, 1, 2, ..., the depth of the contour remains finite). This contour was chosen because both $x(t)$ and $y(t)$ are of the same form as Eqn. 4 - 26. To see this, start by

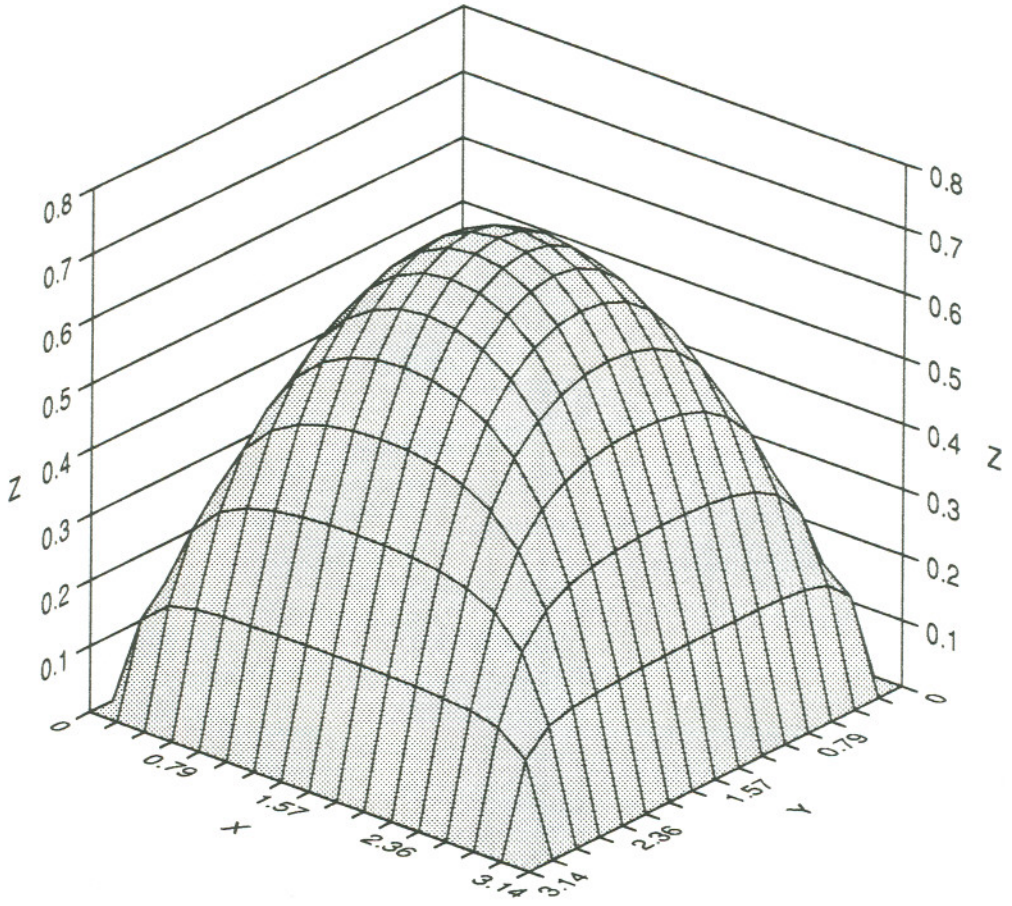

Fig. 4 - 16. Three dimensional plot of a contour of the form given in Eqn. 4 - 28.

substituting Eqn. 4 - 28 into Eqn. 4 - 7 and using the technique of separation of variables.

$$\left(\frac{a}{c}\,\dot{x}\right)^2 - \frac{1}{\sin^2 x} = b \qquad 4 - 29(a)$$

$$\left(\frac{a}{c}\,\dot{y}\right)^2 - \frac{1}{\sin^2 y} = b \qquad 4 - 29(b)$$

For the special case $b = 0$,

$$\dot{x} = \frac{c}{a} \frac{1}{\sin x} \qquad 4 - 30(a)$$

$$\dot{y} = \frac{c}{a} \frac{1}{\sin y} \qquad 4 - 30(b)$$

Eqns. 4 - 30 can be integrated to give t in terms of x, and the result inverted to give x in terms of t. Doing this, the time dependence of the beam position is found to be

$$x(t) = x_0 + \arccos\left[-\frac{c}{a}(t + t_0)\right] \qquad 4 - 31(a)$$

$$y(t) = y_0 + \arccos\left[-\frac{c}{a}(t + t_0)\right] \qquad 4 - 31(b)$$

which is the same as that of the simple sinewave surface of the previous section. The computer software already existed for this form of $x(t)$, which was the reason for choosing this contour.

By combining a series of terms of the form of Eqn. 4 - 31, a waveform similar to that shown in Fig. 4 - 14 was generated, and the contour in Fig. 4 - 17 was created. The machined contour is very close in shape to the ideal contour of Fig. 4 - 16. This is further evidence that the simple model presented above can be used to produce fairly complicated three dimensional contours.

Fig. 4 - 17. SEM photos of the machined contour. Part (b) shows a cross sectional view of the contour.

5 μm

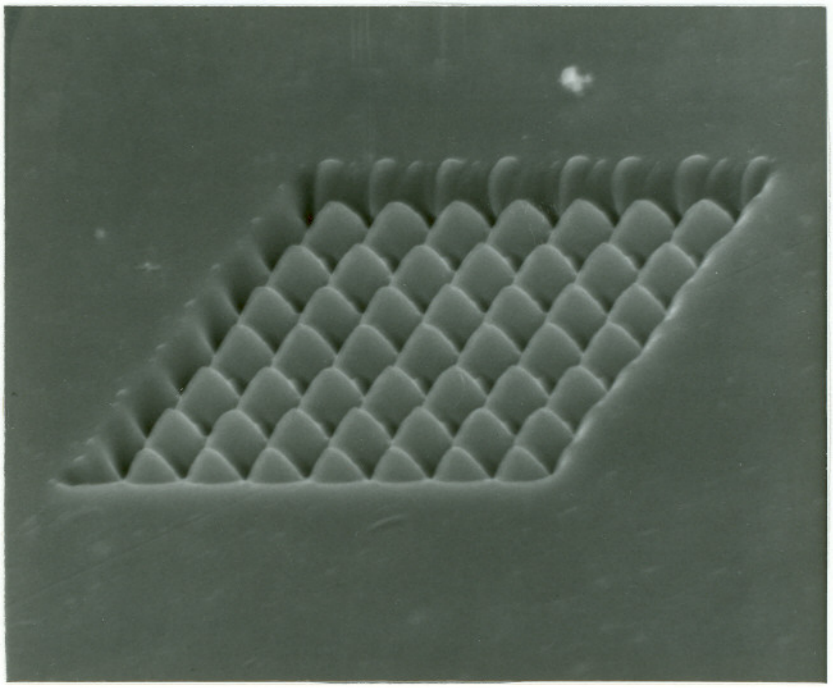

Fig. 4 - 17(b).

2 μm

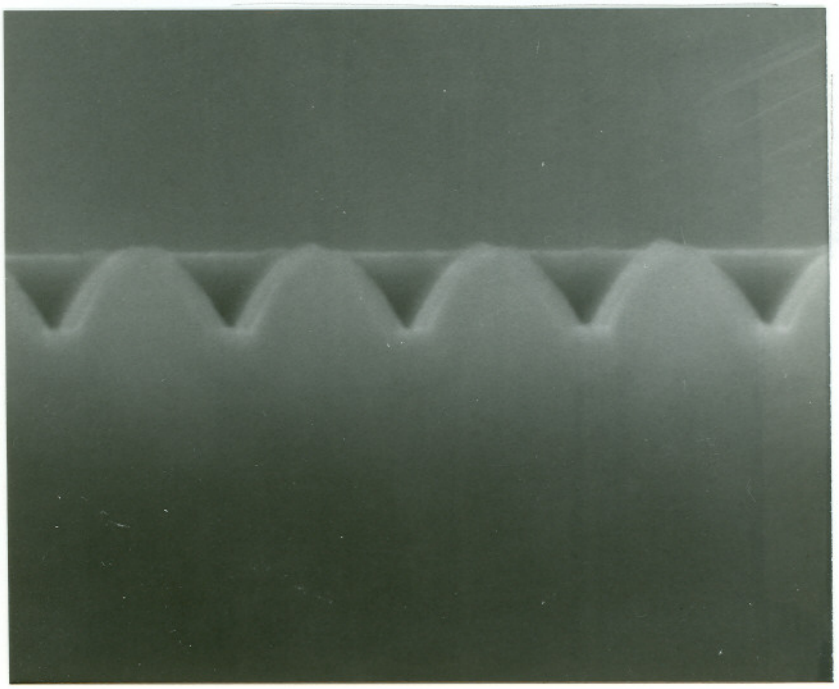

Conclusions

Focused ion beam micromachining is rapidly becoming an important technique for fabricating micron size and submicron size features. One common requirement in most applications of FIBM is the need to know the removal rate of the material being sputtered. The above experiments were designed to test how well the linear cascade theory predicts the sputtering yield for a given ion target combination, and how the bombardment conditions affected the measured sputtering yield. Several interesting results were obtained.

I. Sputtering Yield Measurements.

Sputtering yield measurements were made for several common ion target combinations, and the results compared to the predictions of the

linear cascade theory. In particular, the energy and angular dependence of the sputtering yield were compared to the predictions of the theory.

A. Ga *Bombardment of* GaAs.

The angular dependence of the sputtering yield closely followed the theoretical prediction, indicating that even though the target material was a single crystal, channeling was not significant. The lack of channeling was attributed to the amorphization of the target by the incident ions. The ion doses typical of FIBM are much higher than those required to cause amorphization. Similarly, the energy dependence of the sputtering yield also agreed well with theory. These two results indicate that it may be possible to apply the linear cascade theory of sputtering to FIBM of single crystal materials.

Unfortunately, the theory seriously underestimated the sputtering yield. The discrepancy is most likely due to uncertainty in the surface binding energy of the *GaAs*. No reliable data was available for this quantity. The high ion doses typical of FIBM significantly affect the composition of the target surface, which in turn affects the surface binding energy. Formation of *Ga* rich droplets on the bombarded surface are evidence of the changes in surface composition induced by the ion beam.

Because of the good agreement between the predicted shape of the angular and energy dependence of the sputtering yield and the experimental data, the surface binding energy was used as a fitting parameter to fit the predictions of the theory to the data. This value for the surface binding energy was then checked against the results obtained for *Au* bombardment of *GaAs*.

B. Au *Bombardment of* GaAs.

Again, there was good agreement between the predicted angular and energy dependence of the sputtering yield and that measured experimentally. The main difference between the *Au* and *Ga* data was the increased yield observed for *Au*. This increase resulted in a decreased altered layer thickness, which eliminated the formation of *Ga* rich droplets on the bombarded surface. The higher yields and lack of droplets make the *Au* LMIS interesting for the machining of opto-electronic structures where large amounts of material must be removed and optically smooth surfaces must be produced. Unfortunately, the composition of the beam limits the usefulness of the source unless major modifications are made to the primary focusing column.

Unfortunately, despite the good agreement the calculated sputtering yield was again much less than the measured value, even when using the surface binding energy calculated from the *Ga* results. This was

again attributed to the composition of the surface layer. The *Ga* and *Au* bombarded surfaces show evidence of radically different compositions, which apparently result in radically different surface binding energies. It appears that this is the limiting factor in successfully applying the linear cascade theory to FIBM of *GaAs*.

C. Ga *Bombardment of (100) Oriented* Si.

The energy dependence of the yield for normally incident ions showed good agreement with the theory. There was little variation in the sputtering yield over the range of energies tested. The measured yield also agreed well with the measurements of other investigators made at both higher and lower energies.

The angular dependence of the sputtering yield agreed well with theory for angles between about 20^0 and 60^0, but for smaller angles the yield dropped off slightly more rapidly than predicted. This may have indicated that channeling was influencing the sputtering yield. The calculated values for the sputtering yield were considerably larger than the measured yields, offering further evidence that channeling may have been influencing the yield. To determine if channeling was indeed significant, a second crystal orientation of *Si* was also bombarded.

D. Ga *Bombardment of (111) Oriented* Si.

The energy dependence of the sputtering yield for the (111) oriented crystal was similar to that seen for the (100) orientation, and again agreed well with theory. Similar results were also obtained for the angular dependence of the sputtering yield. The yield again decreased slightly more rapidly than expected for angles less than about 20^0. Also, the linear cascade theory again overestimated the yield by about a factor of 2. All of these results were consistent with the conclusion that channeling was significantly influencing the sputtering yield.

However, comparison of the sputtering yield for the two different crystal orientations showed that there was no measurable difference. This was strong evidence that channeling was not a factor. Furthermore, as was the case for *GaAs*, the ion doses typical of FIBM are far greater than those required to amorphize the target. For this reason, channeling was ruled out as a explanation for the discrepancy between the calculated sputtering yield and the experimentally determined value. The difference was again explained in terms of the changes in surface binding energy produced by the bombarding ions.

II. Vector Scanning.

A differential equation was derived which, for a given surface contour, could be solved for the beam position as a function of time. Controlling the beam according to the solution resulted in the fabrication of the given contour. Two major assumptions were made in deriving the equation. First, second order effects such as redeposition and self focusing of the ion beam were ignored. It was assumed that the depth of the sputter crater depended only on the ion dose, and increased linearly with dose. This is a valid assumption for the creation of relatively shallow sputter craters or for deeper craters created with fast multiple scans of the ion beam. The second assumption was that the current density distribution of the ion beam was uniform.

Following the derivation, several examples were presented to illustrate application of the differential equation to fabrication of specific contours. The applicability of the above sputtering yield measurements to the fabrication of these more complicated structures was also tested.

A. FIBM of a Planar Slanted Surface.

Fabrication of this contour resulted in several interesting observations. First, the sputtering yield was found to be independent of the final angle of the contour, indicating that the angular dependence of

the sputtering yield could be ignored. If this is true for all contours, it greatly simplifies solution of the differential equation. Next, it was found that the beam diameter used in the differential equation must be slightly larger than the measured value. This was explained in terms of the assumption that the current density distribution of the beam was uniform, when in fact the distribution follows a roughly Gaussian distribution. Finally, comparison of the sputtering yields measured for the creation of this contour, and the yields measured for the creation of a relatively shallow rectangular sputter crater, shows that the latter are of little value, even for this relatively simple contour.

B. FIBM of a Sinewave Surface.

The second application of vector scanning was to the fabrication of a simple sinewave surface. Again, several interesting observations were made. Under the proper bombardment conditions the shape of the machined contour closely matched that of the ideal contour. However, the shape of the machined contour was critically dependent on the bombardment conditions. Two very different contours were created under almost identical conditions, the only difference being the full scale deflection of the ion beam. By reducing the size of the contour, and hence increasing the average ion dose, the shape of the contour deviated significantly from the desired shape. The difference in shape was

attributed to second order effects such as self focusing of the beam and redeposition of sputtered material, and may have been avoided by using the technique of fast multiple scans. It was not possible to test this because of the limited speed of the computer used to control the ion beam.

III. FIBM of a 3-D Dome-Shaped Contour.

The final attempt at applying vector scanning involved the creation of a fairly complicated three dimensional contour. Unlike the previous examples, the depth of the contour depended on both x and y. Again, the limited speed of the computer required that the contour be created in a single scan of the beam, but the shape of the resulting contour closely matched the desired shape. This indicates that the vector scanning model presented here should be capable of producing a wide variety of complex surface contours.

[1] R. Levi-Setti, *Scanning Electron Microscopy*, **1** (1974), 125.

[2] J. Orloff, L. W. Swanson, *Scanning Electron Microscopy*, **1** (1977), 57.

[3] V. E. Krohn, Jr., *Prog. Astronaut. Rocketry*, **5** (1961), 73.

[4] V. E. Krohn, G. R. Ringo, *Appl. Phys. Lett.*, **27**(9) (1975), 479.

[5] R. Clampitt, K. L. Aitken, D. K. Jefferies, *J. Vac. Sci. Technol.*, **12**(6) (1975), 1208.

[6] R. Gomer, *Appl. Phys.*, **19** (1979), 365.

[7] R. Clampitt, *Nucl. Instrum. and Methods*, **189** (1981), 111.

[8] R. L. Seliger, J. W. Ward, V. Wang, R. L. Kubena, *Appl. Phys. Lett.*, **34**(5) (1979), 310.

[9] K. Lam, T. R. Fox, R. Levi-Setti, *28 Int. Field Emission Symposium*, Portland Oregon, 1981.

[10] R. L. Seliger, R. L. Kubena, R. D. Olney, J. W. Ward, V. Wang, *J. Vac. Sci. Technol.*, **16**(6) (1979), 1610.

[11] A. Wagner, *SPIE*, **393** (1983), 167.

[12] J. R. A. Cleaver, H. Ahmed, P. J. Heard, P. D. Prewett, G. J. Dunn, H. Kaufmann, *Microelectronic Engineering*, **3** (1985), 253.

[13] P. J. Heard, J. R. A. Cleaver, H. Ahmed, *J. Vac. Sci. Technol. B*, **3**(1) (1985), 87.

[14] T. D. Cambria, N. P. Economou, *Solid State Technol.*, Sept. (1987), 133.

[15] K. Saitoh, H. Onoda, H. Morimoto, T. Katayama, Y. Watakabe, T. Kato, *J. Vac. Sci. Technol. B*, **6**(3) (1988), 1032.

[16] L. R. Harriott, M. J. Vasile, *J. Vac. Sci. Technol. B*, **6**(3) (1988), 1035.

[17] T. Ishitani, Y. Kawanami, H. Todokoro, *Jpn. J. Appl. Phys.*, **24**(2) (1985), L133.

[18] L. R. Harriott, A. Wagner, F. Fritz, *J. Vac. Sci. Technol. B*, **4**(1) (1986), 181.

[19] H. Komano, Y. Ohmura, T. Takigawa, *IEEE Trans. Electron Devices*, **35**(7) (1988), 899.

[20] P. Sudraud, G. Ben Assayag, M. Bon, *J. Vac. Sci. Technol. B*, **6**(1) (1988), 234.

[21] R. Boylan, M. Ward, D. Tuggle, *Microelectron. Manuf. Test.*, **13**(2) (1990), 1.

[22] R. K. Defreez, J. Puretz, R. A. Elliott, J. Orloff, L. W. Swanson, *Electronics Lett.*, **22**(17) (1986), 919.

[23] L. R. Harriott, R. E. Scotti, K. D. Cummings, A. F. Ambrose, *Appl. Phys. Lett.*, **48**(25) (1986), 1704.

[24] J. Puretz, R. K. Defreez, R. A. Elliott, J. Orloff, T. L. Paoli, *Electronics Lett.*, **23**(3) (1987), 130.

[25] L. R. Harriott, R. E. Scotti, K. D. Cummings, A. F. Ambrose, *J. Vac. Sci. Technol. B*, **5**(1) (1987), 207.

[26] N. Takado, K. Asakawa, T. Yuasa, S. Sugata, E. Miyauchi, H. Hashimoto, M. Ishii, *Appl. Phys. Lett.*, **50**(26) (1987), 1891.

[27] M. C. Wu, M. Boenke, S. Wang, W. M. Clark, Jr., E. H. Stevens, M. W. Utlaut, *Appl. Phys. Lett.*, **53**(4) (1988), 265.

[28] R. A. Elliott, R. K. Defreez, J. Puretz, J. Orloff, G. A. Crow, *SPIE*, **876** (1988), 114.

[29] R. K. Defreez, J. Puretz, R. A. Elliott, G. A. Crow, H. Ximen, D. J. Bossert, G. A. Wilson, J. Orloff, *SPIE*, **1043** (1989), 25.

[30] K. Gamo, Y. Ochiai, S. Namba, *Jpn. J. Appl. Phys.*, **21**(12) (1982), L792.

[31] Y. Ochiai, K. Gamo, S. Namba, *J. Vac. Sci. Technol. B*, **1**(4) (1983), 1047.

[32] Y. Ochiai, K. Gamo, S. Namba, *Jpn. J. Appl. Phys.*, **23**(6) (1984), L400.

[33] Y. Ochiai, K. Gamo, S. Namba, *J. Vac. Sci. Technol. B*, **3**(1) (1985), 67.

[34] Y. Ochiai, K. Shihoyama, A. Masuyama, K. Gamo, T. Shiokawa, K. Toyoda, S.

Namba, *Jpn. J. Appl. Phys.*, **24** (1985), L169.

[35] Y. Ochiai, K. Shihoyama, T. Shiokawa, K. Toyoda, A. Masuyama, K. Gamo, S. Namba, *J. Vac. Sci. Technol. B*, **4**(1) (1986), 333.

[36] M. S. Ameen, T. M. Mayer, *J. Appl. Phys.*, **63**(4) (1988), 1152.

[37] K. Affolter, *J. Vac. Sci. Technol. B*, **7**(1) (1989), 19.

[38] M. Taneya, Y. Sugimoto, K. Akita, *J. Appl. Phys.*, **66**(3) (1989), 1375.

[39] J. Melngailis, C. R. Musil, E. H. Stevens, M. Utlaut, E. M. Kellog, R. T. Post, M. W. Geis, R. W. Mountain, *J. Vac. Sci. Technol. B*, **4**(1) (1986), 176.

[40] K. Gamo, N. Takakura, N. Samoto, R. Shimizu, S. Namba, *Jpn. J. Appl. Phys.*, **23**(5) (1984), L293.

[41] K. Gamo, S. Namba, *Microcircuit Engineering*, (1985), 389.

[42] K. Gamo, D. Takehara, Y. Hamamura, M. Tomita, S. Namba, *Microelectronic Engineering*, **5** (1986), 163.

[43] G. Shedd, H. Lezec, A. Dubner, J. Melngailis, *Appl. Phys. Lett.*, **49**(23) (1986), 1584.

[44] A. D. Dubner, G. M. Shedd, H. Lezec, J. Melngailis, *J. Vac. Sci. Technol. B*, **5**(5) (1987), 1434.

[45] Y. Ohmura, T. Shiokawa, K. Toyoda, S. Namba, *Appl. Phys. Lett.*, **51**(19) (1987), 1500.

[46] P. Sudraud, G. Ben Assayag, M. Bon, *Microelectronic Engineering*, **6** (1987), 583.

[47] R. L. Kubena, F. P. Stratton, T. M. Mayer, *J. Vac. Sci. Technol. B*, **6**(6) (1988), 1865.

[48] P. G. Blauner, J. S. Ro, Y. Butt, J. Melngailis, *J. Vac. Sci. Technol. B*, **7**(4) (1989), 609.

[49] A. D. Dubner, A. Wagner, *J. Appl. Phys.*, **65**(9) (1989), 3636.

[50] A. D. Dubner, A. Wagner, *J. Appl. Phys.*, **66**(2) (1989), 870.

[51] K. Nikawa, K. Nasu, M. Murase, T. Kaito, T. Adachi, S. Inoue, *IEEE/IRPS*, (1989), 43.

[52] R. L. Kubena, C. L. Anderson, R. L. Seliger, R. A. Jullens, E. H. Stevens, I. Lagnado, *J. Vac. Sci. Technol.*, **19**(4) (1981), 916.

[53] S. Shukuri, Y. Wada, H. Masuda, T. Ishitani, M. Tamura, *Jpn. J. Appl. Phys.*, **23**(8) (1984), L543.

[54] H. Hamadeh, J. C. Corelli, A. J. Steckl, *J. Vac. Sci. Technol. B*, **3**(1) (1985), 91.

[55] K. Ishida, E. Miyauchi, T. Morita, T. Takamori, T. Fukunaga, H. Hashimoto, H. Nakashima, *Jpn. J. Appl. Phys.*, **26**(4) (1987), L285.

[56] D. M. Hwang, R. Levi-Setti, G. Crow, Y. L. Wang, N. W. Parker, R. Mittlemen, X. W. Qian, S. A. Solin, *Synthetic Metals*, **12** (1985), 73.

[57] R. Levi-Setti, G. Crow, Y. L. Wang, N. W. Parker, R. Mittleman, D. M. Hwang, *Phys. Rev. Lett.*, **54**(24) (1985), 2615.

[58] R. Levi-Setti, G. Crow, Y. L. Wang, *Scanning Electron Microscopy*, (1985), 535.

[59] Y. L. Wang, G. Crow, R. Levi-Setti, E. Olsen, *Nucl. Instrum. and Methods B*, **10/11** (1985), 716.

[60] R. Levi-Setti, Y. L. Wang, G. Crow, *Appl. Surf. Sci.*, **26** (1986), 249.

[61] J. M. Chabala, R. Levi-Setti, Y. L. Wang, *J. Vac. Sci. Technol. B*, **6**(3) (1988), 910.

[62] H. Satoh, M. Owari, Y. Nihei, *J. Vac. Sci. Technol. B*, **6**(3) (1988), 915.

[63] L. R. Harriott, M. J. Vasile, *J. Vac. Sci. Technol. B*, **7**(2) (1989), 181.

[64] P. D. Prewett, P. Marriott, H. E. Bishop, *Microelectronic Engineering*, **10** (1989), 1.

[65] P. Sigmund, *Phys. Rev.*, **184**(2) (1969), 383.

[66] FEI Company, 19500 N. W. Gibbs Drive, Suite 100, Beaverton, OR. 97006.

[67] J. Orloff, L. W. Swanson, *J. Vac. Sci. Technol.*, **19**(4) (1981), 1149.

[68] G. I. Taylor, *Proc. Royal Soc.* (London), **280A** (1964), 383.

[69] L. W. Swanson, *Nucl. Instrum. and Methods*, **218** (1983), 347.

[70] A. E. Bell, L. W. Swanson, *Nucl. Instrum. and Methods B*, **10/11** (1985), 783.

[71] G. Ben Assayag, P. Sudraud, B. Jouffrey, *Ultramicroscopy*, **16** (1985), 1.

[72] D. R. Kingham, L. W. Swanson, *Vacuum*, **34** (1984), 941.

[73] D. R. Kingham, L. W. Swanson, *Appl. Phys. A*, **41** (1986), 157.

[74] M. Chung, N. M. Miskovsky, P. H. Cutler, T. E. Feuchtwang, E. Kazes, *J. Vac. Sci. Technol. B*, **5**(6) (1987), 1628.

[75] Micrion Corp., 1 Corporation Way, Centennial Park, Peabody, MA. 01960.

[76] H. Yamaguchi, A. Shimase, S. Haraichi, T. Miyauchi, *J. Vac. Sci. Technol. B*, **3**(1) (1985), 71.

[77] H. Yamaguchi, *Journal de Physique*, **48** (1987), C6-165.

[78] G. Crow, J. Puretz, J. Orloff, R. K. Defreez, R. A. Elliott, *J. Vac. Sci. Technol. B*, **6**(5) (1988), 1605.

[79] G. A. Schwind, personal communication.

[80] M. Komuro, H. Hiroshima, H. Tanoue, T. Kanayama, *J. Vac. Sci. Technol. B*, **1**(4) (1983), 985.

[81] Amray Inc., 160-T Middlesex Turnpike, Bedford, MA. 01730

[82] Digital Equipment Corp., 146-T Main Street, Maynard, MA. 01754

[83] Data Translation Inc., 100-T Locke Drive, Marlboro, MA. 01752.

[84] M. Vicanek, J. J. Jimenez Rodriguez, P. Sigmund, *Nucl. Instrum. and Methods B*,

36 (1989), 124.

[85] P. Ho, *Surf. Sci.*, **72** (1978), 253.

[86] J. D. Brown, F. G. Rudenauer, *J. Appl. Phys.*, **57**(8) (1985), 2727.

[87] Y. Homma, H. Okamoto, Y. Ishii, *Jpn. J. Appl. Phys.*, **24**(8) (1985), 934.

[88] O. Wada, *J. Phys. D*, **17** (1984), 2429.

[89] J. Massies, F. Turco, J. P. Contour, *Jpn. J. Appl. Phys.*, **25**(8) (1986), L664.

[90] T. Ishitani, A. Shimase, H. Tamura, *Appl. Phys. Lett.*, **39**(8) (1981), 627.

[91] R. Fabbri, M. Servidori, A. Zani, *J. Appl. Phys.*, **66**(10) (1989), 4715.

[92] D. S. Gemmell, *Rev. Mod. Phys.*, **46**(1) (1974), 129.

[93] Tektronix Inc., P. O. Box 500, Beaverton, OR. 97075.

[94] Wacker Siltronic Corp., P. O. Box 03180, Portland, OR. 97203.

[95] P. Sigmund, *Rev. Roum. Phys.*, **17**(7) (1972), 823.

[96] P. Sigmund, M. T. Robinson, M. I. Baskes, M. Hautala, F. Z. Cui, W. Eckstein, Y. Yamamura, S. Hosaka, T. Ishitani, V. I. Shulga, D. E. Harrison Jr., I. R. Chakarov, D. S. Karpuzov, E. Kawatoh, R. Shimizu, S. Valkealahti, R. M. Nieminen, G. Betz, W. Husinsky, M. H. Shapiro, M. Vicanek, H. M. Urbassek, *Nucl. Instrum. and Methods B*, **36** (1989), 110.

[97] M. T. Robinson, Oak Ridge National Laboratory Report No. ORNL-3493, 1963 (unpublished).

[98] K. B. Winterbon, P. Sigmund, J. B. Sanders, *Kgl. Danske, Videnskab. Selskab, Mat.-Fys. Medd.*, **37**(14) (1970).

[99] H. Cramer, *Mathematical Methods of Statistics*, Princeton: Princeton University Press, 1966, pp. 221 - 231.

[100] J. Lindhard, V. Nielsen, M. Scharff, *Kgl. Danske, Videnskab. Selskab, Mat.-Fys.*

Medd., **36**(10) (1968).

[101] K. M. Wang, X. J. Liu, Y. H. Wang, B. R. Shi, J. T. Liu, *J. Appl. Phys.*, **64**(7) (1988), 3341.

[102] P. Sigmund, "Sputtering Processes: Collision Cascades and Spikes", in *Inelastic Ion-Surface Collisions*, ed. N. H. Tolk, J. C. Tully, W. Heiland, and C. W. White (New York: Academic Press, 1977) p. 121.

[103] H. Miyake, Y. Yuba, K. Gamo, S. Namba, R. Mimura, R. Aihara, *Jpn. J. Appl. Phys.*, **27**(11) (1988), L2037.

[104] R. Williams, *Solid State Communications*, **41**(2) (1982), 153.

[105] M. Szymonski, R. S. Bhattacharya, Appl. Phys., 20 (1979), 207.

[106] M. Szymonski, H. Overeijnder, A. E. De Vries, Radiat. Eff., 36 (1978), 189.

[107] T. Ishitani, A. Shimase, H. Tamura, Appl. Phys. Lett., 39(8) (1981), 627.

[108] Y. Ochiai, K. Shihoyama, T. Shiokawa, K. Toyoda, A. Masuyama, K. Gamo, S. Namba, J. Vac. Sci. Technol. B, 4(1) (1986), 333.

[109] Z. H. Lu, E. Sacher, A. Selmani, A. Yelon, Appl. Phys. Lett., 54(26) (1989), 2665.

[110] R. R. Hart, C. L. Anderson, H. L. Dunlap, R. L. Seliger, V. Wang, *Appl. Phys. Lett.*, **35**(11) (1979), 865.

[111] L. R. Harriott, *SPIE*, **773** (1987), 190.

Biographical Note

The author was born in the United States towards the middle of the twentieth century. He attended a moderately sized midwestern college, where he received a B.A. in physics in 1983. Following graduation, he worked on the technical staff of the same school in the area of SIMS microanalysis using a *Ga* focused ion beam. In 1985, he moved to Oregon to attend the Oregon Graduate Center, where in October of 1990 he received a Ph.D. in applied physics. A list of the authors publications may be found on the following pages.

Publications

"Focused-Ion-Beam Micromachined Diode Laser Mirrors", R.K. Defreez, J. Puretz, R.A. Elliott, G.A. Crow, H. Ximen, D.J.Bossart, G.A. Wilson, J. Orloff, *SPIE*, **1043** (1989), 25.

"The Use of Vector Scanning for Producing Arbitrary Surface Contours with a Focused Ion Beam", G. Crow, J. Puretz, J. Orloff, R.K. Defreez, R.A. Elliott, *J. Vac. Sci. Technol.*, **B6** (1988), 1605.

"Focused-Ion-Beam Micromachining of Diode Laser Mirrors", R.A. Elliott, R.K. Defreez, J. Puretz, J. Orloff, G.A.Crow, *SPIE*, **876** (1988), 114.

"Effect of Weak Uniform Frustration on the Resistive Transition in a Josephson Junction Array", J.P. Carini, S.R. Nagel, R. Levi-Setti, Y.L. Wang, J. Chabala, G. Crow, *Solid State Communications*, **65** (1988), 977.

"Scanning Ion Microscopy: Elemental Maps at High Lateral Resolution", R. Levi-Setti, Y.L. Wang, G. Crow, *Appl. Surf. Sci.*, **26** (1986), 249.

"Progress in High Resolution Scanning Ion Microscopy and Secondary Ion Mass Spectrometry Imaging Analysis", R. Levi-Setti, G. Crow, Y.L. Wang, *Scanning Electron Microscopy 1985*, 535.

"Analytical Applications of Focused Ion Beams", N.W. Parker, W.P. Robinson, R. Levi-Setti, Y.L. Wang, G. Crow, *SPIE*, **537** (1985), 117.

"High Resolution Scanning-Ion Microprobe Study of Graphite and its Intercalation Compounds", R. Levi-Setti, G. Crow, Y.L. Wang, N.W. Parker, R. Mittleman, D.M. Wang, *Phys. Rev. Lett.*, **54** (1985), 2615.

"High Lateral Resolution SIMS Mapping of Meteorite Chondrule", Y.L. Wang, G. Crow, R. Levi-Setti, E. Olsen, *Nuclear Instruments and Methods in Physics Research*, **B10/11** (1985), 716.

"High-Resolution Topographic and Isotopic Imaging with a 40 keV Ga^+ Scanning Ion Microprobe", R. Levi-Setti, G. Crow, Y.L. Wang, in *Microbeam Analysis*, ed. J.T. Armstrong, San Francisco Press, 1985.

"Application of Microscopic Probes to the Study of Graphite Intercalation Compounds", D.M. Hwang, R. Levi-Setti, G. Crow, Y.L. Wang, N.W. Parker, R. Mittelman, X.W. Qian, S.A. Solin, *Synthetic Metals*, **12** (1985), 73.